Master Thesis

Flexible Negative Temperature Coefficient Thermistors

Ren Smis

Technische Universiteit Delft

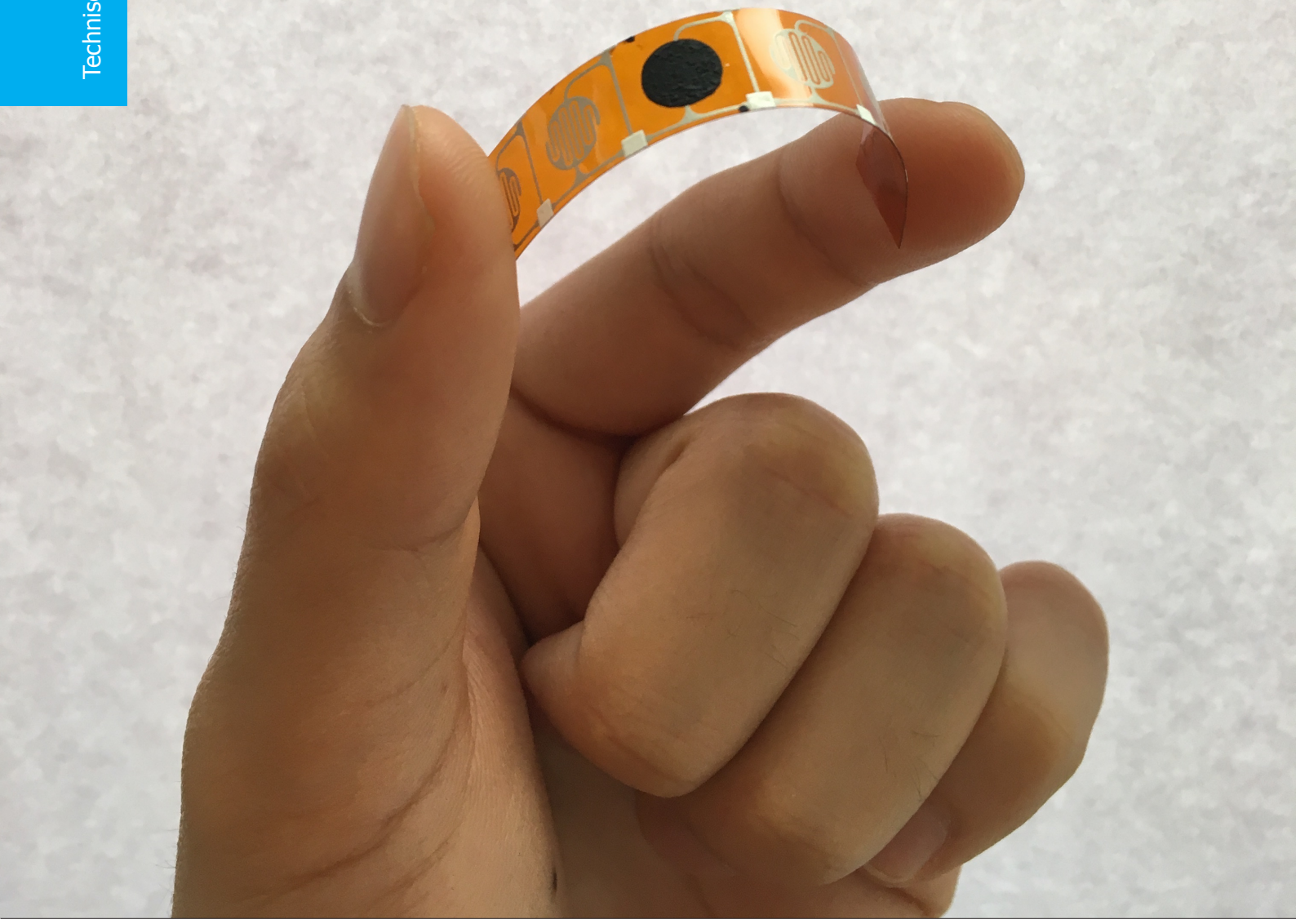

TU Delft Delft University of Technology

Challenge the future

Master Thesis

Flexible Negative Temperature Coefficient Thermistors

by

Ren Smis

to obtain the degree of Master of Science
at the Delft University of Technology,
to be defended publicly on 26-Feburary-2017.

Student number:	4095111	
Thesis committee:	Prof. dr. ir. Pim Groen,	TU Delft, supervisor
	Prof. dr. ir. S. van der Zwaag,	TU Delft, Chairholder NovAM
	Dr. R.M. Groves,	TU Delft

An electronic version of this thesis is available at http://repository.tudelft.nl/.

TU Delft

Aknowledgements

The work performed during my master thesis was both an enjoyable and rewarding experience that was a great way to end my journey to obtain the Master of Science at Delft University of Technology. I felt like I learned from the best and would like to thank everyone for their help and effort in contributing to such an environment.

In particular, I would like to thank my supervisor Prof. dr. Pim Groen for his support and guidance. His expertise and experience in the field of electroceramics were invaluable in guiding me through my thesis topic to obtain good results within a short timeframe. I would like to express a special thanks to Peter Zalar and Edsger Smits for taking the time to help me, and for providing me with expert council and experimental materials.

I would also like to kindly thank Vincent Stuber for his insights and helping me with ceramic-related problems, and in particular fibre spinning and equipment trainings. I would have found myself quite lost without your help and I am deeply grateful for it. Thank you to all the technicians from the Delft Aerospace Structures and Materials Laboratory, especially Misja Huizinga and Frans Oostrum for their all-around help. It has been such a pleasure to be part of NovAM as its such a warm and welcoming research group. Its been a great run while it lasted!

Preface

Negative temperature coefficient of resistance (NTC) materials are materials that experience a decrease in resistivity with increasing temperature, making them ideal for temperature sensing applications. In this study NTC ceramics and NTC ceramic-polymer composites are investigated towards the desire to produce a fully flexible temperature sensor that can readily be used in industry.

Ren Smis
Delft, Feburary 2018

Abstract

Flexible electronics have become the subject of industry focus, generating a market desire for fully flexible temperature sensors. To the best of our knowledge, there are no current systems that can adequately satisfy both the mechanical flexibility and sensing performance demanded for commercial applications. This work focused on a design for a flexible temperature sensor by designing a thermistor using functional granular composites using ceramic NTC fibre particles and a resistive polymer matrix. The objective was to achieve good thermistor performance (high sensitivity: B-value > 3000 K, and low resistivity: $\rho \approx 10^1 - 10^2\ \Omega cm$) while being mechanically flexible (surviving bending radii ≤ 1 cm over 100 cycles).

To achieve this objective this thesis work was organised into 5 major phases. Due to the high commercial value of NTC ceramic thermistors, no reference composition with its exact processing conditions are available in literature that produce a thermistor with commercially desirable properties. Phase 1 was therefore to select a NTC ceramic composition and Phase 2 was to investigate the necessary processing conditions to be able to produce bulk ceramics with adequate temperature sensing performance. Phase 3 involved making NTC ceramic fibres by wet fibre spinning and modifying the processing conditions developed in Phase 2. Phase 4 involved the selection of an appropriate polymer matrix and to attempt to create thermistor composites. Phase 5 involved creating more optimal composite thermistors using stencil printing and to test its thermistor and bending performance.

Using an isotropic mixture of $\mathrm{Mn_{2.4}\,Ni_{0.5}\,Cu_{0.1}\,O_4}$ NTC ceramic fibre particles in an Electrodag matrix, composite thermistors were created by stencil printing onto thin-film substrates of polyethylene terephthalate that have silver inkjet printed interdigitate electrodes. A percolated network is formed with as little as 10 wt% of fibres (≈ 2.86 vol%). The composite with 10 wt% of fibres has good thermistor performance at a low fibre content. The average resistivity at $25°C$ (ρ_{25}) is low around $920 \cdot 10^3\ \Omega cm$ (with a standard deviation of $220 \cdot 10^3\ \Omega cm$) and the sensitivity is high with a B-value = 3290 K and $\alpha_{25} = -3.7\ \%/K$. The overall composite resistance and sensitivity can be tailored and customised by changing the gap width of the interdigitate electrodes. At an electrode gap width of 0.13 mm, with our interdigitate electrodes, $R_{25} = 280\ k\Omega$ and $R_{85} = 45\ k\Omega$. The composite with 10 wt% fibre particle content and an electrode gap of 0.13 mm can survive 300 bends cycles (100 cycles with bending radius 10 mm ($\varepsilon \approx 0.621\%$), 100 cycles with bending radius 5 mm ($\varepsilon \approx 1.23\%$), 100 cycles with bending radius 2.5 mm ($\varepsilon \approx 2.44\%$) without any observable, aesthetic damage. The relative resistance (R/R0) does increase with bending, but after 20 bend cycles it appears to stabilise for every bending radius. In comparison to other flexible temperature sensors in recent literature, this thermistor composite is found to deliver a superior combination of thermistor performance and mechanical flexibility.

Contents

List of Figures

List of Tables

List of Symbols & Abbreviations

α	Temperature Coefficient of Resistance [% per $^{\circ}C$]
$\Delta R/R$	Resistivity drift after being exposed to $150^{\circ}C$ for 1000 hours [%]
Γ	Geometry Factor Γ that influences the degree of anisotropy in conductivity
μ	Charger carrier mobility [cm^2 per V sec]
ρ	Resistivity [$\Omega \cdot m$]
ρ_{∞}	Resistivity at infinite temperature
ρ_i	Intrinsic resistivity [$\Omega \cdot m$]
ρ_t	Tunneling resistivity [$\Omega \cdot m$]
σ	Conductivity [Simens per meter S/m]
σ_{∞}	Conductivity at infinite temperature
e	Charge carrier charge [coulombs]
G	Geometry Factor G that influences the degree of anisotropy in conductivity
k	Stefan-Boltzmann constant [$5.6704 \times 10^{-8} W \cdot m^{-2} \cdot K^{-4}$]
N	The number of charge carriers per cm^3
P_a	Probability that the adjacent B-site is occupied by an acceptor cation
P_d	Probability that the particular B-site is occupied by a cation capable of being an electron donor
q	Hopping mechanism activation energy
R	Resistance [Ohms, Ω]
R_{∞}	Device resistance at infinite temperature
R_c	Overall resistance of a composite conductor [Ohms, Ω]
R_e	Lead resistance to electrodes [Ohms, Ω]
R_i	Intrinsic resistance of a particle [Ohms, Ω]
R_p	Particle to particle contact resistance [Ohms, Ω]
R_t	Tunneling resistance [Ohms, Ω]
R_{cr}	Constriction resistance [Ohms, Ω]
v	Frequency factor
v_f	Percolation limit or critical volume fraction [% filler]
B-value	Also known as the Thermal Constant of an NTC thermsitor
IC	Integrated Circuits
IDE	Interdigitate Electrodes

NTC Negative Temperature Coefficient

PTC Positive Temperature Coefficient

RTDs Resistance Temperature Detectors

SD Standard deviation

SEM Scanning Electron Microscope

XRD X-ray Diffraction

1 Introduction

1.1. Temperature Sensors

Temperature sensing for temperature monitoring and regulation is necessary in many diverse applications and processes across many industries, sectors, and daily life. Towards this, there have been many different types of temperature sensors that have been developed using differing principles of operation. At the most basic level, temperature sensors can be categorised into contact vs. non-contact temperature sensors. Contact temperature sensors principally use conduction to 'sense' and measure the temperature of something, as opposed to non-contact temperature sensors that use convection and radiation. Within the two very basic categories there are many sub-divisions, but most contact temperature sensors used in industry would fall under the following general groups:

- Thermocouples
- Resistance Temperature Detectors (RTDs)
- Integrated Circuit (IC) sensors
- Thermistors (Thermally Sensitive Resistors)

Thermocouples are the most commonly used type of temperature sensor because they are relatively simple, small and have a good speed of response. They are basically made by connecting two dissimilar metal wires at two points (a reference point, kept at a constant temperature called the cold junction, and one point to measure the temperature of something, called the hot junction). An example of a thermocouple device is presented in figure 1.1a. The difference in temperature between the two points causes a difference in voltage, which can be used to determine the temperature of something. Although they typically have the widest temperature range, they have lower accuracy and are less sensitive to small changes in temperature (requiring amplification). Moreover, they also require a reference point or junction as a reference temperature (hence, the device architecture of the temperature sensor needs to insulate and isolate the reference junction).

Resistance Temperature Detectors (RTDs) are made from high purity conducting metals (e.g. typically platinum) as a film or wire wrapped around a glass or ceramic core, an example of which is shown in figure 1.1b. When connected to a current they output a voltage that changes linearly with temperature (since their resistance changes with temperature) and is how they are used as temperature sensors. They are good temperature sensors because they deliver a linear response and have good accuracy. However, they have low temperature sensitivity and slow response time. Also, due to the use of platinum, they are expensive devices. One of the most common RTDs is the PT1000 temperature sensor which uses platinum and has superb accuracy over a wide temperature range, typically -200 to $+850°C$. The PT1000 has a resistance R = 1000 Ω at $0°C$ and is why it is so appropriately named. Linearisation is applied to the temperature sensor, but typically for a PT1000 sensor, a change of $1°C$ causes a change of 3.91 Ω [4]. This means that errors in measuring the resistance translate to large errors in measuring the correct temperature, possibly due to the resistance of the electrode wires or due to self-heating.

This is why many PT1000 sensors have two wires, for current in and out, and two wires for the voltage measurements, while sensor packaging is designed to efficiently dissipate heat to the environment.

Integrated circuit (IC) sensors are temperature sensors based on semiconductors that are placed on an integrated circuit. They are typically two temperature sensitive diodes that produce an output current proportional to their temperature [2]. Figure 1.1d presents an example of an IC temperature sensor. Their main advantages are highly linear output over it's temperature range and general low cost. They are however, low in accuracy and have a very narrow temperature range as compared to the other temperature sensor types.

Thermistors are thermally sensitive resistors and vary in resistance when subjected to a change in temperature. An example of a conventional thermistors is shown in figure 1.1c. They used to be limited by poor stability and a moderate operational temperature range but due to advancements in development, they have largely overtaken thermocouples [35]. Thermistors generally experience a large change in electrical resistance per degree celsius in temperature (-2 to -6 $\%/^{\circ}C$) which makes them more sensitive to smaller temperature changes, as compared to other temperature sensors like platinum RTDs. Furthermore, the response time is fast and has high accuracy $(0.001 - 1 \pm^{\circ} C)$. They have a rather wide operating temperature range, are low in cost to manufacture, and can be produced in small sizes and in a variety of shapes.

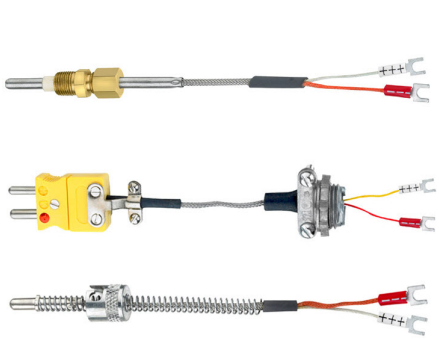

(a) Thermocouples [14]

(b) RTD [4]

(c) Thermistor [22]

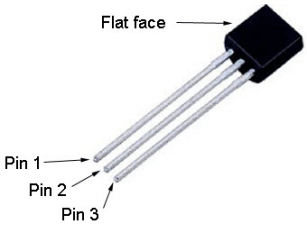

(d) IC sensor [14]

Figure 1.1: Examples of Various Temperature Sensors

Each group of temperature sensor has it's advantages and disadvantages. A review of these sensors has been summarised and tabulated by [17] and presented in table 1.1.

As a temperature sensor, thermistors are very popular due to their aforementioned advantages. So much so that they are found in such a wide range of applications in different sectors of industry from engine temperature monitors, to air conditioning controllers, general body temperature measurements, to chemical industries to control process temperatures [35]. According to [17], 40% of most thermistors produced are for use in the automobile industry, while 30% are used for the consumer electronics industry. Although, these figures may have significantly changed since the time of publication due to the emergence of thermistors for new markets like medical applications (e.g. for blood temperature monitoring during hemodialysis).

Table 1.1: Characteristic Advantages and Disadvantages of Temperature Sensor Types [17]

Characteristics	Thermocouple	RTD	Thermistor	Integrated circuit
Active material	Two dissimilar metals	Platinum	Ceramic	Si or Ge
Changing parameter	Voltage	Resistance	Resistance	Voltage or current
Temperature range [°C]	−270 to +2300	−200 to +650	−50 to +1000	−55 to +150
Additional circuitry	Reference junction	Lead compensation	Linearization	Linearization
Sensitivity	∼1–80 μV/°C	∼0.4%/°C	−2%/° to −6%/°C	−7.3%/°C (Si) −5%/°C (Ge)
Accuracy [± °C]	0.5–5	0.001–1	0.001–1	1
Response time	Fast, 0.1–10 s	Slow, 1–50 s	Fast, 0.1–10 s	Fast, <0.1 s
Stability	Moderate	Excellent	Moderate	High
Cost	Low	Moderate to high	Low to moderate	Low
Advantages	Wide operating temperature range, Low cost, Rugged	Linearity, Wide operating temperature range, Highest stability	Fast response time, Low cost, Small size, Large changes in resistance versus temperature	Highly linear, Low cost
Disadvantages	Nonlinear, Low sensitivity, Reference junction compensation required, Subject to electrical noise	Slow response time, Expensive, Current source required, Sensitive to shock	Nonlinear, Current source required, Currently, limited temperature range	Very limited temperature range, Power source required

Thermistors are undoubtably very popular in industry as temperature sensors. However, their unique characteristics aren't limited to temperature sensing, after all their principle behaviour is that they produce a change in electrical resistance due to a change in temperature. They are therefore invaluable as a circuit component since thermistors can also act as an:

- Electronic time delay
- Capacitor/inductor in a low frequency oscillator
- Surge supressor in capacitive/inductive/resistive circuits
- Voltage/current limiter
- Resettable fuse for current overload protection, etc.

1.2. Flexible Temperature Sensors

Flexible temperature sensors are desirable as part of the increasing trend in industry to produce flexible electronics. Real-time measurements are often necessary for sensor applications, which conventionally were limited to being embedded on flat and rigid surfaces, but "large sensor dimensions and difficulty in packing have long been the key limiting factors to desirable measurements" [58]. Flexible sensors open a new world of possibilities since designs can now use non-conventional form factors to allow new devices like flexible wearable devices / electronics (from wearable sensors to smart fabrics). Previously attention was mostly paid to miniaturisation of electronic components, to some extent this enabled rigid sensors to be placed onto flexible substrates to enable quasi-flexible electronics. However, new applications are pushing industry to produce sensors with greater flexibility, greater durability, greater electrical performance, ease of handling, lower cost, lighter weight, and biocompatibility [37]. Some specific examples for the potential of flexible temperature sensors are covered but are not limited to the following:

Humanoid robot development has seen a upsurge in recent years and there is a need for intelligent sensing capabilities which has led to the desire for artificial skin. This artificial skin would enable the robots to sense and avoid damage to itself and others through the provision of a basic sense of touch and temperature, schematically illustrated in figure 1.2a. Towards this application, flexible temperature sensors are required that have enough flexibility to cover three dimensional surfaces [60]. An example of flexible electronic skin embedded with sensors (organic transistors) is illustrated in figure 1.2b, produced by the Someya Lab at the University of Tokyo [53].

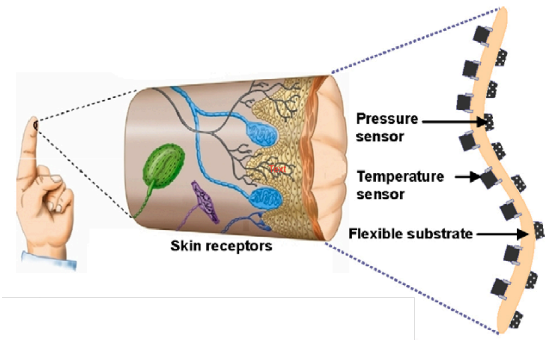

(a) Artificial skin desired for humanoid robots [60]

(b) Prototype robot hand covered in flexible skin integrated with sensors [28]

Figure 1.2: Flexible electronic skin for humanoid robot developement

Wearable health monitoring systems is a growing area of interest as the current world's population is ageing and healthcare in some places is becoming more expensive. Real-time monitoring of health indicators (e.g. body and skin temperature) is desirable for patients admitted to hospital to improve patient comfort, but also to monitor a discharged patient when in their normal environment. This real-time monitoring can then be used to either alert the patient himself, or be connected to a health system that can flag for potential problems either through a smart artificial intelligence system or to a physician directly. The challenge with wearable sensors is to comply with ergonomic constraints and significant hardware resource limitations. The size and weight of the sensor/device needs to be small and light, and there shouldn't be aesthetic issues or the patient may refuse to wear the sensor. Security and privacy of the patient needs to be safeguarded, and power consumption needs to be kept low to ensure a long operational lifetime so the device is practical in real life usage. Moreover, to be actually used in practice, the device needs to be affordable to enable the use of many sensors if needed (i.e. it needs to be cheap enough for the market to actually be interested) [47]. A good example that will help the reader to visualise the goal of wearable health monitoring systems is depicted in figure 1.3 which is a wearable sensor under development by a startup company called MC10, who specialises in flexible electronics.

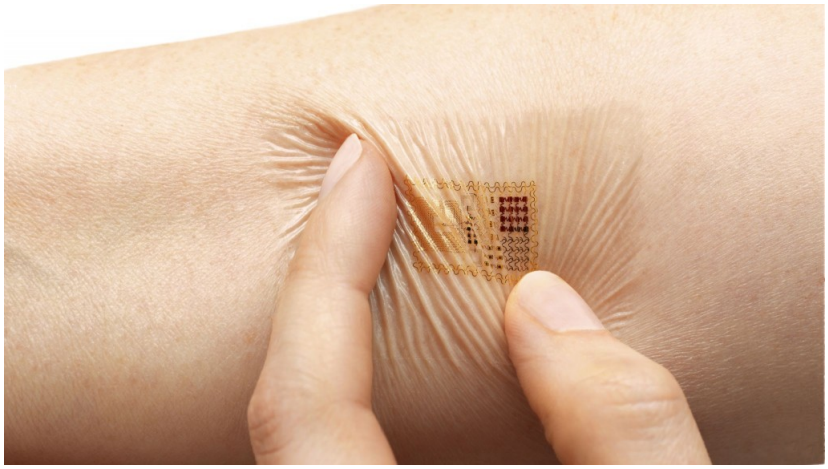

Figure 1.3: A prototype of MC10's BioStamp sensor [10]

Another potential application of flexible temperature sensors is the creation of a human protective suit that is equipped with a complete set of biomedical monitoring sensors to monitor the internal temperature, external chemicals, and other life signals [7]. The purpose of such a protective suit could extend from hazardous environments like chemical waste disposal, to nuclear contamination, to harsh space environments. What is then required from the biomedical monitoring sensors, like the tempera-

ture sensor, is high accuracy, small size and low weight, good durability, biocompatibility and of course, flexibility.

Moreover, a constant pursuit within the aerospace industry is to reduce the size and weight of aircraft and spacecraft structural elements to achieve lighter vehicles. Weight savings in the operational empty weight directly correlates to savings in fuel costs or an increase in payload capability [16]. This translates to cheaper operational costs as well as lowering environmental impact. However, to lower the safety factors used on over-engineered structural elements in aircraft, better health monitoring systems are needed. Towards better and more extensive health monitoring systems, flexible sensors (including temperature sensors) are required. Conventional thermistors are made from electro-ceramic material that are often inflexible and heavy. So by shifting to a flexible composite, a lighter sensor will consequently be made.This would then make the flexible temperature sensor desirable to other markets that also value weight reduction (not just flexibility). Furthermore, when designed correctly, sensors with greater mechanical flexibility can have higher durability and better reliability. Sensors with better reliability are very desirable for the aerospace industry for critical systems like satellites and other spaceflight equipment where resources are scarce.

1.3. Thermistors (NTC vs PTC)

Thermistors are thermally-sensitive-resistors and are called such because their electrical resistance varies over a temperature range by it's coefficient of resistance. This coefficient of resistance can be positive or negative or switch from one to the other. Negative temperature coefficient (NTC) thermistors have a decrease in resistance as temperature increases, while positive temperature coefficient (PTC) thermistors experience an increase in resistance with increasing temperature. However, the resistance versus temperature behaviour can be non-linear as can be seen in figure 1.4. Switching thermistors can show NTC behaviour over an initial range, then switch to PTC behaviour beyond a certain temperature.

For many applications NTC or PTC thermistors can be used, but selection ultimately depends upon many factors (e.g. required operational voltage, power level, physical size, mechanical construction, cost, availability or personal experience, etc.). For temperature measurement, which is the scope of this thesis, NTC thermistors are typically chosen due to their large temperature range, large change in resistance vs temperature, and sensitivity. For these reasons and other advantages covered in section 1.1, NTC thermistors are examined further in the next section.

1.4. NTC Thermistor Material Properties

1.4.1. Crystal Structure

Crystallographically, most NTC thermistor compounds have the same structure; the spinel structure. The spinel structure takes its name from the mineral $MgAl_2O_4$ and is a term used to describe a class of minerals with the common formula of $A^{+2}\,B_2^{+3}\,O_4$. A can be one or more divalent metals that form AO oxides (e.g. FeO, CuO, NiO, CoO) while B can be one or more trivalent metals that form B_2O_3 oxides (e.g. Fe_2O_3, Mn_2O_3). By combining them we get the spinel structure $AO + B_2O_3 = AB_2O_4$ (e.g. $MgO + Al_2O_3 = MgAl_2O_4$).

The spinel crystal structure is best described by a cubic close packing of O^{2-} anions, where some of the interstitial sites are then occupied by Mg^{2+} and Al^{3+} cations. To better understand the crystal structure, its best to visualise atoms within a crystal lattice as hard spheres which can be packed into solid structures of crystals, as proposed by Goldschmidt in 1926. Closed packed structures refers to the closest arrangement of atoms to minimise the volume of unfilled space, hence maximise the efficiency of packing. For a single layer of atoms this is achieved by a hexagonal coordination around each sphere, depicted in figure 1.5a. To get the closest packed 3D structure, when the second layer of spheres is added, it gets placed in the indentations left by the first layer. When this is performed, two types of holes (also called interstitial sites) are formed from the spaces trapped between the first and second layers. The first type is called tetrahedral hole/interstices which is a hole formed with 4 nearest sphere neighbours, depicted in figure 1.5b. The second type is called octahedral holes/interstices which are holes with 6 nearest neighbours, depicted in figure 1.5c. In crystallography, tetrahedral or octahedral holes or interstices are often geometrically represented by a tetrahedron or octahedron,

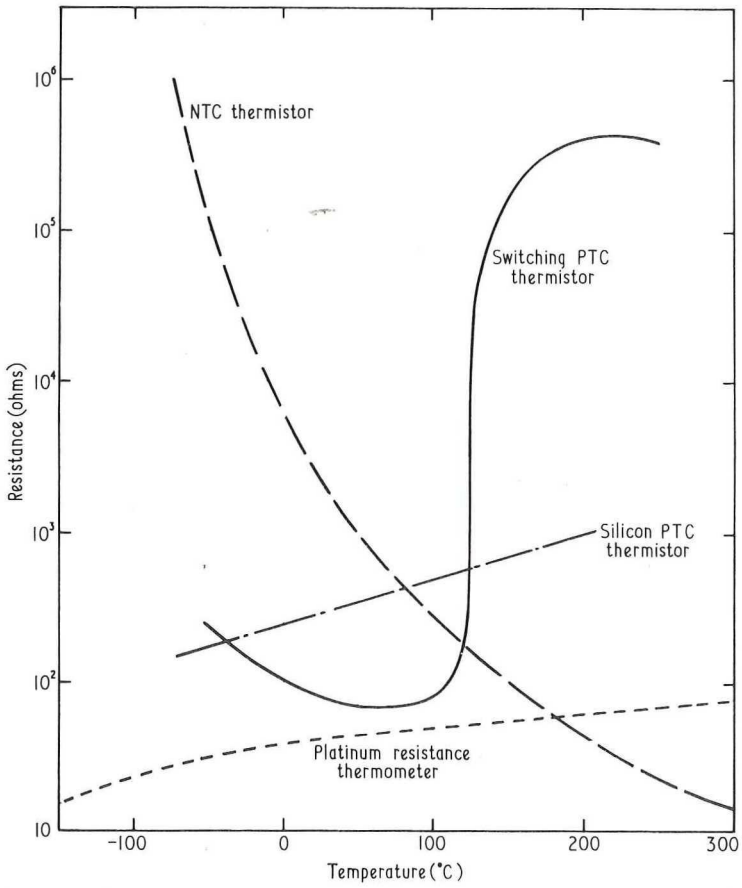

Figure 1.4: Resistance vs temperature behaviour of NTC & PTC thermistors compared to a platinum resistance thermistor [35]

which is formed by treating each atom as a vertex and joining the lines, as shown in figure 1.6. When a third layer of atoms is added and placed in the indentations of the second layer, the configuration has two options. Either the third layer and first layer are directly in line or the third layer is staggered with respect to the first and second layer. The first option has a layer ordering of ABA and is referred to as Hexagonal Close-Packing (HCP), as shown in figure 1.7a. The second option has a layer order of ABC, also called Cubic Close-Packing (CCP), as shown in figure 1.7b.

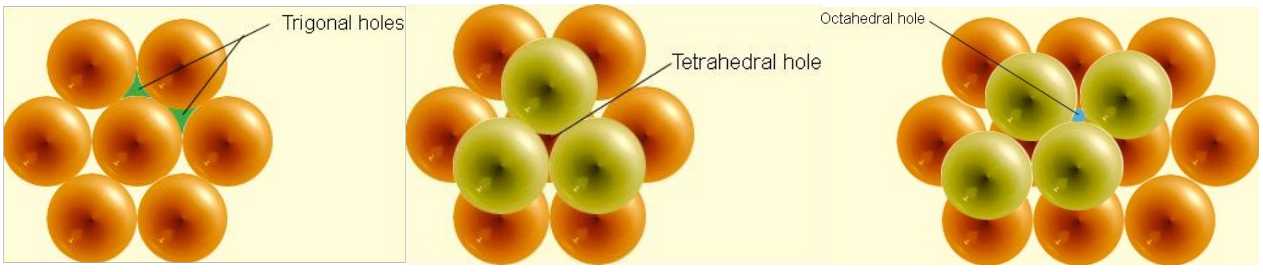

(a) Hexagonal Coordination (b) Tetrahedral Interstitual (c) Octahedral Interstitual

Figure 1.5: Close Packing of Atoms (images taken from [34])

In closed packed structures, for every N amount of spheres there are $2N$ number of tetrahedral interstices and N number of octahedral interstices created. So when looking at the unit cell of a spinel crystal, the unit cell contains 8 formula units of $MgAl_2O_4$ which amounts to 8 Mg^{2+}, 16 Al^{3+}, and 32

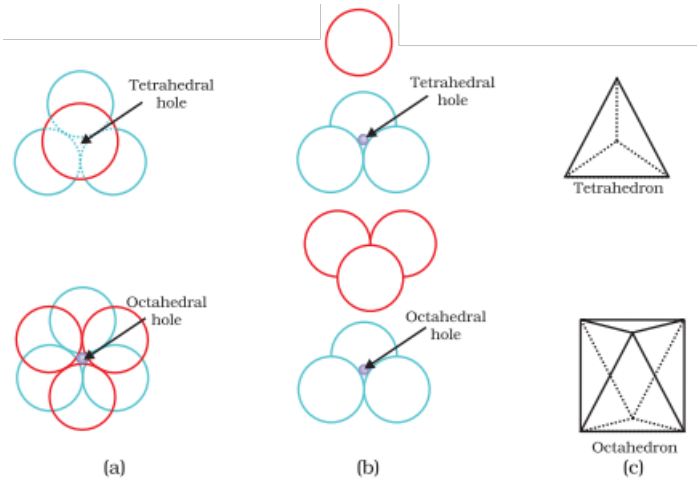

Figure 1.6: Geometrical representation of tetrahedral and octahedral voids (taken from [3])

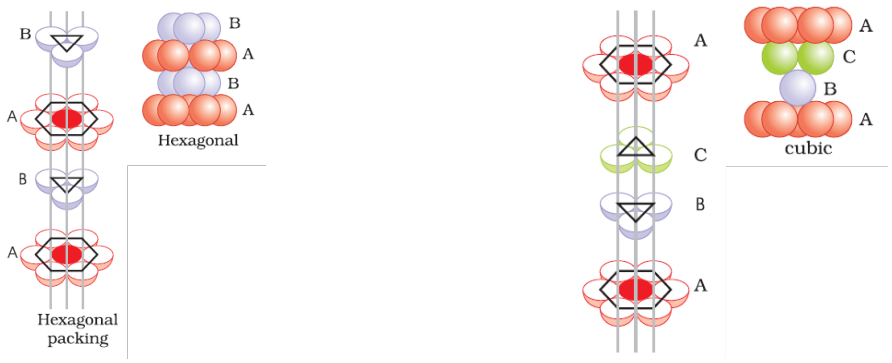

(a) Hexagonal Close-Packing (HCP)

(b) Cubic Close-Packing (CCP)

Figure 1.7: Configuration of 3-layers (images taken from [40])

O^{2-} atoms. Therefore, there are 64 tetrahedral interstices and 32 octahedral interstices. Or in the more general form; a spinel unit cell of formula AB_2O_4 has 8 A atoms, 16 B atoms, and 32 O^{2-} atoms. The 64 tetrahedral interstices are also called A-sites, since A atoms (e.g. Mg^{2+}) normally occupy these holes. Hence, $\frac{1}{8}$ of the tetrahedral holes (A-sites) are occupied (8A atoms and 64 A-sites). Similarly, the 32 octahedral interstices are also called B-sites, since B atoms (e.g. Al^{3+}) normally occupy these holes. Hence, $\frac{1}{2}$ of the octahedral holes (B-sites) are occupied (16B atoms and 32 B-sites). The spinel crystal structure is given in figure 1.8 which shows how the octahedrons occupied with Al^{3+} cations share edges between octahedra, and share corners with tetrahedra occupied with Mg^{2+} cations.

The aforementioned spinel structure where A cations (Mg^{2+}) occupy tetrahedral holes (A-sites) and B cations (Al^{3+}) occupy octahedral holes (B-sites) is referred to as normal spinels. They can be denoted simply as $[A]^{tet}[B_2]^{oct}O_4$. Inverse spinels exist where half of the B cations (Al^{3+}) occupy tetrahedral holes while the other half occupy the octahedral holes along with the A cations (Mg^{2+}). These inverse spinels can be denoted as $[B]^{tet}[A, B]^{oct}O_4$. Structures in between normal and inverse spinels exists and are characterised by the degree of inversion or γ, which is a parameter that defines the fraction of A ions on the octahedral sites [17]. For example, for $MnFe_2O_4$ with a $\gamma = 0.3$ we have a cation distribution of $Mn^{2+}_{0.7}\,Fe^{3+}_{0.3}\,(Mn^{2+}_{0.3}\,Fe^{3+}_{0.7})\,O_4$.

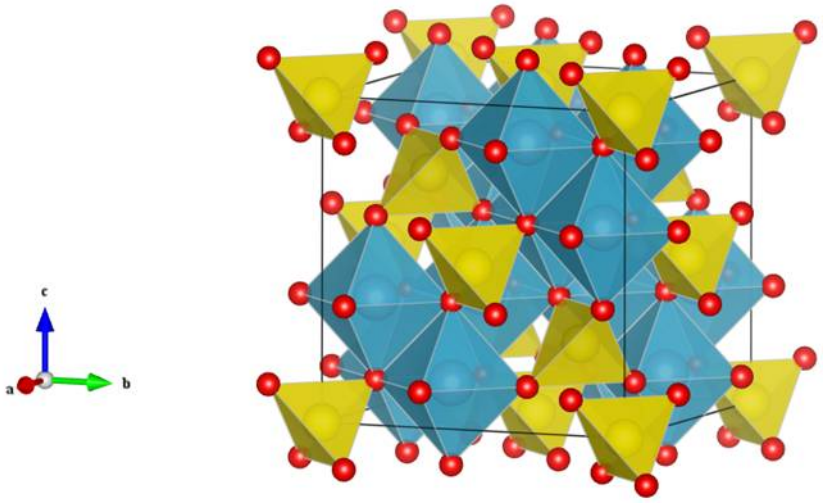

Figure 1.8: Spinel crystal structure of $MgAl_2O_4$ (AB_2O_4) where Mg cations occupy the yellow tetrahedra and Al cations occupy the blue octahedra (taken from [12])

1.4.2. Mechanism Behind Electrical Conductivity

For nonmetallic materials conductivity can be a result of one or both electrical conductivity (i.e. movement of electrons) or ionic conductivity (i.e. movement of ions). Due to the fact that chemical changes and polarisation phenomena simultaneously occur with ionic conduction, electronic semiconducting materials are favoured when manufacturing NTC sensors [17].

The electrical conductivity mechanism in spinel structures are caused by a hopping mechanism where charge carriers hop across ionic sites. Furthermore, its has been determined empirically that the spinel must satisfy the following conditions to have electrical conductivity in a spinel crystal [35]:

- Ions of the same element, but of different valency, occupy crystallographically equivalent lattice sites.
- The ions must differ by only one valency (e.g. Mn^{2+} and Mn^{3+}, but not Mn^{2+} and Mn^{4+})
- The differing ions must occupy the octahedral (B-sites). (Tetrahedral (A-sites) are too greatly spaced for electron hopping to be successful).

To illustrate, with a spinel material like Fe_3O_4, the cation distribution needs to be $[Fe^{3+}]^{A-site}\,[Fe^{2+}, Fe^{3+}]^{B-site}\,O_4$ so that electron hopping is possible.

$$\begin{array}{lll} Fe^{2+} & e^- \longrightarrow & Fe^{3+} \\ \downarrow & & \downarrow \\ Fe^{3+} & & Fe^{2+} \quad e^- \longrightarrow \quad Fe^{3+} \\ & & \downarrow \qquad\qquad \downarrow \\ & & Fe^{3+} \qquad\quad Fe^{2+} \end{array}$$

As illustrated, electrons can therefore move through the spinel structure when an external electric field is applied while keeping the entire crystal electrically neutral. Conductivity is then determined by the number of these ions that can allow electron hopping and the activation energy of the hopping mechanism. The activation energy is the minimum energy needed for the electron to escape (or hop) from an ion and is a function of temperature.

By doping or adding different elements to a NTC material, the conductivity can be drastically altered due to a change in the valency distribution on the B-sites of the crystal lattice. Thus influencing the amount and distribution of acceptor and donor ions that then influence the amount of electrons that can travel through the lattice. To illustrate, Mn_3O_4 has a normal spinel structure which is non-conducting because the valency distribution is: $[Mn^{2+}]^{A-site}\,[Mn^{3+}, Mn^{3+}]^{B-site}\,O_4$. Through the addition of Nickel to this system, Ni^{2+} will replace some Mn^{3+} ions at the B-site, and some Mn^{3+} ions will change to Mn^{4+}

to preserve the overall electrical neutrality of the material. The new valency distribution will now be $[Mn^{2+}]^{A-site}\,[Ni_x^{2+}, Mn_x^{4+}, Mn_{1-2x}^{3+}, Mn^{3+}]^{B-site}\,O_4$. This new system is now electrically conductive since Mn^{3+} and Mn^{4+} ions at the B-sites will enable electron hopping through the lattice. (It must be noted that it is argued in literature that some Ni^{2+} ions exist on the A-sites, but whether this is in fact true or not is less relevant since its the valency distribution of the b-site that effects conductivity [35]).

1.4.3. NTC Material Stability

The stability of thermistors is a difficult topic because thermistors experience ageing where the resistance of a NTC thermistor device at a particular value progressively changes with time, temperature and use. This then directly affects the accuracy of the NTC thermistor device for temperature measurement. The underlying mechanisms that cause ageing is not well understood in literature. Macklen [35] proposed three different mechanisms that are the potential underlying mechanism that causes ageing in thermistor materials:

1. Changes of oxygen content of the oxide composition.
2. Rearrangement of cation distribution within the ceramic material by diffusion.
3. Changes in the electronic states on the surface of the crystallites in contact with each other over time.

These mechanisms aren't fully comprehensive nor fully proven. Instead, Groen et al. [19] derived a model that describes the ageing mechanism of NTC ceramics with the crystal spinel structure due to the process of:

1. Migration of cationic vacancies from grain boundary to bulk.
2. Migration of cations and cationic vacancies to their thermodynamic favourable site, within the spinel structure [19].

Considering that the electrical conductivity mechanism in spinel structures is caused by a hopping mechanism of charge carriers across mostly the B-sites. This ageing model can then account for the increase in resistivity observed in aged NTC thermistors due to the increase in vacancies in the B-sites in the bulk of the grains.

Irrespective of the precise underlying mechanism for the ageing phenomena observed in NTC thermistors, thermistor manufacturers have exercised better control over manufacturing techniques (precursor material purity, mixing technique, sintering recipes, etc) that have improved the stability of devices. Furthermore, experimental trials have shown that for many NTC thermistor materials, most ageing occurs in the first few weeks. Thermistor manufacturers then pre-age their devices so that the devices they deliver have stabilities that are better than 1% resistance change per year for temperatures up to their maximum recommended operating temperatures. Through better control of processing operations and pre-aging, the stability of NTC devices are no longer a concern for practical purposes. For this reason, thermistor stability will not be further investigated since it is an active area of research that is beyond the scope of this work.

1.4.4. Electrical Conductivity

The underlying hopping mechanism through which a n-type NTC material can conduct is explained in section 1.4.2 and its conductivity is given by formula 1.1 where N is the number of charge carriers per cm^3, e is their charge [coulombs], and μ is charger carrier mobility [cm^2 per V sec].

$$\sigma = Ne\mu \tag{1.1}$$

Where N is a factor of the density of B-sites and P_d, the probability that the occupied B-sites are occupied by a cation capable of acting as an electron donor. N is given by equation 1.2 where a and c are the unit cell dimensions in cm.

$$N = \frac{16P_d}{a^2c} \tag{1.2}$$

The charge carrier mobility μ is given by equation 1.3, where d is the distance between B-site cations' nearest neighbours, v is a frequency factor, q is the hopping mechanism activation energy, k is the Stefan-Boltzmann's constant, and T is the absolute temperature in $°K$.

$$\mu = \frac{ed^2ve^{\left(\frac{q}{kT}\right)}}{kT} \tag{1.3}$$

The formula for electrical conductivity can then be re-expressed by combining equations 1.1, 1.2, 1.3 and by correcting for true mobility (by multiplying by P_a, the probability that the adjacent B-site contains an acceptor cation):

$$\sigma = P_a \cdot P_d \frac{16e^2d^2ve^{\left(\frac{-q}{kT}\right)}}{a^2ckT} \tag{1.4}$$

Further simplifying equation 1.4 for a spinel since $d = (a\sqrt{2})/4$ so $d^2 = 2a^2/16$, conductivity can be re-expressed as:

$$\sigma = \sigma_\infty e^{\left(\frac{-q}{kT}\right)} \tag{1.5}$$

Where it has been implicitly assumed that the variation of conductivity with temperature is due to only the exponential term and σ_∞ is the conductivity at infinite temperature, defined as:

$$\sigma_\infty = P_a \cdot P_d \left(\frac{e^2v}{ckT}\right) \tag{1.6}$$

However, for thermistors resistivity is more often used, being the inverse of conductivity $\rho = (1/\sigma)$, resistivity is therefore given by equation 1.7

$$\rho = \rho_\infty e^{\left(\frac{q}{kT}\right)} \tag{1.7}$$

Similarly, resistivity at infinite temperature ρ_∞ is given by equation 1.8.

$$\rho_\infty = \frac{ckT}{P_aP_de^2v} \tag{1.8}$$

1.4.5. Important Parameters for NTC Thermistors

In general, there are two categories of thermistor characteristics:

1. Characteristics of the semiconductor material (e.g. resistance vs temperature curves, B-value, Temperature Coefficient of Resistance values).
2. Characteristics mainly determined by the physical shape, size or mode of encapsulation (e.g. voltage vs current curves, time constant, dissipation factor).

This section will look into some thermistor characteristics that are important for the practical application of thermistors.

Resistance vs Temperature Characteristics

An NTC thermistor material is largely characterised by its resistivity, given by equation 1.7 and 1.8. However, for thermistors of a given dimension, resistance (R and R_∞) is often used over resistivity (ρ and ρ_∞). Also, a constant B [$°K$] is used as an expression of the combined terms of activation energy (q) and the Stefan-Boltzmann constant (k) so that $B = q/k$. This constant is commonly called the NTC thermistor *thermal constant* or *B-value*, or *B factor*. The resistance at infinite temperature R_∞, the counterpart of ρ_∞, is also typically denoted as a constant A, so that $R_\infty = A$. Hence, the resistance of a thermistor device is expressed by equation 1.9.

$$R = A\ exp\left(\frac{B}{T}\right) \tag{1.9}$$

When using equation 1.9 to plot the resistance (or resistivity) versus temperature curve, often the plot uses the logarithm of resistivity ($log(\rho)$) and the reciprocal of the absolute temperature ($1/T$) to produce a linear curve, also called an Arrhenius plot. An example of which is given in figure 1.9 where Verwey *et al.* [55] were the first to demonstrate how manipulating the chemical doping of a Fe_3O_4 – $MgCr_2O_4$ system could control the desired B-values and resistivity of the NTC material.

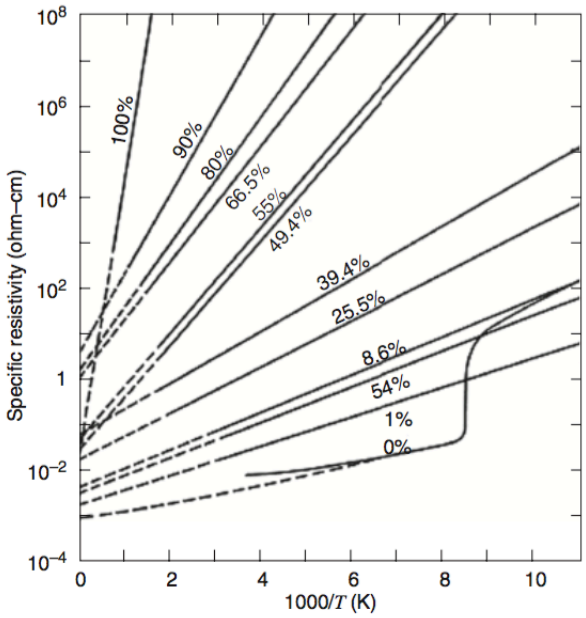

Figure 1.9: Resistivity versus Temperature Curve of Fe_3O_4 – $MgCr_2O_4$ with varying percentage of the addition of $MgCr_2O_4$ to tailor the NTC thermistor B-value and temperature coefficient of resistance. (taken from [17])

As seen in figure 1.9, the curves are linear, however for the curve of 0% at higher temperatures the slope of the curve starts to change which is characteristic for many materials. This led to the empirical equation 1.10 that better fitted experimental results which added a constant term θ [$°K$].

$$R = A\ exp\left(\frac{B}{T+\theta}\right) \tag{1.10}$$

B-Value or Thermal Constant

As previously described the B-value or Thermal Constant of an NTC thermistor is a value that helps characterise it's resistance versus temperature behaviour according to equation 1.9. It's value can be calculated through experimental results of resistance measurements at two specific temperatures, R_1 at T_1 and R_2 at T_2. Using equation 1.9, the equation of the B-value can be derived in the following:

$$R_1 = A\ exp\left(\frac{B}{T_1}\right) \qquad R_2 = A\ exp\left(\frac{B}{T_2}\right)$$

By dividing both equations:

$$\frac{R_1}{R_2} = \frac{Ae^{\frac{B}{T_1}}}{Ae^{\frac{B}{T_2}}}$$

$$ln\left(\frac{R_1}{R_2}\right) = ln\ e^{\left(\frac{B}{T_1}-\frac{B}{T_2}\right)} = \left(\frac{B}{T_1}-\frac{B}{T_2}\right) = B\left(\frac{1}{T_1}-\frac{1}{T_2}\right)$$

$$ln\left(\frac{R_1}{R_2}\right) = B\left(\frac{1}{T_1}-\frac{1}{T_2}\right)$$

$$B = \frac{ln\left(\frac{R_1}{R_2}\right)}{\left(\frac{1}{T_1} - \frac{1}{T_2}\right)} \tag{1.11}$$

Hence the B-value of an NTC Thermistor can be calculated from experimental resistance measurements using equation 1.11. However, the calculated B-value can change for the same system depending on what T_1 and T_2 temperatures are chosen. To have B-values that are comparable between different material systems the same T_1 and T_2 temperatures need to be chosen, this is usually $25°C$ and $100°C$.

A typical spinel-based NTC ceramic thermistor used in industry has a B-value between 2000-5000 K, that has a corresponding temperature coefficient of resistance, α ranging from -2.2 to -5.5%/K at room temperature [17]. As a general rule, high B-value thermistors find applications in temperature sensing, while low B-value thermistors find applications in circuit compensation and cryogenic temperature sensing.

Temperature Coefficient of Resistance

The temperature coefficient of resistance α is the ratio of the rate of change of resistance with temperature to the resistance at a specific temperature with units of [% per $°C$].

$$\alpha = \frac{\text{rate of change of resistance with temperature}}{\text{resistance at a specific temperature}}$$

The temperature coefficient of resistance α can be derived mathematically in the following:

$$\alpha = \frac{d}{dT}\left[R = A\ exp\left(\frac{B}{T}\right)\right]$$

$$\alpha = \frac{d}{dT}\left[ln(R) = ln\left(Ae^{\frac{B}{T}}\right)\right]$$

$$\alpha = \frac{d}{dT}\left[ln(R) = ln(A) + ln\left(e^{\frac{B}{T}}\right)\right]$$

$$\alpha = \frac{d}{dT}\left[ln(R)\right] = \frac{d}{dT}\left[ln(A)\right] + \frac{d}{dT}\left[\frac{B}{T}\right]$$

$$\alpha = \frac{1}{R} \cdot \frac{dR}{dT} = \frac{-B}{T^2} \tag{1.12}$$

Therefore, the temperature coefficient of resistance α is given by equation 1.12 with units of [% per $°C$]. Hence, α and B-values are both parameters used to characterise and compare NTC thermistors, but these two parameters are directly related to each other and one cannot change one without changing the other.

$$B = \frac{ln\left(\frac{R_1}{R_2}\right)}{\left(\frac{1}{T_1} - \frac{1}{T_2}\right)} \qquad \alpha = \frac{1}{R} \cdot \frac{dR}{dT} = \frac{-B}{T^2}$$

1.5. Literature Review of Flexible Temperature Sensors

When surveying literature for recent advancements in flexible temperature sensors (specifically flexible thermistors) many recent studies have used different architectures and materials that enable flexibility. Two trends from literature have emerged in the pursuit to develop flexible temperature sensors:

1. Use conventional thermistor material → Develop new architecture to allow flexibility
2. Use new unconventional, intrinsically flexible thermistor material → Improve thermistor performance

Hence, flexible temperature sensors are attempted either through the smart mechanical re-design of active and nonactive materials to form new device architectures (e.g. functional granular composites or thin-films), or by using intrinsically stretchable active materials (e.g. conductive polymer or graphene). In any case, the device architecture and material choice have to be taken in concert. A summary of flexible temperature sensors found in recent literature are presented in tables A.1 and A.2 in appendix A to provide the reader with a broad overview. A few of the most relevant concepts will be discussed in greater detail, but in summary, the types of flexible thermistors reviewed were:

1. Non-Flexible NTC element with Flexible Polymer
    - Functional Granular Composites (active filler in polymer matrix)
        - Spherical Particles
        - Aggregated Particles (i.e. Clusters)
        - Crumpled sheets (thin platelets)
        - Fibres
    - Thin-film lay ups (thin-film of active NTC material and thin-film of polymer substrate)
        - Flat stacked or through layers
        - Corrugated, wavy layers
        - Serpentine thin-film design
2. Flexible NTC Element with Flexible Polymer
    - Thin-film lay-ups
    - Pairing with conductive polymer (e.g. Graphene with PEDOT:PSS)

Within recent literature, conductive composites have been widely explored [30], however the use of NTC ceramic materials as fillers in polymer matrices has, to the best of our knowledge, not been well explored. Deutz [13] investigated the use of NTC nickel-manganite spinel particles in an epoxy matrix, using the concept of functional granular composites where particles of ceramic NTC material were added to a polymer matrix to form a percolated network. In theory, they could have the electrical characteristics of the ceramic material and the mechanical flexibility of the polymer. Deutz mainly investigated the effect of the filler volume fraction on composite resistivity (15-50 vol% filler), the effect of structuring the filler particles (using dielectrophoresis turning 0-3 to 1-3 composites), and the effect of agglomerating filler particles (particle diameters of 1-10 μm and agglomerates diameters of 10-100 μm). Deutz's findings, summarised in figure 1.10a, show that at high filler volume of NTC particles (up to Φ_c = 50%) the resistivity of the NiMnO-Epoxy composite was still very high and behaved similarly to a pure epoxy system. Similarly, figure 1.10b also shows that at high filler volume of NTC particles the corresponding B-value is still low, similar to the pure epoxy system.

Hence, a composite with conductivity and B-value similar to the bulk ceramic cannot be produced simply by increasing the filler volume fraction alone. An attempt was made to better structure the particles into a percolated network using dielectrophoresis (DEP) to increase the conductivity. However, it is evident from figure 1.10a that structuring on spherical particles of 1-10 μm in size did little to lower the overall resistivity of the composite. Only when inhomogenousley dispersed agglomerates of NTC material were used, at high filler volumes, did the composite have a conductivity and B-value closer to the bulk ceramic. This system was the most conductive where the composite had a resistivity on the order of $10^5\ \Omega cm$ and a B-value of about 1500 K at a filler volume content of $\approx$ 45 vol%. This study suggests that functional granular composites can be successful, but not with homogeneously dispersed, small spherical filler particles. Instead, agglomerated particles or high aspect ratio particles (e.g. fibres) are needed.

Similar to the approach of using functional granular composites by Deutz, Murugaraj et al. [43] created a composite thermistor of carbon nanoparticle fillers in a polyimide matrix. Spherical filler particles of 30 nm were used at varying volume fractions of 1-10 vol%. Unfortunately, the thermal sensitivity parameters (B-value and α) are very low (by orders of magnitude) compared to commercially available ceramic-based thermistors. Khan et al. [23] also took the same approach using NiO nanoparticles mixed with polystyrene-butadiene rubber (PSBR) binder. A conductive composite ink was created and stencil-printed as a thin-film onto kapton polyimide. The B-value and α were high, but the mechanical flexibility achieved was low.

Other researchers like Huang et al. [21] went for the simple thin-film approach using a very thin layer of NiO as the NTC material deposited on a flexible substrate of polyimide film. The design takes a conventional well performing NTC thermistor material and produces it as a thin-film so that its bendable (to a degree) and supported on a flexible polymer substrate. However, the mechanical flexibility is very limited since the thin-film NiO thermistor cannot survive a bend test of radius 0.5 cm and fails catastrophically by exfoliation. Yu et al. [61] adapted the simple thin-film approach and made the thin-film element a wavy (corrugated) buckled thin-film, supported by a PDMS substrate so that it enables

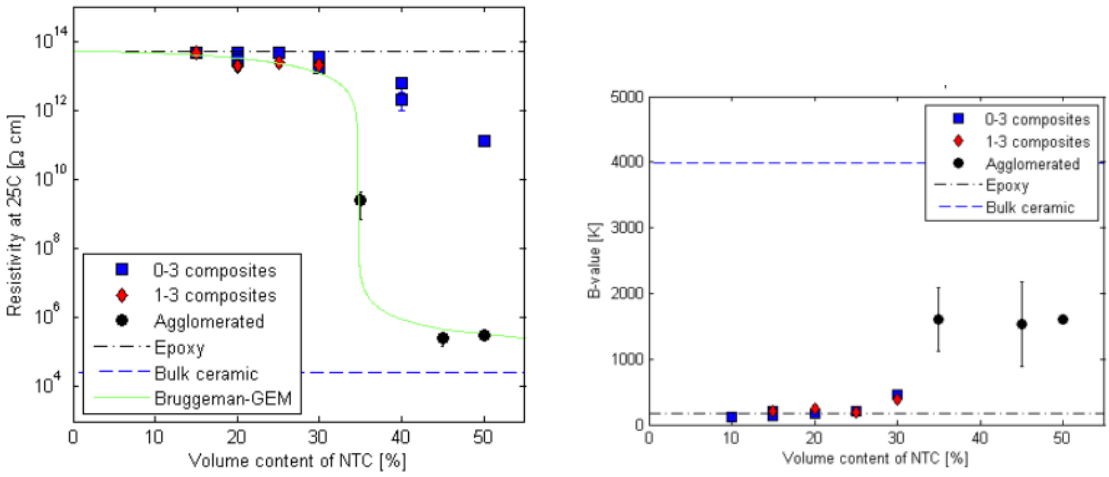

(a) Resistivity vs Filler Volume Content

(b) B-value vs Filler Volume Content

Figure 1.10: Resistivity and B-value vs filler volume content of NiMnO particles in NiMnO-Epoxy composites [13]

reversible stretching and compression up to 30% strain with unchanging performance. Although the active thermistor material used was a positive temperature coefficient (PTC) material, the architecture and production method that enabled mechanical flexibility is very interesting and could potentially be applied to NTC materials.

Alternatively, other researchers took a different approach and avoided ceramic based materials lacking mechanical flexibility, instead using novel materials that can perform as a NTC while also being intrinsically flexible. Yan et al. [59] used a graphene-based thermistor to try to achieve a temperature sensor that can withstand very high strains (higher than 30%), beyond the smaller strains usually induced with moderate bending (usually below 1% [59]). Yan et al. [59] used crumpled graphene sheets stitched together with nanocellulose fibril, forming a conductive network within a polymer matrix of polydimethylsiloxane (PDMS). It is mechanically flexible and robust, but its temperature sensing properties, specifically sensitivity, is inferior to ceramic based devices (most ceramic materials have B-values = 3000-5000 K, while the unstretched graphene-based thermistor has a B-value of 945 K [59]). Kong et al. [24] also used graphene as the stretchable NTC material but used inkjet printing to deposit graphene layers onto flexible substrates of polyethylene terephthalate (PET). A trend is evident where the performance as a temperature sensor is low when the mechanical flexibility achieved is high. The same trend was reinforced by Bendi et al. [6] who used graphene on a thin-film of poly[(vinylidenefluoride-co-trifluoroethyle)] (PVDF-TrFE) and by Vuorinen et al. [56] who produced a composite system of graphene and the conductive polymer poly(3,4-ethylenedioxythiophene): poly(styrenesulfonate) (PEDOT:PSS).

1.5.1. Conclusions Drawn From Literature Review

The literature review of the state-of-the-art in flexible temperature sensors shows that researchers are following two general trends. The first trend is to use well-established thermistor materials (e.g. ceramic metal-oxides) that already perform well and try to develop device architectures that enable flexibility. This is done through functional granular composites, thin-film lay ups, corrugated or serpentine thin film shapes. Many researchers are producing impressive devices with good thermistor performance (high sensitivity and response speed, and low fabrication cost), but mechanical flexibility is limited, and stretchability is an issue. This is especially true for thin-film architectures that have poor adhesion to the substrate and are limited in bending (they can bend to a degree, but cannot be stretched in-plane) and fail by exfoliation.

The second trend is to use novel, inherently stretchable thermistor materials (e.g. graphene and conductive polymers) which can also capitalise on new and efficient production techniques like inkjet printing and screen-printing. Many researchers are producing very stretchable thermistor devices, but the manufacturing process can be difficult and/or expensive, but more importantly, the thermistor performance is sub-par (specifically low sensitivity, B-value and temperature coefficient of resistance). Moreover, using conductive polymers has other drawbacks, like high manufacturing costs, instability,

and high moisture sensitivity [33].

These drawbacks led many researches to use more conventional thermistor materials with good electrical properties and develop novel twists to enable flexibility through mechanical design. This thesis work wants to capitalise on the benefits of ceramic-based thermistors because of their key advantages in having low fabrication cost, high sensitivity, and high response speed [59], and investigate ways to enable mechanical flexibility and stretchability. Polymer-ceramic composites are very promising, as seen by the work of Deutz that uses the concept of functional granular composites, which will be further examined in the next section.

1.6. Functional Granular Composites FGC

In literature, there are many studies that look into piezoelectric ceramic-polymer composites. What is learnt from these studies can be directly extrapolated to a potential thermistor ceramic-polymer composite, where active temperature sensing ceramics are combined with the flexibility of non-active polymers to produce functional granular composites (FGC). Many of the techniques and methods will be the same, but they may have to be adapted to accommodate the substitution of the active element from being a piezoelectric ceramic to a conductive ceramic.
The following subsections will address some of the factors and issues that will affect the overall conductivity of a composite thermistor and therefore need to be taken into account in its design.

1.6.1. Connectivity

If we consider a composite that is comprised of two distinct phases, each phase may be self-connected in any combination of the 3 dimensions. Newnham *et al* [46], created the conventional terminology to describe the connectivity of the phases in a binary composite; a two digit number e.g. 0-3. The first digit denotes the connectivity of the filler material (e.g. ceramic) in the 3-dimensions (x,y,z, directions) while the second denotes the connectivity of the matrix (e.g. polymer) in the 3-dimensions (x,y,z, directions). According to [46], there are 10 different possibilities of how the two phases can be self-connected: 0-0, 1-0, 2-0, 3-0, 1-1, 2-1, 3-1, 2-2, 3-2, 3-3. These 10 possibilities are graphically illustrated in figure 1.11. Practical examples of how some of these connectivity options can be produced as a ceramic-polymer composite are given in figure 1.12.

In practice, composites with 3-3 connectivity would be comparatively more difficult and costly than producing composites of 0-3 or 1-3 composites. Hence, many studies have focused on producing 0-3 or 1-3 composites through the dispersion of particles or fibres of the active material within a polymer matrix. The following section will discuss the role of percolation in random and segregated functional granular composites.

1.6.2. Percolation Theory

To understand percolation theory an example is necessary, take copper - polyvinylchloride (Cu-PVC) composites as an example towards a conductor-filled composite. The Cu particles are the conductive filler material and the PVC is the non-active matrix material. At low volumes of filler added to the matrix, the properties of the matrix material dominate the overall properties of the composite. However, with increasing volumes of filler added the copper particles begin to contact one another and form a conductive network within the polymer matrix. The critical volume fraction at which the filler particles form a conductive network, denoted v_f, is commonly referred to as the percolation limit. The percolation limit is clearly visible when the electrical conductivity of the composite is plotted against the volume fraction of the conductive filler, as can be seen in figure 1.13a. Before the percolation limit, the composite conductivity is characterised by the polymer. Near the percolating limit, the conductivity is characterised by the thin layers of polymer that lie in between the conductive filler particles. After the percolating limit, the conductivity is characterised by the conductive filler particles that are in contact with each other.

Factors Affecting the Percolation Limit

Standard percolation theory normally models the filler-matrix composites as isometric matrices that are randomly filled by particles based on statistical probabilities. However, in reality the distribution of filler particles are not random and the conductivity pattern is not isometric. Many researchers have looked

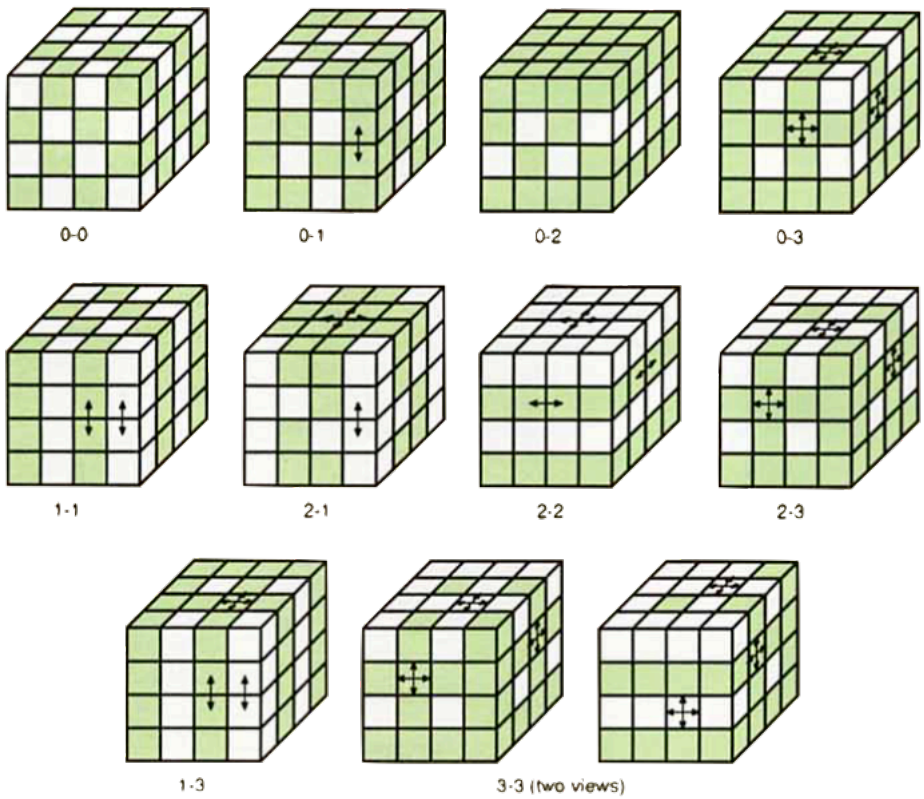

Figure 1.11: Possible connectivity patterns of a 2-phase composite [36]

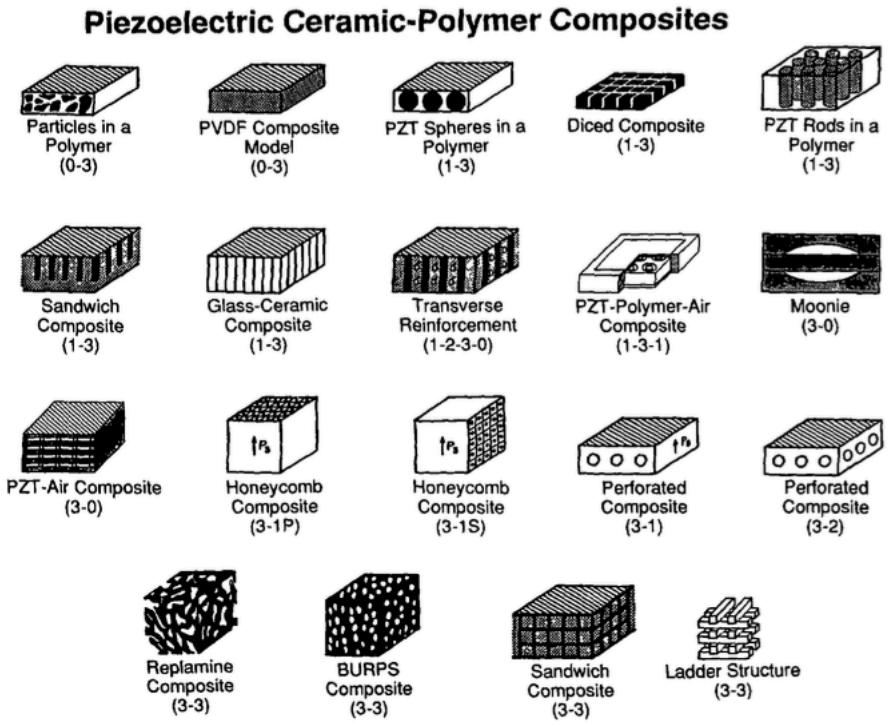

Figure 1.12: Examples of piezoelectric ceramic-polymer composites with different connectivites [52]

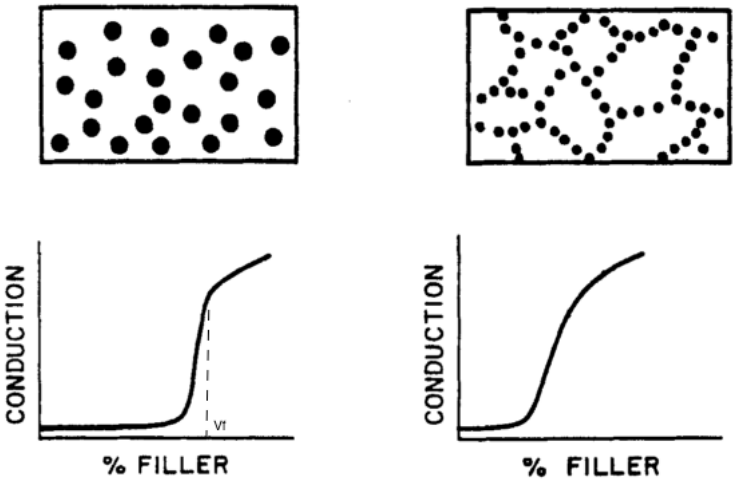

(a) Filler particle size ≅ Matrix particle size(b) Filler particle size < Matrix particle size

Figure 1.13: Determining the percolation limit from the plot of electrical conductivity of the composite versus the volume fraction of the conductive filler. The percolation limit is smaller when the ratio of filler particle size to matrix particle size is large [45]

into the critical volume fraction at which the filler particles form a conductive network, v_f (also called the percolation limit) for many different conductive composites. Table 1.2 is taken from [51], where it is evident that for some of the very same composite systems the percolation limit (denoted V_c in this study) experimentally determined was different. This is evidence that there are many other factors that affect the percolation limit, some of which are addressed in the following:

Table 1.2: Critical Volume Fractions for Conductive Composite Systems [51]

Filler	Polymer	V_c
Cu	Polyvinylchloride	0.01
Cu	Polyvinylchloride	0.20
Cu	Polystyrene	0.15
Cu	Polystyrene	0.35
Ag	Polystyrene	0.36
Ag	Rigid Epoxy	0.09
Ag	Rigid Epoxy	0.30
Ag	Silicone Rubber	0.15
Ag	Silicone Rubber	0.27
$Sb:SnO_2$	Flexible Epoxy	0.30
$Sb:SnO_2$	Flexible Epoxy	0.40
Fe	Styrene / acrylonitrile	0.20
Al	Styrene / acrylonitrile	0.40

One crucial factor is the influence of the size ratio of the filler particles to the matrix particles. If the filler particles are substantially smaller than the matrix particles, they will be forced into the interstitial sites created by the larger matrix particles. The effect would be the creation of a conductive network at a relatively lower amount of filler particles, thus decreasing the critical volume fraction or percolation limit. This effect is illustrated in figure 1.13b, which has a larger matrix particle size than filler particle size and therefore a lower percolation limit than if matrix and filler where of equal size, as seen in figure 1.13a. Hence, if we keep the matrix particles the same, decreasing the filler particle size lowers the V_f

needed for percolation. This is illustrated schematically in figure 1.14

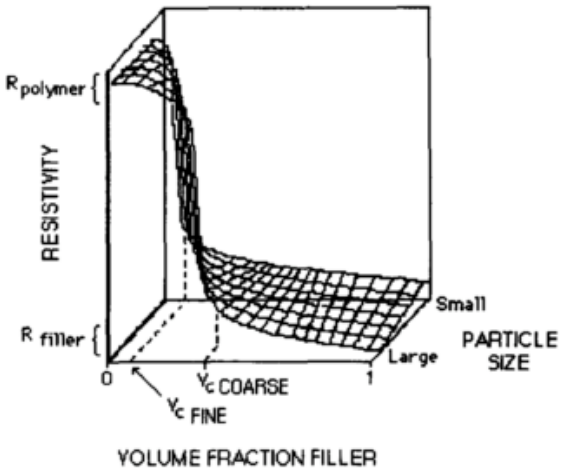

Figure 1.14: Effect of varying filler particle size on the percolation curve of a conductive composite (V_c is equivalent to V_f) [51]

Another important variable is the geometry factor, G which is given by equation 1.13, that helps to characterise the effect the size and shape of the overall composite has on the percolation limit. The geometry factor, G is basically the ratio of the area of the electrode contact ($A = w \cdot t$) vs the length between the electrodes (L). If you decrease the value of G (by decreasing A and/or increasing L), illustrated by figure 1.15b, the percolation limit or critical volume fraction of filler required for conduction is higher. This was proven experimentally by [51] and depicted in figure 1.16a where the thickness of the sample was decreased (thus decreasing A), decreasing G and consequently increasing the critical volume fraction of filler needed for percolation. This can be explained when looking at the probability that a filler particle will fill an adjacent lattice site, the probability of continuing a percolation path is greater for a particle in the bulk of the composite than for a particle at the surface [51]. This is due to the greater amount of adjacent lattice sites available for bulk particles so that the conductive path can continue.

The effect that sample geometry has on the percolating limit is less pronounced when the particle size is smaller in relation to the sample thickness. This can be seen in figure 1.16b whereby smaller filler particles are used and the thickness of the sample is again decreased, decreasing the G, and consequently increasing the percolation limit. However, the increase in the percolation limit is not as drastic due to the smaller particle size used. This is where the second geometry factor can be introduce, Γ which is given by equation 1.14 and is basically the ratio of the smallest sample dimension to the particle size. The smallest sample dimension is typically the thickness dimension for thin, flexible sheet-type conductive composites. The larger the particle size in relation to the sample's dimension, the more particles will occupy positions at the surfaces rather than in the bulk [51]. As mentioned before, particles at the surface have lower probability of continuing a percolation path.

$$G = \frac{A}{L} = \frac{\text{Area of Electrode Contact}(A = w \cdot t)}{\text{Length between electrodes}} \tag{1.13}$$

$$\Gamma = \frac{t}{d} = \frac{\text{the smallest sample dimension}}{\text{diameter of filler particle}} \tag{1.14}$$

To summarise:

- Low geometry factors G ($G \leqq 1.0cm$ [51]) are unfavourable geometries for percolation, especially when Γ is small ($\downarrow \Gamma = \frac{\downarrow t}{\uparrow d}$).

(a) Normal Value of G (b) Higher value of G

Figure 1.15: Changing the geometry factor of a conductive composite sample [51]

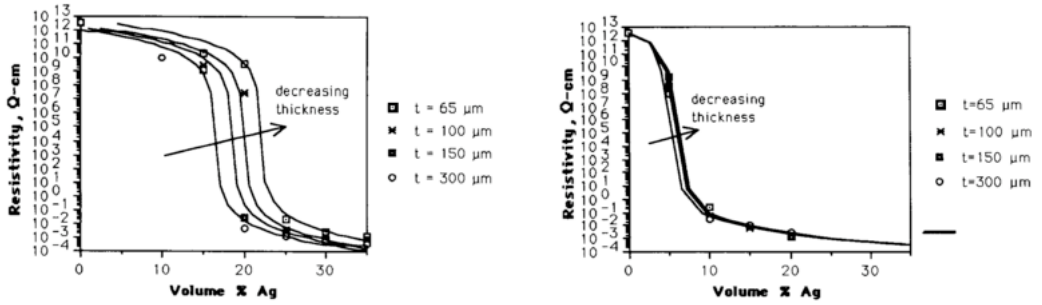

(a) $9.0\mu m$ Ag powder-filled silicone rubber composites (b) $0.5\mu m$ Ag powder-filled silicone rubber composites

Figure 1.16: Percolation curves showing the effect of increasing the geometry factor (by lowering sample thickness) and its effectiveness to alter the percilation limit when smaller particle sizes are used (graphs taken from [51])

- Large geometry factors G ($G \geqq 1.0cm$ [51]) are favourable geometries for percolation.

This is visually illustrated in figure 1.17, where the geometry factor is plotted against the critical volume fraction for percolation. It becomes evident that higher values of G enable lower V_f of filler required for percolation. Also, higher values of Γ by using smaller filler particles also enable lower volume fractions of filler particles required to achieve percolation.

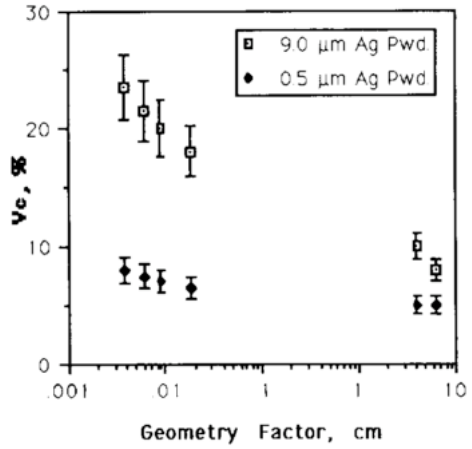

Figure 1.17: Change in critical volume fraction V_c or percolation limit due to a change in geometry factor $G = \frac{A}{t}$ and the influence of $\Gamma = \frac{t}{d}$ [51]

Lastly, another factor that effects percolation in conductive composites is the particle shape. Non-spherical particles have a greater tendency to bridge and result in lower volumes of filler particles needed to create a conductive network. Bridging is very significant in lowering the percolating limit and V_f when fibres and flakers are used [51].

Knowing the factors that effect percolation and how to reduce the V_f of conductive filler particles is extremely important for manufacturing and performance reasons. For a desired performance, if the amount of conductive filler can be reduced it can offer more benefits, inherent to the particular composite system chosen. If the polymer was chosen for its price, mechanical flexibility, durability or other features, using less filler particles potentially would enable the composite properties to be closer to the polymer's properties. E.g. a more flexible thin-film thermistor can be achieved from a conductive composite that has a lower filler volume fraction of conductive ceramic. Moreover, conductive ceramics are technical ceramics and are usually more laborious and expensive to make, so using lower amounts of them translate directly to cost savings.

1.6.3. Coefficient of Expansion Mismatch in Composites

The behaviour of a composite thermistor with varying temperature can be complicated by the mismatch in thermal expansion of the constituents. If a composite thermistor is formed with the volume of conductive filler near the percolation limit, at low temperatures the behaviour would be characterised by the properties of the conductive filler. If the conductive filler is an NTC ceramic, the composite will behave like an NTC material. For example, carbon particles dispersed in a polyethylene matrix. However, at increasing temperatures the polymer may expand more rapidly then the ceramic particles, effectively pulling the particles apart and discontinuing the conductive network, thus lowering the composite's conductivity. The composite thermistor at high temperatures then can act as a PTC thermistor, despite having NTC ceramic filler material. Therefore, a NTC-PTC thermistor is possible, albeit under certain conditions, which should be considered when designing a composite thermistor.

1.6.4. Modelling the Resistivity of Composite Conductors

When sufficient conductive particles are added to a polymer matrix percolated networks form that create conductive pathways. When modelling, it is incorrect to assume each conductive pathway acts similar to a conductive filament. Electrically, they behave like many resistors placed in series. The total resistance of a composite conductor is a function of mainly three independent contributions:

- The constriction resistance at the contacts
- The tunnelling resistance at the contacts
- The intrinsic filler resistance of each particle

Where the tunnelling resistance is typically the most dominant contribution to the overall resistance of the composite. The overall resistance of a composite conductor, R_c can be characterised by equation 1.15, devised by Yasuda and Nagata.

$$R_c = 2R_e + \frac{(M-1)R_p + MR_i}{N} \tag{1.15}$$

Where,

- R_c is the composite resistance
- R_e is the lead resistance to the electrodes
- R_p is the particle-particle contact resistance
- R_i is the intrinsic resistance of each particle
- M is the number of particles that form a single conductive pathway
- N is the number of conductive pathways

Yasuda and Nagata's equation is based on their model that has a few underlying assumptions that are critical to note. Firstly, it was assumed that the maximum number of filler particles are added to the polymer matrix. This was assumed so that the conductive composite can be modelled as a conductive

skeleton of simple cubic packing of filler particles in a polymer matrix. Hence, the filler volume fraction is high enough to avoid the percolation threshold effects. Furthermore, the filler particles are assumed to be of the exact same size and are spherical in shape to allow for simply cubic packing, as illustrated in figure 1.18 for a conductive composite of length L, width w, and thickness t.

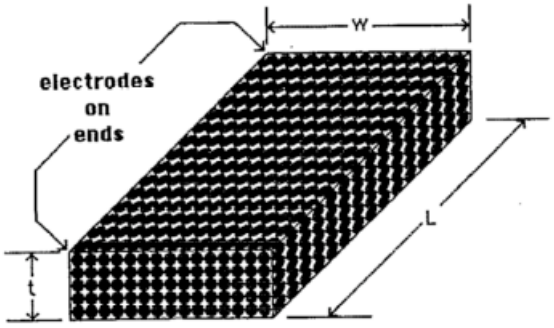

Figure 1.18: Simple cubic packing of conductive filler particles in a polymer matrix [50]

Considering the ideal model of simple cubic packing of filler particles as presented in figure 1.18, each filler particle in the cross section along the width of the composite, represents one path of conduction through the length of the composite. Therefore, the number of conductive pathways, N, can be calculated from equation 1.16:

$$N = \frac{wt}{d^2} \tag{1.16}$$

Where wt is the cross sectional area of the composite and d is the diameter of filler particles, so d^2 is the cross sectional area of one chain with its surrounding insulation. Then, the number of particles that form a single conductive pathway, M (through the length of the composite) is given by equation 1.17.

$$M = \frac{L}{d} \tag{1.17}$$

Where L is the length of the composite and d is again the diameter of the filler particles. [50] admits that this model is very idealistic and that actual samples will use much lower filler volumes and hence conductive pathways will be more irregular and curvy, but these assumptions are necessary to build a model for comparison purposes. From equation 1.15 one can note that the important factors to consider is the particle-particle contact resistance (R_p) and the intrinsic resistance of each particle (R_i). The lead resistance to the electrodes (R_e) is less important because it can be eliminated by using a four-point-probe resistance measurement [50]. Between the two resistances R_p and R_i, R_p is generally the more dominant resistance and will be subject of the following subsection.

Particle-Particle Contact Resistance, R_p

As mentioned earlier, the total resistance of the conductive composite is a summation of the constriction resistance at the contacts, the tunnelling resistance at the contacts, and the intrinsic filler resistance of each particle. The first two comprise the particle-particle contact resistance, so that R_p is given by equation 1.18 where both components will be addressed in the following section.

$$R_p = R_{cr} + R_t \tag{1.18}$$

Constriction Resistance

Constriction resistance R_{cr} is the resistance caused by the constriction of the electron flow between two spheres that touch where the area of contact is small. This constriction of conductivity is characterised by equation 1.19.

$$R_{cr} = \frac{\rho_i}{d} \tag{1.19}$$

Where d is the diameter of the contact spot and ρ_i is the intrinsic resistivity of the filler particles. Moreover, this equation is valid when the ratio between the particle diameter D and contact spot diameter d is not too large. When the particle diameter is much larger than the contact spot diameter so that $D/d > 10$, the resistivity from constriction diverges form equation 1.19 and is so large, almost all conductivity is lost.

Tunnelling Resistance

Tunnelling resistance is the resistance associated with any insulating film that may exist between two conducting particles, usually as insulating films that are coated on the filler particles. The three most common sources of films that can be present in varying thickness on filler particles that act as an insulating layer are:

- Oxide films or tarnish films that usually form on metal particles.
- Residual organic films usually on processed powders that can remain after processes like milling.
- The matrix polymer itself that covers the conductive particles and exist in between two otherwise contacting particles.

According to quantum-mechanical tunnelling, the probability that an electron will tunnel through a potential barrier is proportional to the work function of the conductor, the film's thickness, and the relative dielectric permittivity of the film. Unintutiviely, the resistivity of the film is not a factor, so similar tunnelling resistivities are found for films of organics, polymers and oxides which have similar work functions, thicknesses and dielectric permittivities [50]. The tunnelling resistance of contact in a conductive composite can be characterised by equation 1.20.

$$R_t = \frac{\rho_t}{a} \tag{1.20}$$

Where a is the area of the contact spot and ρ_t is the tunnelling resistivity of the contact. This ρ_t can be determined if the thickness of the insulating film is known since Dietrich [50] had derived an empirical relation for the dependence of tunnelling resistivity on the thickness of the insulating film that can be applied to all materials (the relation was empirically derived from TiO_2 films on Ti).

Hence, substituting equation 1.19 and 1.20 into 1.18 gives the new equation that describes the particle-particle contact resistance, R_p

$$R_p = \frac{\rho_i}{d} + \frac{\rho_t}{a} \tag{1.21}$$

Contact Spot Area

Equation 1.21 describes the particle-particle contact resistance, R_p which is generally the dominating resistivity contribution to the overall resistivity of the composite conductor, characterised by equation 1.15. The equation is dependent on both the diameter and area of the circular contact spot between two spheres that touch. This actual contact spot is a function of the applied pressure placed on the spheres and the resulting deformation that occurs. This deformation has both an elastic and plastic element. According to [50], the contact spot area between two spheres that touch is fairly well determined by equation 1.22 where plastic deformation occurs, and equation 1.23 where purely elastic deformation occurs.

$$a_{plastic} = \frac{a}{H} \tag{1.22}$$

$$a_{elastic} = 2.43\frac{FD}{E}^{\frac{2}{3}} \tag{1.23}$$

Where F is the applied force on the particles, H is the contact hardness, D is the diameter of the spherical particles, and E is their modulus of elasticity. However, when plasticity occurs, it is usually accompanied by an elastic element, therefore for the case where both elastic and plastic deformation occurs, the contact area is simplified into equation 1.24.

$$a_{elastic-plastic} = \frac{F}{\xi H} \tag{1.24}$$

Where ξ is elasticity factor that ranges from $0.2 \leq \xi \geq 1.0$, 0.2 for purely elastic deformation and 1.0 for purely plastic deformation.

Therefore, when looking back at equation 1.18 that describes the particle-particle contact resistance, R_p

$$R_p = \frac{\rho_i}{d} + \frac{\rho_t}{a}$$

This equation can be updated for the a and d terms that describe the contact spot area and diameter which are a function of the applied pressure between particles and the resulting deformation that occurs for the plastic (with some elastic) deformation case, given by equation 1.25 and the purely elastic deformation case, given by equation 1.26.

$$R_{p(plastic)} = 0.89\rho_i(\frac{\xi H}{F})^{\frac{1}{2}} + \rho_t\frac{\xi H}{F} \tag{1.25}$$

$$R_{p(elastic)} = 0.57\rho_i(\frac{E}{FD})^{\frac{1}{3}} + 0.26\rho_t(\frac{E}{FD})^{\frac{2}{3}} \tag{1.26}$$

Conclusions from the models

The overall models and equations presented here to help characterise the resistivity of conductive composites are based on an ideal model that isn't very applicable to a real-life conductive composite. These idealised assumptions are summarised in the following:

- The maximum number of filler particles are added to polymer matrix, avoiding percolation threshold effects.
- The filler particles are arranged as a conductive skeleton of simple cubic packing through the entire composite.
- The filler particles are all the same size and are perfectly spherical.
- All the filler particles are involved in conduction and conductive chains are all straight, without dead ends or nonpercolated members.
- The contact force and tunnelling resistivity is the same for all particles.
- Conduction through regions other than at particle-particle interfaces along a chain are insignificant contributions to the overall resistivity.

Thus the equations presented therefore may not accurately characterise real-life conductive composites to which the aforementioned simplifying assumptions are not valid. However, they are extremely valuable relations because they still describe the factors that affect resistance and enable qualitative comparisons to which factors are most influential. Furthermore, the relations enable a quantitative way to compare different filler materials which is extremely valuable for design purposes for producing conductive composites.

In summary, some of the design lessons learned from the characteristic equations are:

- Resistivity increases with higher filler hardness, elastic modulus, and larger insulating film thickness.
- Resistivity decreases with increasing particle size, and intrinsic stress.

This leads to the conclusion that highly conductive composites are attained by using soft, large filler particles and by inducing mechanical stress, possibly by having a polymer matrix that undergoes large shrinkage. Also, particles with higher aspect ratio, i.e. fibres, would be better in conduction since it minimises the amount of particle-particle contacts for a given length.

1.6.5. Modelling the Resistivity of Composite Thermistors

As described in section 1.6.4, the total resistance of a composite conductor R_c is a function of the constriction resistance at the contacts, the tunnelling resistance at the contacts, and the intrinsic filler resistance of each particle that follows the relation given by equation 1.15, devised by Yasuda and Nagata. This relation is repeated below:

$$R_c = 2R_e + \frac{(M-1)R_p + MR_i}{N}$$

Where the particle-particle contact resistance was described by equation 1.18 and equation 1.21, repeated again below for the reader's convenience.

$$R_p = R_{cr} + R_t = \frac{\rho_i}{d} + \frac{\rho_t}{a}$$

Where the intrinsic resistivity of the filler particles ρ_i for NTC ceramic filler material is described in section 1.4.4, and given by equation 1.7 and 1.8.

$$\rho = \rho_\infty exp^{\left(\frac{q}{kT}\right)} \qquad \rho_\infty = \frac{ckT}{P_a P_d e^2 v}$$

And the intrinsic resistance of the NTC particle R_i is given by equation 1.9.

$$R = A\ exp\left(\frac{B}{T}\right)$$

By combining all terms into equation 1.15 for the total resistance of a composite conductor that uses NTC filler material, the total resistance of a composite thermistor R_{ct} can be re-expressed in equation 1.27. The lead resistance to the electrodes R_e can be eliminated by using a 4-wire resistance setup and is therefore dropped.

$$R_c = \frac{(M-1)\left[\frac{\frac{ckT}{P_a P_d e^2 v}\cdot exp^{\left(\frac{q}{kT}\right)}}{d} + \frac{\rho_t}{a}\right] + M\left[A\ exp\left(\frac{B}{T}\right)\right]}{N} \tag{1.27}$$

Where,

- R_{ct} is the resistance of the composite thermistor
- M is the number of particles that form a single conductive pathway
- c is the unit cell dimensions [cm]
- k is the Stefan-Boltzmann's constant
- T is the absolute temperature [K]
- P_a is the probability that the adjacent B-site contains an acceptor cation
- P_d is the probability that the occupied B-sites contains a cation capable of donating an electron
- e is the charge of the charge carriers [coulombs]
- v is a frequency factor
- q is the hopping mechanism activation energy
- ρ_t is the tunnelling resistivity of the contact
- a is the area of the contact spot
- A is a constant equal to the resistance at infinite temperature R_∞ (counterpart of ρ_∞)
- B is the B-value of the NTC material ($B = q/k$) [k]
- N is the number of conductive pathways

1.7. Objective of the Thesis

The technology sector is moving towards flexible electronics with new fields emerging like wearable sensors for health monitoring. Towards this, there is a need to develop flexible sensors like temperature sensors. A literature review of flexible thermistors has highlighted the gap that there are no current systems, to the best of our knowledge, that can adequately satisfy both the mechanical and sensing performance demanded for commercial applications. The main research question of this thesis is then:

> *How can we produce a mechanically flexible temperature sensor with commercially desirable sensing performance by using composite materials of negative temperature coefficient (NTC) ceramics and polymers?*

This work aims to tackle this research question with a research objective to suggest a design for a mechanically flexible temperature sensor by designing a thermistor using functional granular composites that can have good thermistor performance (high sensitivity: B-value > 3000 K, and low resistivity: $\rho \approx 10^1 - 10^2\ \Omega cm$) while being mechanically flexible (surviving bending radii ≤ 1 cm over 100 cycles).

This work draws inspiration from the growing trend of using high aspect ratio particles like fibres as filler materials (e.g. silver nanowires embedded in polymer matrices to produce stretchable electrodes [20]). This architecture benefits from the general manufacturing simplicity of 0-3 functional granular composites, while being more effective at forming a conductive network than spherical particles. Switching to higher aspect ratio particles (e.g. fibres) makes forming a network easier, and lowers the amount of contact points. (This effectively agglomerates particles into larger high aspect ratio particles and lowers the role of constriction resistance through the lowering of the amount of contact points).

The work of Stuber [54], takes a similar approach where promising advancements have been made in using ceramic-fibres and polymer matrix composites for energy harvesting application. Stuber managed to produce a flexible ceramic-polymer fibre composite for energy harvesting applications. Potassium sodium niobate with 3 mol% lithium (KNLN3), with 5 mol% lithium (KNLN5), and PZT ceramic powders were used in a wet fibre spinning process that produced fibres that were sintered and embedded into a polymer matrix. This wet fibre spinning manufacturing technique can be adapted to a ceramic NTC thermistor system and will be the focus of this thesis work to ultimately produce a flexible temperature sensor using ceramic-fibre polymer-composites. Hence, a ceramic NTC material will need to be chosen where a metal-oxide based composition will ultimately be selected due to their advantages over other cutting edge materials (e.g. graphene) in low fabrication costs, high sensitivity, and high response speed. This thesis work is organised into the phases listed below with the intention to create the first fully flexible temperature sensor that can perform on par with conventional thermistors that can be immediately adopted into industry.

Phase

1. Tailoring NTC metal-oxide composition.
2. Characterisation of ceramic bulk properties.
3. Fibre Preparation.
4. Ceramic fibre - polymer matrix composites.
5. Stencil printed flexible thermistor composites.

2

Phase 1: Tailoring NTC metal-oxide composition

2.1. Introduction

It must be mentioned that existing NTC ceramic compositions, with their exact processing conditions, that are used in industry are kept as trade secrets. Almost all processing conditions affect the final performance of NTC ceramics and so processing conditions and techniques are just as important as the material composition. Due to its high commercial value, no reference NTC ceramic composition and processing conditions are available in Literature that produce a thermistor with commercially desirable properties (i.e. high sensitivity over a large temperature range, with high thermal stability and low resistance drift). Hence, this thesis work needs to select a NTC ceramic composition and processing conditions to firstly be able to produce bulk ceramics with adequate temperature sensing performance, before modifying the processing conditions to make NTC ceramic filler material for thermistor composites.

When choosing the active NTC material for the temperature sensing composite it is important to realise that many different material systems have potential, there is no single material system that is optimum with respect to all the important criteria involved for thermistors (e.g. resistivity, B-value, temperature coefficient of resistance, stability, etc.). All the material compositions currently used in industry have their strengths and weaknesses and choosing the right material system for a target application involves trade-offs. To illustrate, nickel manganite is a good basis for NTC materials that is widely used and relatively well understood and doping can be used to improve certain characteristics with trade-offs. Copper is effective at reducing the overall resistivity, but reduces the thermal stability. However, further doping can reduce or alleviate the problems in stability at the expense of something else (higher resistivity). Producing a NTC material that has desirable characteristics in all the relevant criteria for a thermistor that is desirable for industrial applications is a very difficult feat and an active area of research, somewhat beyond the scope of this thesis.

For wearable sensors in general, an ideal composite thermistor has low resistivity (at room temperature), but retains high/moderate sensitivities [48], i.e. high temperature coefficient of resistance and high B-value. This can be represented schematically on a resistance vs temperature curve shown in figure 2.1a. But for thermistor materials, having a low resistivity is usually coupled to having a low α and B-value.This is represented schematically by figure 2.1b.

This thesis will focus on producing a NTC material that has low resistivity as a filler material for a functional granular composite with a polymer matrix, that as a whole, can function as a thermistor with acceptably low resistivity and good mechanical flexibility. Hence an NTC material composition that gives low resistivity is desired. Low resistivity is prioritised because it is important from a design perspective. Resistivity is a dimensionless, intrinsic characteristic of a material, while the resistance depends on geometry and circuit design. If the material has a low intrinsic resistivity, and a higher

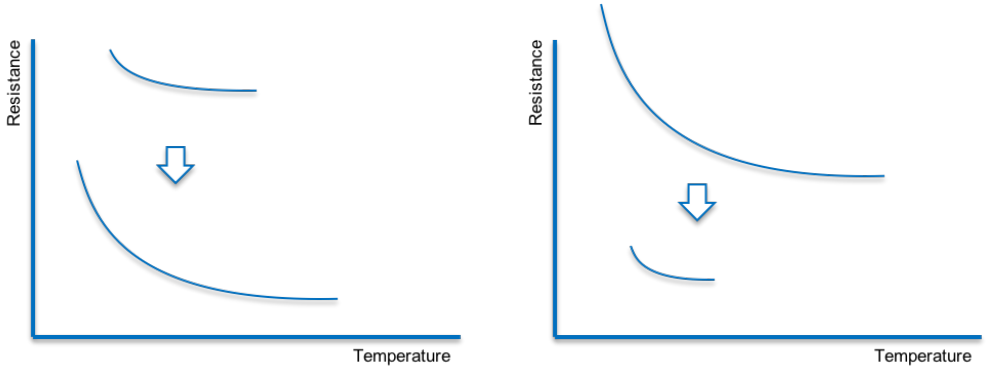

(a) Want low ρ_{RT} and high α and B-value

(b) Low ρ_{RT} is usually coupled to low α and B-value

Figure 2.1

resistance is desired, a longer length or smaller cross section can be used. However, if the material has a high resistivity and a lower resistance is desired, it is generally more difficult to attain a low resistance through the reduction of the geometry alone. Additionally, low resistance thermistors enable larger currents and are easier signals to detect allowing cheaper (lower fidelity) measuring devices. These are the main reasons a NTC composite thermistor with low resistivity is desired.

Furthermore, polymers that can provide good flexibility and compatibility with ceramic NTC filler particles are typically very intrinsically resistive. This is another reason why low resistivity is the criterion that is prioritised for the selection of the ceramic NTC filler material. In order to move forward, a composition will need to be chosen as the NTC material that will be used in a composite system of ceramic NTC in a polymer matrix system that can act as a flexible thermistor. Once a good basis is established, one can return to further improve on the nickel manganite based NTC material through doping with additional elements for improved characteristics (e.g. thermal stability). However, "Most of the industrial products are now manufactured with only three elements, which simplifies the manufacturing process, increases productivity, avoids having to manage a stock of many different raw materials, and limits the risk of irregularities in the quality of the supply" [49]. Although this was the view in 1994, at the time this study was published, it is relevant now to this thesis to aim to use 3 elements for the same reasons, since almost all the ceramic processing parameters affect the final electrical performance, and so the author can minimise the possibilities of irregularities to ensure the reproducibility of the final results.

2.2. Selecting the Active NTC Material: Nickel Manganate Copper Ceramics $\mathrm{Mn_{2.2}Ni_{0.5}Cu_{0.3}O_4}$

The most widely used materials for NTC thermistors are nickel manganate based systems that have the general formula $\mathrm{AB_2O_4}$ and have a cubic spinel crystal structure, as described in section 1.4.1, such as Ni-Mn-O, Fe-Ni-Mn-O, Cu-Ni-Mn-O [62], [42]. To reiterate, Mn_3O_4 has a normal spinel structure where oxygen atoms form a cubic close packing structure and Mn cations fill both tetrahedral a-sites and octahedral b-sites. Mn_3O_4 is non-conducting because the valency distribution is: $[Mn^{2+}]^{A-site}\,[Mn^{3+}, Mn^{3+}]^{B-site}\,O_4$. Through the addition of Nickel to this system, Ni^{2+} will replace some Mn^{3+} ions at the B-site, and some Mn^{3+} ions will change to Mn^{4+} to preserve the overall electrical neutrality of the material. The new valency distribution will now be $[Mn^{2+}]^{A-site}\,[Ni_x^{2+}, Mn_x^{4+}, Mn_{1-2x}^{3+}, Mn^{3+}]^{B-site}\,O_4$. This new system is now electrically conductive since Mn^{3+} and Mn^{4+} ions at the B-sites will enable phonon assisted hopping of charge carriers between the octahedral b-sites. Hence the effect of doping with nickel changes the crystal structure and increases the conductivity by increasing the concentration of donor-acceptor pairs of $\mathrm{Mn^{3+}}$ and $\mathrm{Mn^{4+}}$ ions.

Rousset et al. [49] investigated the effect the variation of Ni content had on the overall resistivity of the NTC material of $Mn_{3-x}Ni_xO_4$. The effect was also compared when the NTC material of $Mn_{3-x}Ni_xO_4$ was manufactured using the chemical route (oxalic precursors) or the conventional method used in industry. This is an important comparison because the chemical processing route is indicative of ceramics made in a laboratory while the conventional method is indicative of what is widely used in industry, which usually is limited by many more constraints and often isn't as precise as laboratory developed ceramics. The results are summarised in figure 2.2. It shows that when using $Mn_{3-x}Ni_xO_4$ produced using the chemical method, Ni content of $x = 0.78$ resulted with the lowest resistivity. While when produced using conventional methods a higher minimum resistivity was obtained at a Ni content of $x = 0.6$. However, it greatly differs depending on different authors since almost all the ceramic processing parameters affect the result. Though it is clear that resistivity lower than 1000 Ωcm is unobtainable through optimisation of nickel content in nickel manganites manufactured by the chemical process, and resistivity lower than 2000 Ωcm is unobtainable by production using the conventional process. For lower resistivities doping using an additional element is required, towards this cobalt and/or copper are effective as dopants for lowering the resistivity of nickel manganite NTC materials.

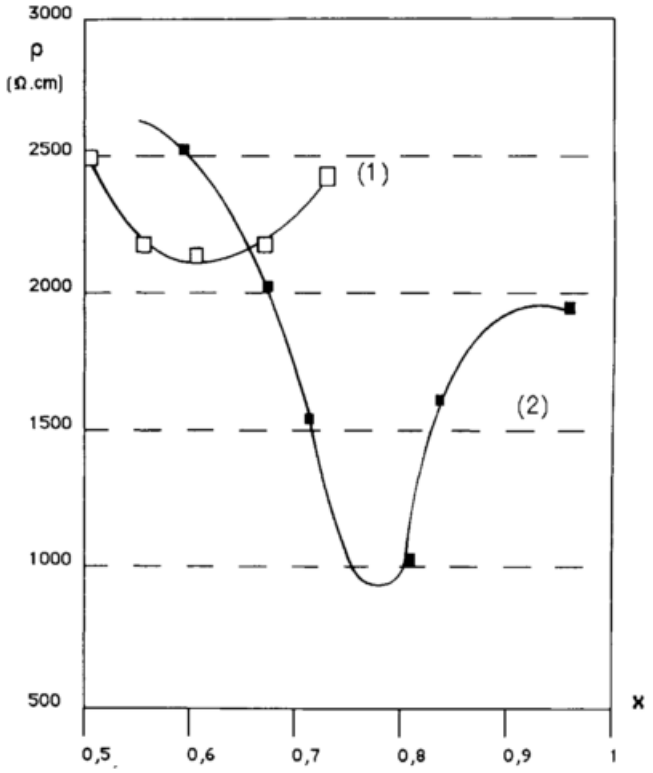

Figure 2.2: Resistivity vs nickel content (x) for $Mn_{3-x}Ni_xO_4$ NTC material where (1) was manufactured using the conventional industrial method and (2) was manufactured using the chemical process (oxalic precursors), taken from [49]

Rousset et al. [49] also investigated the effect of doping nickel manganite with copper or cobalt to see the effect the doping content has on the overall resistivity. The results are presented in figure 2.3 where it can be seen that the nickel content was chosen near the composition for minimum resistivity ($x \approx 0.73$) and the cobalt content was varied from $0 \leq x \leq 1$ for $Mn_{2.25-x}Ni_{0.75}Co_xO_4$ while the copper content was varied from $0 \leq x \leq 0.6$ for $Mn_{2.3-x}Ni_{0.70}Cu_xO_4$. The graph of resistivity versus doping content in figure 2.3 shows that doping with copper content is very effective in reducing the overall resistivity (and can be as low as $\rho \approx 3\ \Omega cm$) and is more effective than doping with cobalt (where ρ can be as low as $\rho \approx 300\ \Omega cm$). Due to the effectiveness of copper at reducing the overall resistivity, a closer look at the effect of copper doping is warranted. But first, if copper doping of nickel manganite is more effective at lowering the resistivity than simply increasing the nickel content in nickel manganites, then at what amount should the nickel content be fixed at?

2.2.1. Selecting the Nickel Content

The interactions of dopants are very complex where even the exact ionic distributions of well used compositions are sometimes disputed, so instead this work will compare two studies that have measured the effect of copper doping using a slightly different amount of Nickel, seen in figure 2.4.

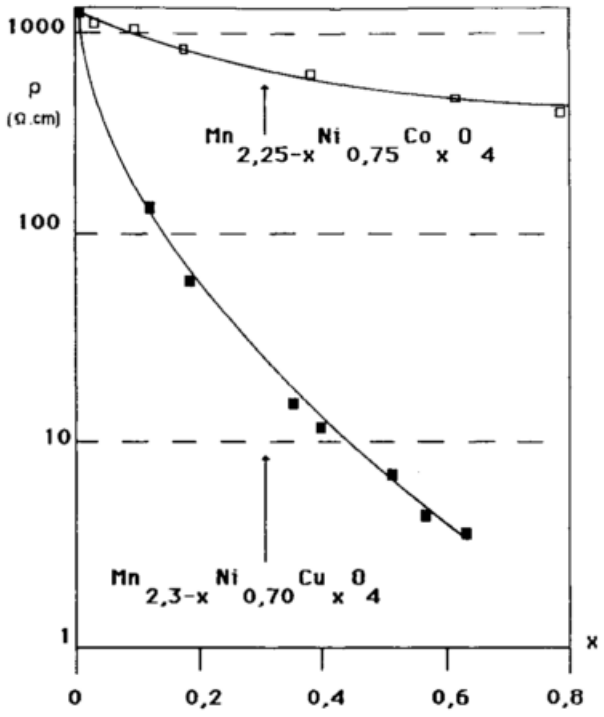

Figure 2.3: Resistivity versus doping content of cobalt in $Mn_{2.25-x}Ni_{0.75}Co_xO_4$ and Cu in $Mn_{2.3-x}Ni_{0.7}Cu_xO_4$, taken from [49]

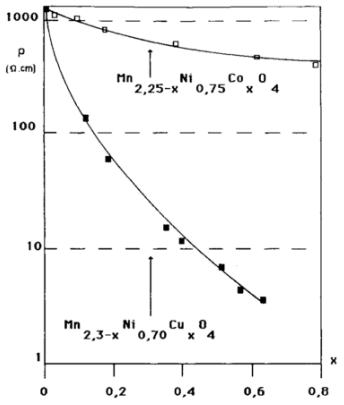

(a) Resistivity vs doping content of Cu in $Mn_{2.3-x}Ni_{0.7}Cu_xO_4$ [49]

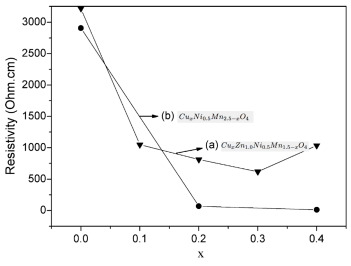

(b) Resistivity vs doping content of Cu in $Mn_{2.5-x}Ni_{0.5}Cu_xO_4$ [62] curve (b)

Figure 2.4: Two studies that have investigated the effect of copper doping on nickel manganite resistivity using different Ni content where (a) [49] used 0.70 and (b) [62] used 0.5

As can be seen from comparing the two similar figures in 2.4, if we compare the resistivity obtained for a copper content of 0.4, the curve in figure 2.4a shows that $Mn_{1.9}Ni_{0.7}Cu_{0.4}O_4$ has a resistivity of $\rho \approx 11$ while the curve in figure 2.4b shows that $Mn_{2.1}Ni_{0.5}Cu_{0.4}O_4$ has a resistivity of $\rho = 12.6$. The resistivities are almost the same for the same amount of copper. Therefore, the extra 0.2 atomic percent of Ni contributes very little to reducing the overall resistivity of the composition when copper is

involved. Moreover, [49] pointed out that an increase of nickel content beyond a certain concentration causes precipitation of NiO since the extra nickel atoms no longer enter the spinel lattice. This creates a polyphase ceramic which can have both advantages and disadvantages. According to [49]; "thermistor polyphase ceramics have better stability than monophase ones", but this improvement of thermal stability comes at the cost of higher resistivity. Furthermore, the NiO precipitates typically arise by having excessively high sintering temperature (e.g. $1300°C$) followed by rapid cooling (e.g. $150°C/h$). This controlled, rapid cooling presents a difficulty for industrial manufacturing of NTC ceramics. Industrial scale tooling, process control and batch and sample sizes can prove to be difficult to accurately control a rapid cooling rate (e.g. large bulk ceramics that cool slower in their centres creating thermal stresses and unstable phases). For this reason a single phase ceramic is desired, so that it is independent of the cooling rate and reproducible on industrial scales. "Single-phase, homogenous, fine-grained ceramics with sufficient density are the most advantageous for practical uses" [9] because they have electrical characteristics that are highly reproducible. The exact threshold at which the added nickel concentration no longer enters the spinel lattice is unclear in [49], but from figure 2.3 it can be inferred that it is at the minimum of the curve of resistivity vs nickel content, since beyond this minimum an increase in nickel content causes an increase in the resistivity. When looking at the appropriate curve ((1) that correlates to nickel manganite prepared using the conventional industrial method), the minimum of resistivity occurs close to a nickel content of 0.6 atomic percentage. A nickel content of 0.5 is then an arguably safe and conservative choice, which agrees well with the results of [62] where a base composition of $Mn_{2.5-x}Ni_{0.5}Cu_xO_4$ was chosen.

This also agrees well with the phase diagram of $Ni_{1-x}Mn_{2+x}O_4$ presented by [31] and illustrated in figure 2.5. The partial phase diagram shows that for $x < 0.5$ for Ni_{1-x}, which is equivalent to a high nickel content $x > 0.5$ for Ni_x at high sintering temperatures, two phase (NiO + Spinel) will occur. Conversely, according to [31], for compositions of low nickel content where $x = 0.60 - 0.85$ for Ni_{1-x} (so if nickel content Ni_x $x = 0.15 - 0.4$) prepared at $1200°C$ or above, it was difficult to obtain well-crystalized material which was possibly due to the occurrence of a two phase region at lower temperatures. In addition, for low nickel content where $x > 0.5$ for Ni_{1-x}, if the sample was cooled too slowly when quenched, the samples were oxidised by the air and Mn_2O_3 would appear as suggested by the x-ray powder diffraction tests performed by [31]. It is important to note that according to [31] the phase boundaries presented in figure 2.5 are approximate boundaries. Therefore, the phase diagram indicates that low ($x > 0.5$ for Ni_{1-x}) and high ($x < 0.5$ for Ni_{1-x}) nickel content can both cause two phases to occur and so a nickel content of x=0.5 is the safest choice if a well-crystalized, mono-phase, cubic spinel phase is desired.

2.2.2. Selecting the Copper Content

Now knowing a target composition of $Mn_{2.5-x}Ni_{0.5}Cu_xO_4$ is desired, how much copper should be used? Firstly, some insight into copper doping is provided by a study of [62] who referenced Elbadraoui et al. [15] who proposed a cationic distribution for copper nickel-manganite of composition $Cu_{0.41}Ni_{0.66}Mn_{2.93}O_4$ of:

$$[Mn^{2+}_{0.616}, Cu^{2+}_{0.360}, Cu^{+}_{0.024}]^{A-site}\,[Ni^{2+}_{0.660}, Mn^{3+}_{0.604}, Mn^{4+}_{0.710}, Cu^{2+}_{0.026}]^{B-site}\,{O_4}^{2-}$$

Evident from the cationic distribution is the contribution copper has to the conduction mechanism because the Cu^{2+} and Cu^{+} in the A-site (tetrahedral sites) also contributes to the electron conduction process. The copper ions follow the same rules, proposed in section 1.4.2, that applies to the main conduction mechanism of electron hopping from Mn^{3+} to Mn^{4+}. The copper ions are cations of the same element, but of different valency, that vary by only one valency, that occupy crystallographically equivalent lattice sites. Hence, one reason why copper doping of nickel-manganite spinel crystals is so effective at reducing electrical resistivity is the Cu^{2+} and Cu^{+} ions that occupy tetrahedral sites that allow electron hopping [15]. Another reason is proposed by Muralidharan et al. [42] who proposed that increasing copper content increases the Mn^{3+}/Mn^{4+} pairs in the B-sites (octahedral sites), being the main conductivity mechanism for nickel-manganite spinels. Bodak et al. [9] claim that Cu^{2+} ions that occupy the B-sites (octahedral sites) are also involved in the conduction mechanism with Mn cations. Again the exact cationic distributions (and their conductivity mechanisms) are somewhat disputed in literature depending on the exact dopants used and their quantities, so it is important to look at em-

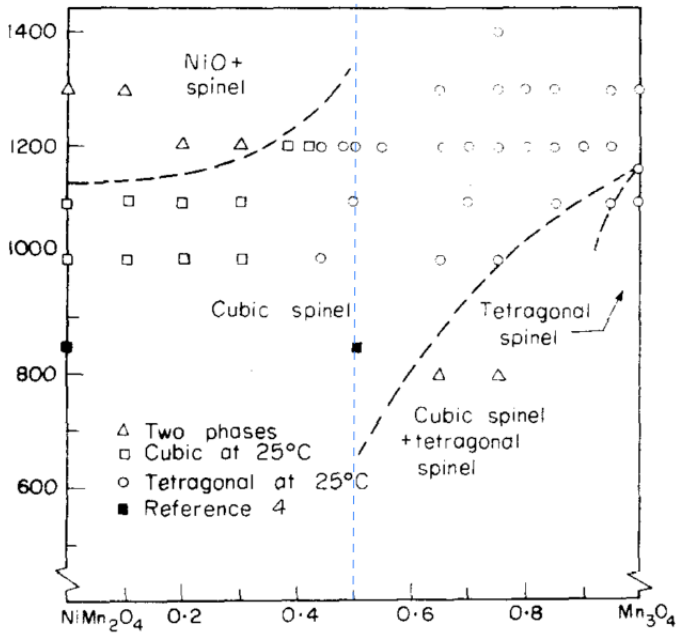

Figure 2.5: Partial phase diagram of $\mathrm{Ni_{1-x}Mn_{2+x}O_4}$ where samples were quenched from the temperatures displayed on the y-axis, taken from [31]

pirical data on the effect of copper doping on electrical performance characteristics. Zhao et al. [62] have measured the effect of copper doping on nickel-manganite's resistivity, B-value and resistivity drift, and is presented in figure 2.6. In addition to looking at the effect of differing copper amounts in $\mathrm{Cu_xNi_{0.5}Mn_{2.5-x}O_4}$, Zhao et al. also looked at at the effect of increasing copper in nickel manganite that also contains zinc $\mathrm{Cu_xZn_{1.0}Ni_{0.5}Mn_{1.5-x}O_4}$.

From observing the 3 subfigures in figure 2.6, it appears that copper is effective in reducing the resistivity, but it comes at the cost of a lower sensitivity (i.e. lower B-value). This trade-off between a desired lower resistivity and undesirable, lower sensitivity is also noted for copper doping in [42]. Another factor that is traded-off with increasing copper content is the lowering of the thermal stability (i.e. higher resistivity drift). The time stability under thermal stress of a NTC thermistor is typically measured by the relative change in resistance $\Delta R/R$ (also referred to as drift) after being exposed to $150°C$ for 1000 hours. According to [49], Mn-Ni-Cu systems show some of the largest drifts that can exceed 20% due to the copper ions since Mn-Cu systems can show drifts of over 100%. This is obviously unfavourable for NTC thermistors as it affects the device's reliability to sense/measure temperature accurately over time. However, as previously mentioned, having a low resistivity will be prioritised and the adverse effects can later be mitigated and optimised with further doping, after a baseline ceramic-polymer composite thermistor has been developed. Keeping this in mind, looking at figure 2.6a of the curve of resistivity vs copper content for $\mathrm{Cu_xNi_{0.5}Mn_{2.5-x}O_4}$. If a low resistivity is desired, the copper content $x \geq 0.2$, but also $x \leq 0.4$ because no further significant reduction in resistivity is achieved with a further increase in copper content. A choice of $x = 0.3$ is a safe pick for copper content so it isn't too close to the threshold where a slight decrease in copper content from processing errors could cause a huge increase in resistivity. Unfortunately the graph of $\mathrm{Cu_xNi_{0.5}Mn_{2.5-x}O_4}$ only tests $x = 0.2$ and $x = 0.4$ and there could be a local minimum, but the graph of $\mathrm{Cu_xZn_{1.0}Ni_{0.5}Mn_{2.5-x}O_4}$ in the same figure suggests the local minimum is at a copper content of $x = 0.3$. This should also hold true for $\mathrm{Cu_xNi_{0.5}Mn_{2.5-x}O_4}$ since the role of zinc in nickel manganites is mainly to improve the stability against oxidation [62] at the expense of higher resistivity. Therefore a copper content of $x = 0.3$ will be chosen, to potentially give minimum resistivity which can be expected to be on the order of $\rho_{25} \approx 12.6$ Ωcm at $25°C$. Using figure 2.6b, the B-value of this system should be on the order of $B_{25/50} \approx 2960$ K. Similarly, using figure 2.6c, the resistivity drift should be on the order of $\Delta R/R \approx 12\%$ after 1000 hours at $150°C$.

This agrees quite well with a study performed by Gao et al. [18] where a very similar composition of copper nickel-manganite $Cu_{0.3}Ni_{0.66}Mn_{2.04}O_4$ was prepared and its electrical properties were measured. A resistivity of ρ_{25} = 63.3 Ωcm was obtained, a $B_{25/50}$ = 2740 K, and a resistivity drift of 5.4% after 500h at $150°C$. It is important to note that this composition has a higher nickel content and all the ceramic processing parameters involved in manufacturing affect the performance results. To reiterate, this is again why this thesis work will aim to use only 3 elements (at least in the initial phase) to simplify the manufacturing process, to limit the risk of irregularities, and to ensure the reproducibility of the results. Hence, this thesis work will commence with using a composition of $Cu_{0.3}Ni_{0.5}Mn_{2.2}O_4$ as the active NTC materials in a ceramic-polymer composite.

If problems arise and the performance is determined to be unacceptable or lower than required, it is important to know the role that dopants can play in improving specific characteristics (e.g. Ni, Ba, Zn, Co). As perviously mentioned, polyphase ceramics have better stability then monophase ceramics [49]. So if thermal stability is a problem, one can induce more phases to precipitate by altering the composition and the sintering and cooling treatments. A higher nickel content would be needed and higher sintering temperature (e.g. $1300°C$) with a fast cooling rate (e.g. $150°C/h$).This can cause NiO phases to precipitate which according to [49] can reduce drift by a factor of 2, at the expense of a higher resistivity. Alternatively, by doping with Ba^{2+} and quenching, precipitates of $BaMnO_3$, NiO, and $CuMnO_2$ can form, reducing the drift to $1-2\%$ at the expense of increasing resistivity. According to [62], the addition of zinc in nickel manganites can improve stability and limit the reduction in sensitivity (i.e. B-value) that a high content of copper causes, again at the expense of a higher resistivity. According to Muralidharan et al. [42], doping nickel manganite with cobalt also decreases the resistivity and B-value with increasing cobalt content, thus having a similar effect as copper doping. However, if you co-dope with cobalt and very small amounts of copper then low resistivities (although not lower than when doped with only copper) can be achieved with good sensitivities. A common theme is that there is always a trade-off with every dopant and is why a baseline composition was chosen that prioritised low resistivity. If certain characteristics need improvement through doping, a collection of different relevant compositions of NTC ceramics found in literature are compiled in table B.1 in appendix B for future reference.

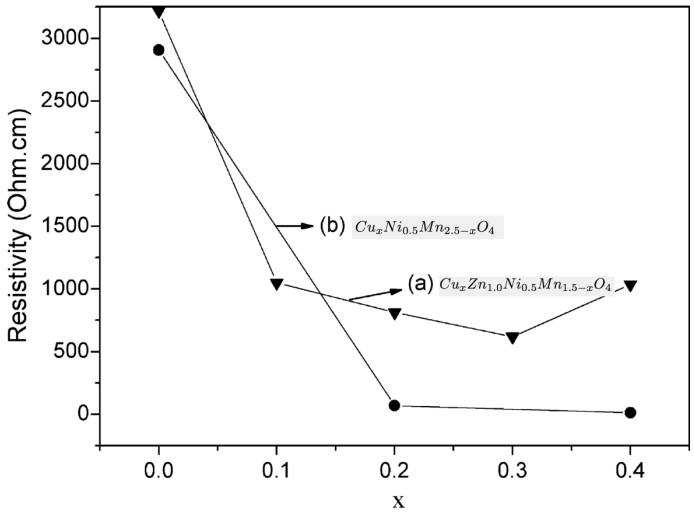

(a) Resistivity vs doping content of Cu in $Mn_{2.5-x}Ni_{0.5}Cu_xO_4$ [62]

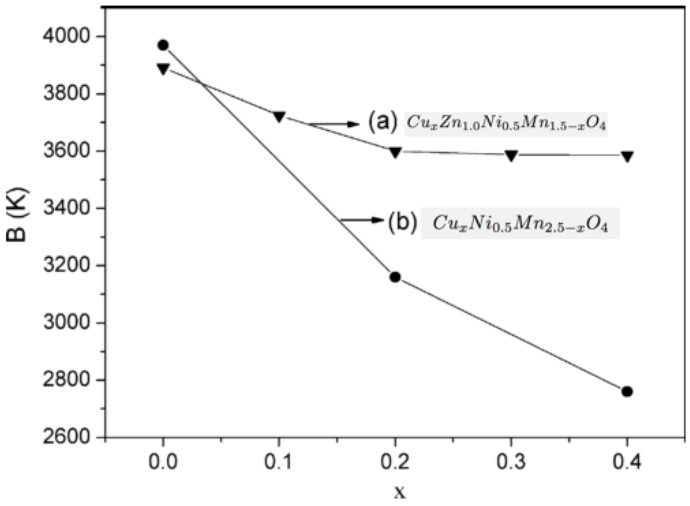

(b) B-value vs doping content of Cu in $Mn_{2.5-x}Ni_{0.5}Cu_xO_4$ [62]

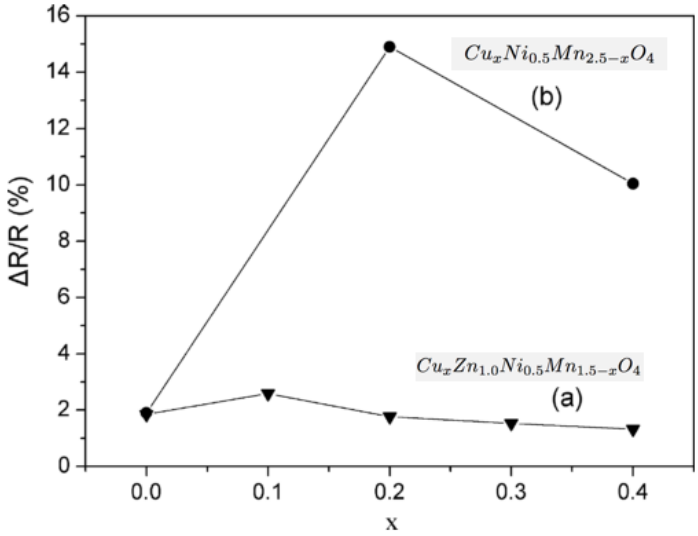

(c) Resistivity drift vs doping content of Cu in $Mn_{2.5-x}Ni_{0.5}Cu_xO_4$ [62]

Figure 2.6: The effect of copper doping on nickel manganite resistivity, B-value, and resistivity drift [62]

3

Phase 2: Characterisation of Ceramic Bulk Properties

3.1. Introduction

As discussed in the previous chapter, NTC ceramic compositions with their exact processing conditions are of high commercial value and are therefore trade secrets. So after selection of a NTC composition described in Chapter 2, bulk ceramic pellets were processed to determine the best processing conditions and techniques to see and characterise their thermistor performance. Ceramic pellets were produced with the intention to carry-over the same processing conditions (e.g. sintering time and temperature) to produce ceramic fibres for flexible composites.

3.2. Conventional Manufacturing Route of NTC Ceramics

Although thermistors come in many different shapes, sizes, and base materials, they all have a relatively similar production process that follows the stages illustrated in figure 3.1. With the exception of film thermistors, most thermistor manufacturers follow this general production scheme with some variations.

In stage 1, metal oxides that form the basis of the NTC thermistor are selected and weighed to the appropriate ratios needed for the final composition. These materials are usually divalent metals that form AO oxides (e.g. FeO, CuO, NiO, CoO) and trivalent metals that form B_2O_3 oxides (e.g. Fe_2O_3, Mn_2O_3) as already discussed in section 1.4.1.

1. Weighing Component Materials
↓
2. Powdering Mixing/Milling
↓
3. Calcination
↓
4. 2nd Milling
↓
5. Formation of Green Bodies
↓
6. Sintering
↓
7.Finishing

Figure 3.1: General Process Procedure for Thermistor Manufacture

In stage 2, mixing and milling is usually performed where milling is needed to reduce the particle size and to eliminate aggregates that have formed. These aggregates would otherwise need lots of time during the sintering process for the neighbouring particles to inter-diffuse. Breaking them up, homogenizing them, and mixing them in this stage helps the constituents react faster and more completely in the following stage to produce a more uniform final composition.

In the calcination stage, the powder constituents that have been physically mixed together are chemically reacted (by solid state reaction) at high temperature to form the desired compound. Significant shrinkage will occur during calcination, which is advantageous to have the most shrinkage occur in this stage before the final shaping of the material has been performed (i.e. to avoid crack formation). The temperature and time of calcination needs careful consideration and control since it influences the particle size of the calcined product and the amount of shrinkage.

Stage 4 involves milling again since the calcined product may have formed aggregates which are undesirable for the following shaping stage, but to also reactivate any unreacted materials. This stage may consists of a series of milling operations in order to arrive at the desired controlled particle size.

Stage 5 is the shaping stage where the desired form is given (e.g. disc, rod, beads, etc) before the sintering process is performed. A binder (and frequently solvents, plasticisers, and surfactants) is usually added to the mix (normally already in the milling stage) to make the formation of green bodies easier. The binder's role is to give the dry shape enough strength to be handled for shaping and sintering. It is also extremely important that the binder can be removed (e.g. burnt-out) from the mix without having a disruptive effect. The powder mix is usually thoroughly mixed with a solution containing the binder (e.g. polyvinyl alcohol, acetate, methacrylate, phthalates, methyl celluloses, starch, etc.) and then subsequently dried and then shaped. The shaping then depends on the desired form, e.g. rod shapes are extruded through a die and cut into the desired length while discs and washers are pressed into shape by a tabulating press. The binder and the particle size then have to be controlled and adjusted to the shaping method to ensure good formability and avoid cracking and void formation in the green bodies. Some of the shaping methods that can be used are [41]:

- Dry-pressing
- Isostatic pressing
- Calendering viscous plastic processing
- Extrusion
- Jiggering
- Injection Moulding
- Slip-casting
- Band-casting
- Screen-printing

Stage 6 is Sintering where densification occurs to form a single phase of polycrystalline semiconducting ceramic. The temperature/time profile needs careful design since many factors needs consideration that affect the final product. The heating rate needs to be controlled so that the burn out of the binder doesn't cause crack or void formation, warping, bloating, or particle rearrangements. The soak temperature needs to account for grain growth and shrinkage, and the cool-down rate needs to avoid introducing thermal shock stresses than can create residual stresses and even cracks. A typical sintering cycle can take 8-24 hours, with a soak temperature of around $1200^{\circ}C$ held at $1-12$ hours.

The remaining stages are related to the 'finishing' of the ceramic to create an electronic device. Slicing would be performed if smaller sizes or shapes are needed from the bulk material. Metallisation is then performed to create electrical contact areas on the surface of the ceramic from which leads can be attached. The choice of metal is important as adhesion to the ceramic is important, as well as to avoid introducing unwanted barriers to the flow of current carriers. After metallisation soldering leads would be attached so that the thermistor can be incorporated into a circuit. Encapsulation or lacquering

is then performed to provide shielding from the environment (e.g against moisture and oxidation) and to control the electrical properties of the device. However, this step and the entire finishing stage is highly dependent on the final desired thermistor design, shape, and target properties and the whole process is adapted accordingly, but generalised in this description.

3.3. Manufacturing Route for Bulk Pellets of $Mn_{2.2}Cu_{0.3}Ni_{0.5}O_4$

To produce pellets of $Mn_{2.2}Cu_{0.3}Ni_{0.5}O_4$, the conventional manufacturing route will be followed with some minor adjustments. The correct ratio of powder constituents of the metal oxide powders of Mn_2O_3, NiO, and CuO (obtained from Sigma-Aldrich) were measured using a balance scale. The un-calcinated powder was then mixed and milled using a planetary ball mill (Retsch, PM100, Haan, Germany) for 1 hour 30 minutes at 150 rpm using a container filled with 5.20 mm Y-stabilised zirconium oxide (ZrO) balls. For better milling performance, the container was filled up to $\frac{2}{3}$ with cyclohexane. After milling, the powder is poured through a sieve to collect the ZrO balls, and left in a pan for the cyclohexane to evaporate and the powder to dry. The powder is then collected into a Y-stabilised zirconium oxide crucible and calcined at $800°C$ for 6 hours in a furnace (Nabetherm L5/13/B180, Lilienthal/Bremen, Germany), with a heating rate of $300°C/hr$. After calcination, the powder aggregates are stuck together and are re-milled again using the planetary ball mill for 1 hour and 30 minutes. The calcined powder mixture is then dried again in a pan and placed in a oven at $100°C$ for 1 hour to ensure it is thoroughly dry. The dried powder is then stored in vacuum to avoid moisture absorption.

Pellets are subsequently made using the calcined powder to primarily investigate the effects of sintering time and temperature (among other factors) on the densification of the powder and its corresponding electrical properties. Towards this, the calcined powder is pressed into pellets of 20 mm diameter using 1.5 grams of powder and 3 tonnes of pressure, held for 1 minute before being released. The pellets are then placed onto a Y-stabilised ZrO plate with a thin layer of loose calcined powder to prevent sticking when sintered in a furnace. The pellets are then placed in a furnace to sinter under different sintering schemes (e.g. $1100°C$ for 6 hours with a $300°C/hr$ heating rate). After the pellets are sintered, the top layer of the pellets need to be polished to remove the thin oxide layer that has developed. This is performed gently by hand using carbon sanding paper with 1000 grit and ethanol for lubrication. To measure the electrical performance of the sintered pellets, both surfaces of the circular pellets need electrodes, applied using a gold sputter coater (Balzers SCD 040, Lichtenstein) using an electrical current of 15 mA for 15 minutes on each side. The finished electrodes are tested using a multimeter (Fluke 114) to check for conductivity.

3.4. Characterisation

To make sure that the right phase was obtained, X-ray diffraction (XRD) using Cu $K\alpha$ radiation (Rigaku MiniFlex600) is performed on the calcined powder and compared with indexed results of similar compositions that are stored in the database of PDXL2 (Rigaku's full-function powder diffraction analysis package). The crystal structure of the pellets after sintering was determined using XRD to verify the composition, and to determine the lattice parameters to help calculate the maximum theoretical density. The maximum theoretical density is needed to later calculate the relative density of the pellets. The density of the sintered pellets was measured using Archimedes' principle. A scanning electron microscope (SEM) (JEOL, JSM-7500F, Nieuw Vennep, The Netherlands) is used to observe the particle size of the ceramic powder and the microstructure of the sintered ceramic (e.g. particle size, porosity, defects). Observing microstructure and defects was also performed using an optical microscope (Zeiss, Discovery V8, Germany and Keyence, VHX 2000, Osaka, Japan). Pellet weight and dimensions were measured using a regular balance scale and calliper.

3.4.1. Characterisation of Electrical Performance - Experimental Setup

DC Resistance measurements were performed using a Keithley Model 2000 Multimeter, where the Model 2000 can make 4-wire resistance measurements from $100\mu\Omega$ to $120M\Omega$. The kelvin (4-wire) resistance measurement is a method to avoid errors from wire resistance and measures only the subject resistance. How this is achieved is schematically shown in figure 3.2. The subject resistance is obtained by measuring the current that passes through the subject, the voltage drop across, and by using Ohms Law ($R = \frac{V}{I}$). The trick is that a very small current runs through the voltmeter's wires so the drop

in voltage due to long wires is insignificant compared to the voltage drop of the subject resistance. By decoupling the ammeter, the voltmeter will not measure any voltage drop across the ammeter's wires, which carry the main current.

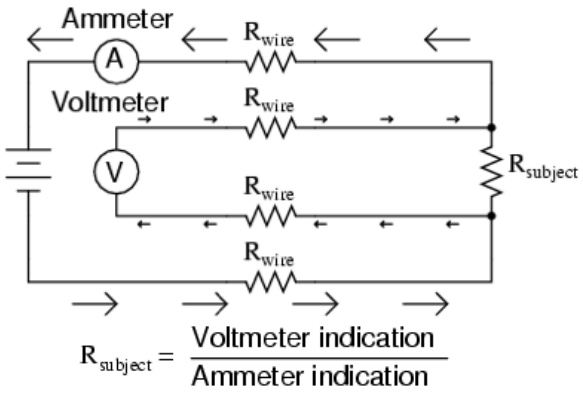

Figure 3.2: Schematic of Kelvin (4-Wire) Resistance Measurements, ammeter and voltmeter are decoupled with low current passing through voltmeter and high current through ammeter, [27]

Resistance measurements were performed at constant temperature, 25 or $30°C$ and $85°C$, by submerging the ceramic pellets into an oil bath (Lauda K20) of sunflower oil that accurately holds the temperature constant to $0.1°C$ accuracy. The electroded pellets were held using a custom device, shown in figure 3.3a, to both submerge the pellet into the oil and electrically connect both sides to the Keithley 2000 multimeter. The complete experimental setup for the resistance measurements is pictured in figure 3.3b. The B-value can then be calculated using equation 1.11 and the temperature coefficient of resistance using equation 1.12. Resistivity at a particular temperature (e.g. ρ_{25} or ρ_{85}) can be simply calculated using equation 3.1.

$$\rho = \frac{R \cdot A}{L} [\Omega \cdot cm] \tag{3.1}$$

Where,

- R is the resistance in Ohms.
- A is the cross sectional area (area of the electrode) in cm^2.
- L is the length (thickness of the pellet disk) in cm.

3.4.2. Validation of Experimental Setup

The experimental setup needs to be validated to ensure that future resistivity results are reliable. Towards this, 3 reference samples of slightly different compositions of NTC ceramic pellets were obtained from Prof. dr. ir. Pim Groen's personal archive. The reference samples are of the following composition:

- $Mn_{2.4}\,Ni_{0.6}\,O_4$
- $Mn_{2.35}\,Ni_{0.6}\,Cu_{0.05}\,O_4$
- $Mn_{2.3}\,Ni_{0.6}\,Cu_{0.1}\,O_4$

Their resistance was measured at $25°C$ and $85°C$ and their corresponding resistivity and B-value were calculated and plotted against their known values (from Pim Groen, Internal Communications) shown in figure 3.4.

As can be seen from figure 3.4, the experimentally measured values are close to the reference values of resistivity and B-value. There is some variation, but considering the NTC pellets were manufactured in 2001, it is suspected that the variation is due to ageing and moisture absorption of the

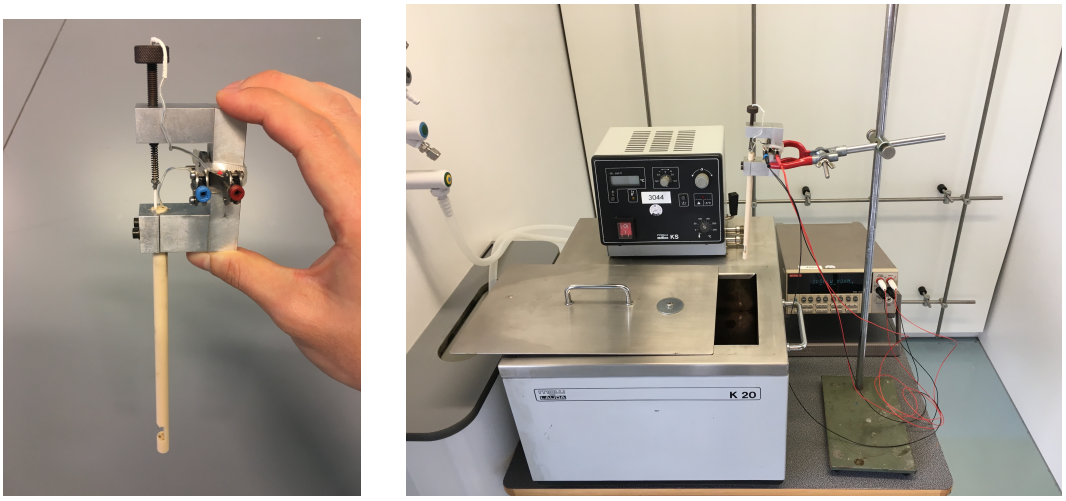

(a) Custom device for submerging pellets

(b) Complete Experimental Setup

Figure 3.3: Experimental Setup for Measuring NTC Electrical Performance

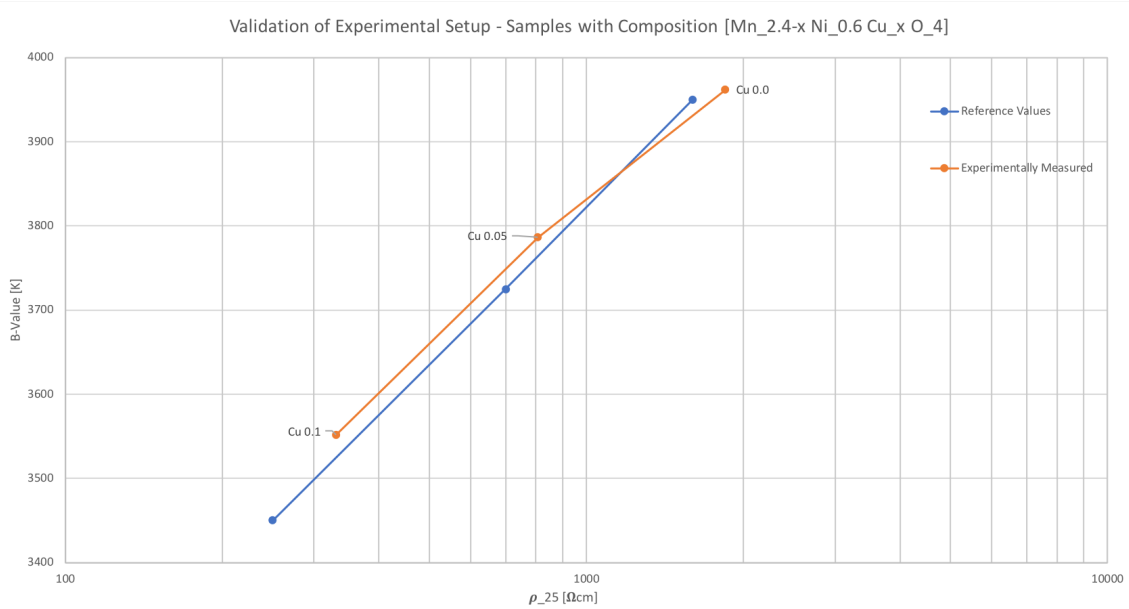

Figure 3.4: Comparison of reference values and experimentally measured resistivity and B-value for experimental validation

pellets. This then explains why the experimentally obtained resistivity is systematically higher then their corresponding reference values. Therefore, due to the similar values obtained between the experimentally measured resistance readings and the reference values, the experimental setup has been validated.

3.5. Results of Processing Conditions

From Chapter 2, the NTC ceramic composition chosen was $\mathrm{Mn_{2.2}Cu_{0.3}Ni_{0.5}O_4}$ where one can expect to obtain thermistor performance values similar to those reported in literature. I.e. a $\rho_{25} \approx 12.6\ \Omega cm$, a $B_{25/50} \approx 2960$ K, and a resistivity drift on the order of $\Delta R/R \approx 12\%$ after 1000 hours at $150°C$ [62]. But as previously noted, all processing conditions have an effect on the overall final performance of the NTC ceramic. Therefore, this section investigates the following processing factors affecting the

ceramic bulk properties:

1. Sintering time (6 vs 2.5 hours)
2. Pellet size (20 vs 7 mm)
3. Copper content (Cu 0.3, Cu 0.1, Cu 0.05)
4. Sintering temperature and ramp ($1100°C$ vs $1200°C$)
5. Effect of adding binder (no binder vs binder)
6. Sintering temperature revisited ($1200°C$ vs $1250°C$ with binder)

This list is not exhaustive, but given the time constraints of the thesis, each relevant processing factor was sequentially investigated in the manufacturing route. To start, the composition of $Mn_{2.2}Cu_{0.3}Ni_{0.5}O_4$ was used and pressed into pellets of 20 mm diameter using the same mass of calcined powder (1.5 g). The pellet pressing technique was always kept constant going to a maximum pressure of 3 tons and holding for exactly 1 minute, before releasing the pressure and removing the pellets. A sintering temperature of $1100°C$ was chosen with a sintering ramp of $300°C/hr$. The first processing condition to be investigated was then the sintering time.

3.5.1. Sintering Time

To summarise, the processing parameters that are kept the same are listed in table 3.1 of constant variables. The sintering time was varied from a long 6 hours to a shorter and more convenient 2.5 hours. It should be noted that the values presented in 3.2 are an average of 5 specimens and the standard deviation (SD) is included.

Table 3.1: Constant Variables - Processing Parameters

Constant Variables	
Composition	Mn(2.2) Ni(0.5) Cu(0.3) O(4)
Pellet Diameter	20 mm
Sintering Temperature	1100 °C
Sintering Ramp	300 °/hr

Table 3.2: Effect of sintering time on thermistor performance of NTC ceramic pellets

Sintering Time [hrs]	Density [g / mL]	Relative Density [%]	ρ_{30} [Ω·cm]	ρ_{85} [Ω·cm]	$B_{30/85}$ [K]	α_{30} [% / K]
6	4.92 (SD 0.02)	93.6 (SD 0.4)	450 (SD 320)	180 (SD 40)	1490 (SD 1300)	-1.6 (SD 1.4)
2.5	4.84 (SD 0.03)	92.1 (SD 0.5)	310 (SD 120)	180 (SD 80)	1160 (SD 630)	-1.3 (SD 0.7)

As can be seen from the thermistor performance values in table 3.2, there is some difference in the resistivity at $30°C$ which translates to a difference in the B-value. But more importantly, the pellets exposed to 6 hours of $1100°C$ showed a high amount of disk warpage and cracking. Any cracks and defects were exacerbated by the long sintering treatment which led them to break very easily after being handled, as can be seen in figure 3.5. The difference in colour of the gold electrode is due to a height difference, caused by warpage. This is what also causes a larger spread in resistivity values and why the standard deviation is very large for the B-value obtained. In conclusion, sintering for a shorter time (2.5 hours) achieves good thermistor performance, while avoiding cracking and disk warpage and is cheaper and quicker to manufacture.

3.5.2. Pellet Size

The achievable density and performance of the NTC ceramic proved to be very sensitive to the pellet pressing technique. For this reason, making pellets of smaller diameter size could help in producing pellets with less defects and cracking. Hence, pellets of 7 mm diameter were made and compared to the pellets of 20 mm diameter. Again the constant variables are summarised in table 3.3 and the

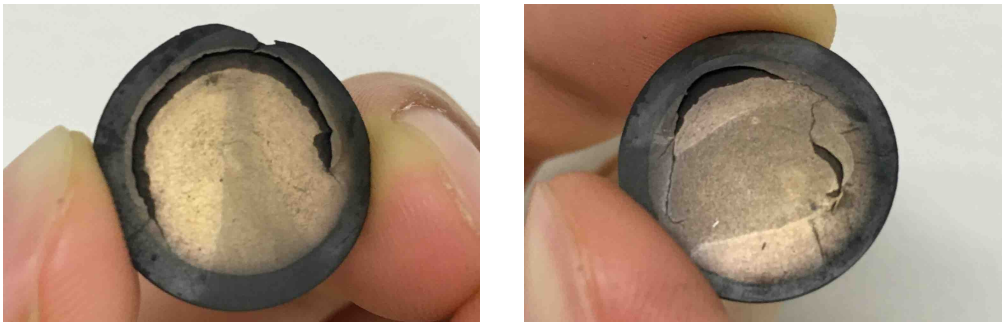

(a) (b)

Figure 3.5: Pellets sintered at $1100^{\circ}C$ for 6 hours were more likely to crack and warp

Table 3.3: Constant Variables - Processing Parameters

Constant Variables	
Composition	Mn(2.2) Ni(0.5) Cu(0.3) O(4)
Sintering Temperature	1100 °C
Sintering Ramp	300 °/hr
Sintering Time	2.5 hrs

Table 3.4: Effect of pellet size on thermistor performance of NTC ceramic pellets

Pellet Size [mm]	Density [g / mL]	Relative Density [%]	ρ_{30} [Ω·cm]	ρ_{85} [Ω·cm]	$B_{30/85}$ [K]	α_{30} [% / K]
20	4.84 (SD 0.03)	92.1 (SD 0.5)	310 (SD 120)	180 (SD 80)	1160 (SD 630)	-1.3 (SD 0.7)
7	4.93 (SD 0.01)	93.9 (SD 0.1)	230 (SD 95)	70 (SD 25)	2610 (SD 135)	-2.8 (SD 0.1)

results are an average of 5 specimens, presented in table 3.4.

As can be seen from the performance characteristics presented in table 3.4, smaller pellets have higher density, lower resistivity at both $30^{\circ}C$ and $85^{\circ}C$, while having a larger B-value and temperature coefficient of resistance. The pressing technique is a very sensitive processing factor and smaller pellets are easier to press to produce consistent pellets with less cracks and defects, and thus they are able to achieve higher density, and consequently better thermistor performance.

3.5.3. Copper Content

The pellets of $Mn_{2.2}Ni_{0.5}Cu_{0.3}O_4$ were achieving high relative densities (above 92%), and their resistivity at room temperature was quite low, but their B-value was also low (B-value < 3000 K). Note in section 1.7, the thesis objective was to ultimately create flexible thermistors with a B-value > 3000K. Hence, it was necessary to look to reduce the copper content of the material composition to raise the sensitivity (B-value and α) at the cost of higher resistivity. Hence, new pellets of composition $Mn_{2.4}Ni_{0.5}Cu_{0.1}O_4$ and $Mn_{2.45}Ni_{0.5}Cu_{0.05}O_4$ were produced and compared to the original $Mn_{2.2}Ni_{0.5}Cu_{0.3}O_4$ specimens. The constant variables are summarised in table 3.5 and the results presented in table 3.6.

Table 3.5: Constant Variables - Processing Parameters

Constant Variables	
Pellet Diameter	7 mm
Sintering Temperature	1100 °C
Sintering Ramp	300 °/hr
Sintering Time	2.5 hrs

Table 3.6: Effect of copper content on thermistor performance of NTC ceramic pellets

Composition	Density [g / mL]	Relative Density [%]	ρ_{30} [Ω·cm]	ρ_{85} [Ω·cm]	$B_{30/85}$ [K]	α_{30} [% / K]
Mn(2.2) Ni(0.5) **Cu(0.3)** O(4)	4.93 (SD 0.01)	93.9 (SD 0.1)	230 (SD 95)	70 (SD 25)	2610 (SD 135)	-2.8 (SD 0.1)
Mn(2.4) Ni(0.5) **Cu(0.1)** O(4)	4.81 (SD 0.002)	93.5 (SD 0.05)	4560 (SD 930)	820 (SD 100)	3530 (SD 225)	-3.7 (SD 0.2)
Mn(2.45) Ni(0.5) **Cu(0.05)** O(4)	4.63 (SD 0.03)	90.1 (SD 0.6)	25360 (SD 7500)	4110 (SD 1320)	4030 (SD 60)	-4.2 (SD 0.1)

Evident from table 3.6 is that a higher density is obtainable with a higher copper content in copper nickel manganate ceramics. With higher copper content, the resistivity is lower, but so is the sensitivity (B-value and α). Additionally, the resistance drift (i.e. thermal instability) was observed to be high and plays a larger role at lower resistances. A copper content of 0.1 is evidently a better composition because it delivers a higher B-value and α, close to those delivered by a copper content of 0.05, but with a lower trade-off in increased resistivity. For these advantages, the new NTC thermistor composition selected is $\mathrm{Mn_{2.4}Ni_{0.5}Cu_{0.1}O_4}$.

3.5.4. Sintering Temperature and Ramp

To obtain a higher density and better thermistor performance, a higher sintering temperature can be tested. From literature (Prof. dr. ir. Pim Groen, Internal Communications), similar copper nickel manganate NTC pellets (but of slightly different composition) had promising performance being sintered at $1200°C$ with a ramp of $180°C/hr$. Its exact manufacturing conditions are unknown, but it indicates a higher sintering temperature with slightly slower heating rate may be better for copper nickel manganate pellets. New pellets were therefore sintered at $1200°C$ for 2.5 hours with a ramp of $180°C/hr$ and compared to the original scheme of $1100°C$ for 2.5 hours with a ramp of $300°C/hr$. Again, the constant variables are presented in table 3.7 and the results presented in table 3.8.

Table 3.7: Constant Variables - Processing Parameters

Constant Variables	
Composition	Mn(2.4) Ni(0.5) Cu(0.1) O(4)
Pellet Diameter	7 mm
Pellet Mass	0.25g
Sintering Time	2.5 hrs

Table 3.8: Effect of sintering temperature and ramp on thermistor performance of NTC ceramic pellets

Sintering Temp & Ramp	Density [g / mL]	Relative Density [%]	ρ [Ω·cm]	ρ_{85} [Ω·cm]	B [K]	α [% / K]
Temp = 1100 °C Ramp = 300 °C / hr	4.81 (SD 0.002)	93.5 (SD 0.05)	ρ_{30} = 4560 (SD 930)	820 (SD 100)	$B_{30/85}$ = 3530 (SD 225)	α_{30} =-3.7 (SD 0.2)
Temp = 1200 °C Ramp = 180 °C / hr	4.75 (SD 0.09)	92.4 (SD 1.8)	ρ_{25} = 5370 (SD 2230)	650 (SD 330)	$B_{25/85}$ = 3790 (SD 140)	α_{25} = -4.3 (SD 0.2)

When comparing the results presented in table 3.8, resistivity at $25°C$ is not very comparable to resistivity at $30°C$, but all new samples were measured at $25°C$ to be more comparable to results published in literature. When looking at resistivity at $85°C$, it is evident that a higher sintering temperature produced an average resistivity that was lower. Consequently, the B-value and temperature coefficient of resistance were higher. However, the measured density doesn't seem to agree, having a lower density with higher sintering temperature. This is probably due to a measuring error with the archimedes principle where trapped air bubbles could have introduced measurement errors. This was confirmed by measuring the diameter of the pre and post sintered pellets for both sintering schemes producing a 4.43% shrinkage in pellet diameter for the $1100°C$ sintering scheme, and a 7.04% shrinkage in pellet diameter for the $1200°C$ sintering scheme. This suggests that the pellets exposed to the higher sintering scheme had higher geometrical shrinkage and therefore should have a higher density, corroborating the theory that the measured density was lower due to a measurement error. Hence, the scheme of $1200°C$ for 2.5 hours with a ramp of $180°C/hr$, has been shown to be a better sintering scheme.

3.5.5. Effect of Binder

In preparation for the wet fibre spinning process, where a binder will be used, it is important to see if the addition of binder to bulk ceramic pellets has an effect on the final density and performance of the pellets. In theory, the binder should burn-out at low temperature and should not be detrimental to the final density and performance. However, the spaces left by the binder could be large enough that the sintering time and temperature does not allow for a comparatively high density to be reached. Pellets using binder were produced with the same processing conditions presented in table 3.9 and the results are presented in table 3.10. The binder used was polyethylene glycol with molecular weight $M_w = 20,000$ (PEG, Fluka 81300, Sigma-Adlrich Chemie GMBH, Steinheim, Germany). The ratio used was $50g : 1.5g : 10mL$ of $\mathrm{MnCuNiO}$: PEG : $\mathrm{H_2O}$, where the PEG was dissolved in warm water and then gradually mixed with the MnNiCuO calcined powder and then pressed into pellets.

Table 3.9: Constant Variables - Processing Parameters

Constant Variables	
Composition	Mn(2.4) Ni(0.5) Cu(0.1) O(4)
Pellet Diameter	7 mm
Pellet Mass	0.25 g
Sintering Temperature	1200 °C
Sintering Ramp	180 °/hr
Sintering Time	2.5 hrs

Table 3.10: Effect of adding binder (polyethylene glycol) on thermistor performance of NTC ceramic pellets

Binder	Density [g / mL]	Relative Density [%]	ρ_{25} [Ω·cm]	ρ_{85} [Ω·cm]	$B_{25/85}$ [K]	α_{25} [% / K]
Without	4.75 (SD 0.09)	92.4 (SD 1.8)	5370 (SD 2230)	650 (SD 330)	3790 (SD 140)	-4.3 (SD 0.2)
With	4.81 (SD 0.03)	93.6 (SD 0.6)	690 (SD 33)	90 (SD 1)	3650 (SD 64)	-4.1 (SD 0.1)

What was evident from the manufacturing of the pellets is that the addition of binder helped with the processability of the calcined ceramic powder and helped to produce more consistent pellets with less defects, chipping, and cracks. The binder also helped the unsintered pellets keep shape and were less fragile making them easier to handle prior to sintering. This is probably why the resistivity at both $25°C$ and $85°C$ was drastically lower when a binding agent was used. Surprisingly, the addition of binder helped produce pellets with higher density, but the improvement in drastically lowering resistivity cannot be attributed to just the increase in density. It is probably due to the binder helping to avoid crack and void formation within the pellet. It was observed that pellets without binder had a characteristic crack around the circumference, midway through the thickness of the disk, this also caused the pellets to crack into two halves if mishandled. Hence, the addition of binder helped improve the achievable density and avoid crack and defect formation leading to drastically lower resistivity, while keeping sensitivity (B-value and α) high.

To confirm that a monophase ceramic was still obtained, XRD was performed to make sure there was no unexpected peaks. The XRD results are presented in figure 3.6 where the pattern is compared to a reference pattern from the PDXL2 archive of the closest composition available: $\mathrm{Mn_{2.17}\,Ni_{0.7}\,Cu_{0.13}\,O_4}$. The peaks match very well and there are no unexpected or extra peaks, leading to the conclusion that a monophase exists of the spinel structure. To confirm that all the binder has been burn-out, leaving no residual components, SEM images were taken to compare the microstructure of sintered pellets that used binder versus pellets that did not. Presented in figure 3.7 is a comparison of the microstructure inside the pellets, it is evident that they are very similar, confirming that the use of a binder doesn't have a detrimental effect on the microstructure.

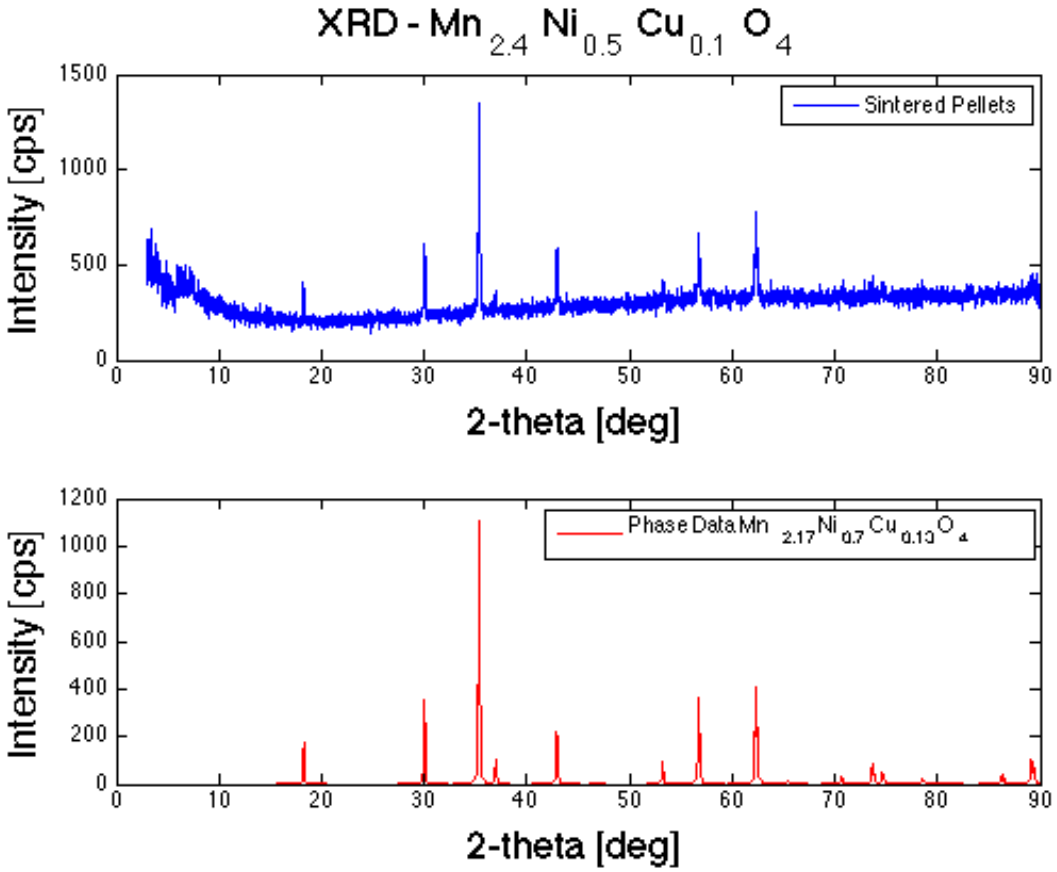

Figure 3.6: XRD pattern of sintered $Mn_{2.4}\,Ni_{0.5}\,Cu_{0.1}\,O_4$ pellets that used binder compared to reference pattern of $Mn_{2.17}\,Ni_{0.7}\,Cu_{0.13}\,O_4$

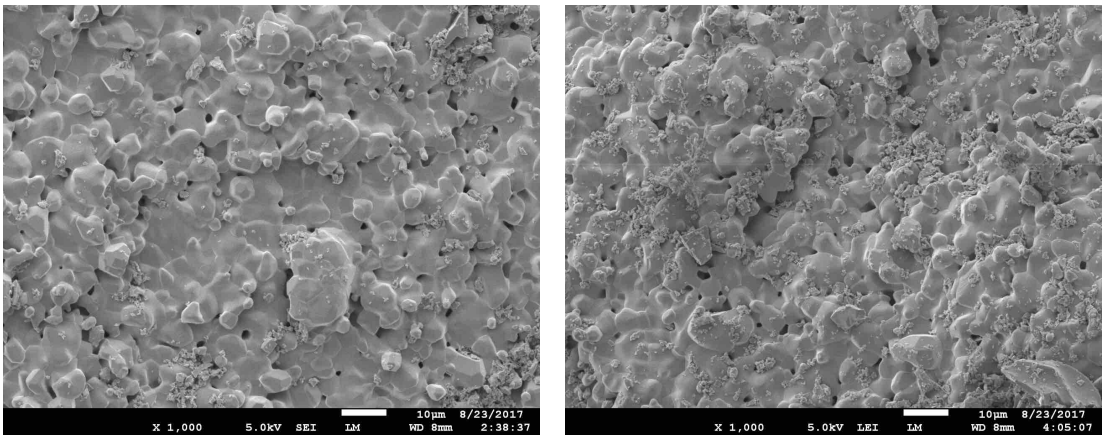

(a) No Binder Used (b) Binder Used

Figure 3.7: Comparison of SEM images of microstructure inside sintered pellets of $Mn_{2.4}\,Ni_{0.5}\,Cu_{0.1}\,O_4$ at same magnification

3.5.6. Sintering Temperature Revisited (with binder)

With the addition of a binder that gets burnt out at low temperatures during the sintering scheme, the ceramic particles need to diffuse over a greater distance to form a compact, dense ceramic. However, the effect of the binder was shown to slightly help the final density of the ceramic in section 3.5.5. Evidently, the highest obtainable density is most sensitive to the physical pressing and forming tech-

nique, for which the binder greatly helps (producing less defects). It is then interesting to revisit the sintering temperature and see if an even higher sintering temperature will help obtain a slightly higher density. New specimens were made with binder (where the constant variables are presented in table 3.11) and sintered at $1250^{\circ}C$ for 2.5 hours with a ramp of $180^{\circ}C/hr$. This is the maximum temperature that the furnace (Nabetherm L5/13/B180, Lilienthal/Bremen, Germany) can deliver over an extended period of time. The results are compared with the pellets sintered at $1200^{\circ}C$ for 2.5 hours with a ramp of $180^{\circ}C/hr$ and are presented in table 3.12. It must be noted that the pellets were produced with lower mass (0.15 g) since it has been observed that pellets of the same diameter (7mm) but with lower mass leads to less defects and cracks.

Table 3.11: Constant Variables - Processing Parameters

Constant Variables	
Composition	Mn(2.4) Ni(0.5) Cu(0.1) O(4)
Pellet Diameter	7 mm
Pellet Mass	0.15 g
Binder	With Binder
Sintering Ramp	180 °/hr
Sintering Time	2.5 hrs

Table 3.12: Effect of higher sintering temperature on thermistor performance of NTC ceramic pellets with binder

Sintering Temp	Density [g / mL]	Relative Density [%]	ρ_{25} [Ω·cm]	ρ_{85} [Ω·cm]	$B_{25/85}$ [K]	α_{25} [% / K]
1200 °C	4.79 (SD 0.15)	93.1 (SD 3.0)	910 (SD 280)	120 (SD 30)	3600 (SD 40)	-4.1 (SD 0.05)
1250 °C	4.69 (SD 0.10)	91.2 (SD 2.0)	720 (SD 180)	90 (SD 20)	3630 (SD 30)	-4.1 (SD 0.03)

From the results presented in table 3.12, pellets sintered at $1250^{\circ}C$ had slightly lower resistivity and slightly higher sensitivity (B-value and α). However, the density obtained from the archimedes principle shows conflicting results where the higher sintering temperature produced pellets with lower density. It is speculated that this is again a measurement error (probably due to trapped air-bubbles) because the shrinkage in diameter of the pellets after sintering is higher. Pellets sintered at $1250^{\circ}C$ had 8.01% shrinkage in diameter, while pellets sintered at $1200^{\circ}C$ shrunk by 6.43%. This suggests the pellets sintered at $1250^{\circ}C$ had higher geometrical shrinkage and therefore should have a higher density, corroborated by the lower resistivity values. However, when taking the standard deviation of the averaged results into account, the results are not significantly different. Hence, either sintering scheme can practically be used.

3.6. Validating Results

To validate the results of the thermistor performance obtained from our composition and manufacturing process for NTC ceramics, it was necessary to compare to a reference sample of similar composition and processing conditions to validate the results. Towards this, the reference sample of $Mn_{2.3}\,Ni_{0.6}\,Cu_{0.1}\,O_4$ used in section 3.4.2 is used to compare to the results from section 3.5.6. Both used binder and were sintered at $1200^{\circ}C$ with a ramp of $180^{\circ}C/hr$. The thermistor performance can be compared in table 3.13.

Although the nickel content of the reference sample is higher, the composition is very comparable. Notably, the reference sample is very dense at almost 99.5% relative density, which could account for the lower resistivity. The order of magnitude is the same and the B-value and temperature coefficient of resistance α are very similar. Based on the similarity of the results and taking into account the different in relative density, the results obtained from the experimentally manufactured NTC ceramic pellets are very sensible and therefore validated.

Table 3.13: Comparison of thermistor performance of manufactured NTC ceramic pellets with reference sample

Composition	Density [g / mL]	Relative Density [%]	ρ_{25} [Ω·cm]	ρ_{85} [Ω·cm]	$B_{25/85}$ [K]	α_{25} [% / K]
Mn(2.4) Ni(0.5) Cu(0.1) O(4)	4.79 (SD 0.15)	93.1 (SD 3.0)	910 (SD 280)	120 (SD 30)	3600 (SD 40)	-4.1 (SD 0.05)
Mn(2.3) Ni(0.6) Cu(0.1) O(4)	5.12	99.5	330	45	3550	-4.0

3.7. Conclusions

As stated in the introduction to this chapter, It was important to develop my own composition since every composition needs a bespoke processing route (where all stages affect the final performance) since successful compositions and their exact processing conditions are never published since they are commercially valuable. Hence, bulk ceramic pellets were processed to determine the best processing conditions and techniques and to characterise their thermistor performance with the intention to carry-over the same processing conditions to produce ceramic fibres for flexible composites. It was discovered that the most sensitive manufacturing parameter is the physical pellet pressing process prior to sintering (to avoid cracks and defects), which will be interesting for the fibre sintering behaviour since the fibre spinning process doesn't involve pressing for compaction.

To conclude, chapter 2 used theory to select a NTC ceramic composition of $\mathrm{Mn_{2.2}Ni_{0.5}Cu_{0.3}O_4}$ that should give a $\rho_{25} \approx 12.6\ \Omega cm$ and a $B_{25/50} \approx 2960$ K. In practice, with our in-house manufacturing route a more suitable composition of $\mathrm{Mn_{2.4}\ Ni_{0.5}\ Cu_{0.1}\ O_4}$ was selected with a sintering scheme of $1200°C$ or $1250°C$ for 2.5 hours with a ramp of $180°C/hr$ that should give a relative density of 91-93%. The resistivity at $25°C$ (ρ_{25}) should be near 720 Ωcm, the resistivity at $85°C$ (ρ_{85}) should be close to 90 Ωcm, the B-value ($B_{25/85}$) near 3600 K and a temperature coefficient of resistance (α_{25}) close to -4.1 $\%/K$. Now we have a composition, bespoke processing conditions for bulk ceramic pellets and performance characteristics that will provide a benchmark for the ceramic fibres for functional granular composites, that is the subject of the following chapter.

4

Phase 3: Fibre Preparation

4.1. Introduction

The work of Stuber [54] has made promising advancements in using ceramic-fibres and polymer matrix composites for energy harvesting application. Potassium sodium niobate with 3 mol% lithium (KNLN3), with 5 mol% lithium (KNLN5), and PZT ceramic powders were used in a wet fibre spinning process that produced fibres that were sintered and embedded into a polymer matrix. This wet fibre spinning manufacturing technique can be adapted to a ceramic NTC thermistor system, which is the focus of this chapter. Ultimately, the NTC ceramic fibres will be used to produce a flexible temperature sensor by ceramic-fibre polymer-composites.

4.2. Fibre Spinning Process

According to Stuber [54] ceramic fibres of potassium sodium niobate (KNLN) were spun using a spin dope that was prepared using KNLN powder, cellulose acetate (CA) (Mn 30,000, Aldrich Chemistry), and acetone. The volume ratio of KNLN powder to CA powder is 1:1. The cellulose acetate needs to be dissolved in acetone, to form a solution of 20 wt% CA in acetone. Stuber noticed that the fibre spinning process was very sensitive to the total volume of KNLN included in the spin dope used for a single spinning session. The optimal spin dope used a KNLN volume equivalent to 12 grams of powder. Knowing $\rho_{KNLN} = 4.51 g/mL$, the optimal spin dope uses 2.66 mL of ceramic powder. For calcined $\mathrm{Mn_{2.4}\,Ni_{0.5}\,Cu_{0.1}\,O_4}$ powder, $\rho = 5.1430 g/mL$ so 2.66 mL translates to 13.68 grams of powder. Following a 50:50 volume ratio of cellulose acetate to ceramic powder, 3.41 grams of CA should be used given $\rho_{CA} = 1.28 g/mL$. To dissolve the cellulose acetate, 13.64 grams of acetone is needed to make a solution of 20 $wt\%$ CA in acetone. This gives a total spin dope of 13.68g of NiMnCuO, 3.41g of CA, and 13.64g of acetone to combine into the optimum spin dope for the wet fibre spinning setup. The spin dope is prepared by firstly mixing the NiMnCuO powder and CA powder in a 60 mL sealed cup and mixed at 1500 RPM for 5 minutes in a speed mixer. The acetone is then added and mixed again at 1500 RPM for 5 minutes. To ensure thorough mixing and a uniform consistency, a spatula is used to scrape the bottom of the cup to check if there is any sedimentation. If there is any sedimentation, the solution is mixed again using the speed mixer. If the solution is consistent, then the cup is sealed until used for fibre spinning. The acetone evaporates quickly, and care needs to be taken to avoid that too much evaporation takes place, or it will affect the quality of the fibres that are spun.

The fibre spinning technique used is the exact same as Stuber [54], where the setup is depicted in figure 4.1. The spin dope gets poured into the spin tube, where the piston head lowers and forces the spin dope to be extruded through the spin head which is submerged in the water bath of deionised water. The configuration in the spin head is depicted in figure 4.2. It includes a spinneret with 6 holes of 100 μm diameter from which the fibres are extruded. There is a 325 μm mesh to ensure that no aggregate particles can block the holes or become part of the fibres. Polytetrafluoretheen (PTFE) washers are used to space and support the mesh and spinneret. When the extruded fibres contact the water bath, the acetone evaporates and the cellulose acetate solidifies, binding the NiMnCuO powder into a green fibre (i.e. un-sintered fibre). The fibres are pulled and wound by a fibre winder and supported by the

black supports of the spin bath and the separate supports depicted in figure 4.1. The fibre winder helps to stretch the fibres and helps with the extrusion process, by pulling the fibres out the spinhead.

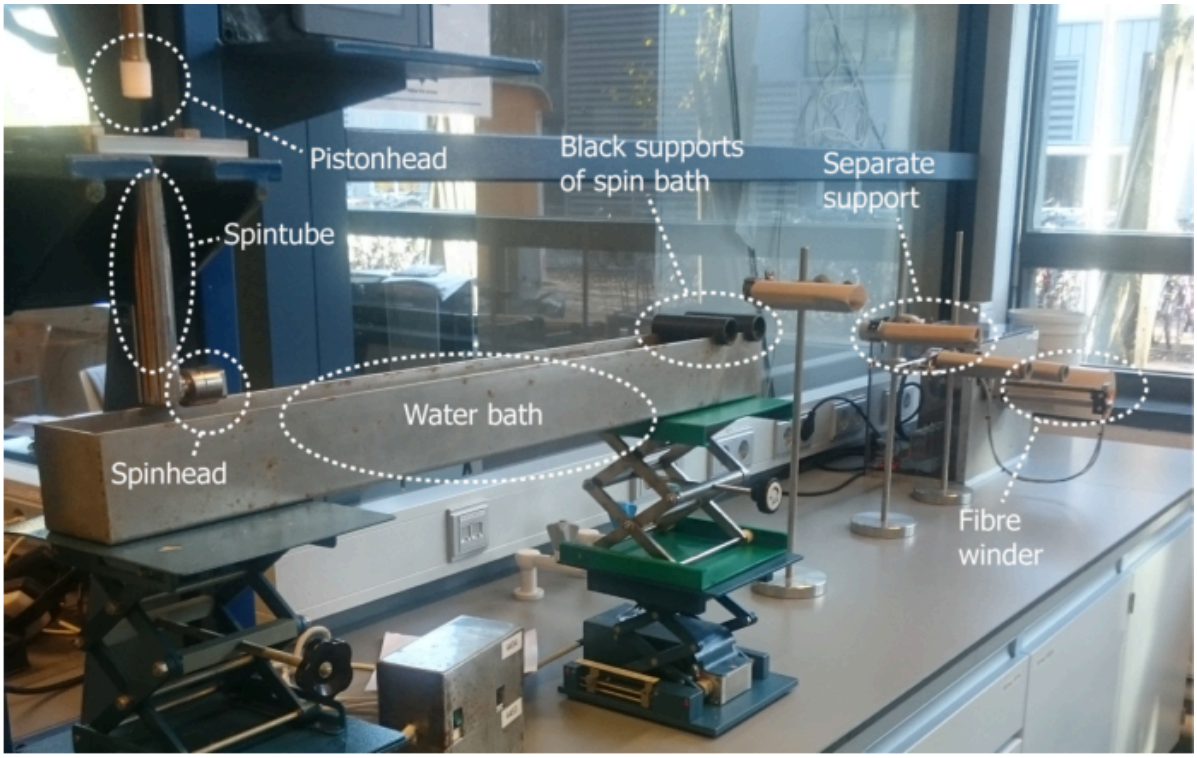

Figure 4.1: Experimental Setup of Wet Fibre Spinning Technique [54] for ceramic fibres

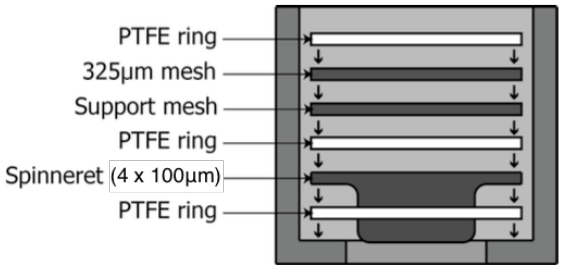

Figure 4.2: Experimental Setup of Spin Head [54]

4.2.1. Fibre Spinning Procedure

The piston head is lowered to a position just above the top of the spin tube, then the spin dope is quickly poured into the spin tube using a spatula to help scrape all of the solution, while avoiding any dried solutes. This must be done as fast as possible to avoid the acetone evaporating. The piston head is then lowered using a speed of 1500 units (TU-Delft in-house setup and unit, approximately equal to a piston head speed of 1.9 cm/min). When spin-dope starts emerging from the spin head the speed is reduced to 150 units (approximately 0.2 cm/min) and the water bath is raised to submerge the spin head under water. Fibres are extruded in the water bath and grabbed using tweezers, and pulled in a smooth motion over the supports of the spin bath and over the separate supports and onto the fibre winder (Set at a speed of 3 units, of the TU Delft in-house setup that is approximately equal to 75 RPM or 2400 cm/min). After some of the fibre starts being wound, the speed of the fibre winder is increased to 6 units (approximately equal to 5200 cm/min) so that the fibre is stretched thinner. The speed of

fibre extrusion is about 2000 cm/min, giving a stretch ratio with the fibre winder of about 2.6.

The fibre spinning process needs to be continuously supervised since the extruded fibres sometimes break or a hole on the spinneret gets blocked. The spinneret might need some scraping and the new fibres need to be pulled and fed to the fibre winder. The spun fibres are wound on the cylinder of the fibre winder and are left there to dry. They are then removed and placed into an oven at $100°C$ for 1 hour to ensure they are dry. The amount of fibres produced in a single run can vary depending on how many spinneret holes become blocked during the spinning process.

4.3. Fibre Sintering

The green ceramic fibres need to be sintered, similar to the pressed pellets, to undergo densification. With the bulk ceramic pellets, a sintering scheme of $1200°C$ or $1250°C$ for 2.5 hours with a ramp of $180°C/hr$ was determine to be best for the composition of $\mathrm{Mn_{2.4}\,Ni_{0.5}\,Cu_{0.1}\,O_4}$. However, the pellets of $\mathrm{Mn_{2.4}\,Ni_{0.5}\,Cu_{0.1}\,O_4}$ used the binder; polyethylene glycol with molecular weight $M_w = 20,000$ in a ratio of $50g : 1.5g$ of $\mathrm{MnCuNiO}$: PEG. The fibres used a significantly higher ratio of binder with 13.68g : 3.41g of NiMnCuO to cellulose acetate (Mn = 30,000). This prompted the need to investigate whether a special binder burn-out step was required. Three different sintering schemes were investigated with fibre sintering. They are presented in table 4.1. Scheme A, is the same sintering treatment as the ceramic pellets ($1200°C$ for 2.5hrs with a ramp of $180°C/hr$), with the addition of a binder burnout step ($400°C$ for 1min with a ramp of $100°C/hr$) which is basically just a slower heating ramp to ensure all the binder is slowly and completely burnt-out. Fibre densification occurs through shrinkage only, whereas pellets are densified by mechanical pressing with high pressure and shrinkage. Hence, Scheme B raises the sintering temperature and time to hopefully provide more time and energy for densification. It also simultaneously tests if a specific binder burn-out step is really necessary. Scheme C is a variation of Scheme B, and is designed to test if the heating rate has an effect on the sintered fibres. For industrial purposes, a faster heating ramp translates to a quicker process which is beneficial.

Table 4.1: Fibre Sintering Schemes

Scheme	Parameters
A	Step 1: 400°C for 1 min with 100°C/hr ramp Step 2: 1200°C for 2.5 hours with 180°C/hr ramp
B	Step 1: 1250°C for 6 hours with 180°C/hr ramp
C	Step 1: 1250°C for 6 hours with 300°C/hr ramp

Before sintering, the green fibres are tough and very easy to handle. They appear and feel very much like human hair, as can be seen in figure 4.3. After sintering, they are much thinner and very brittle to the touch.

(a) Greem Fibres (b) Sintered Fibres (c) Sintered Fibres

Figure 4.3: Fibres before and after sintering

4.3.1. Fibre Sintering Scheme A vs B

Due to the nature of the sintered fibres being small and brittle, measuring their resistance directly is very difficult. The ceramic fibres break when handled and so directly measuring the thermistor performance characteristics is not possible. Instead, SEM images will be taken to compare their microstructure.

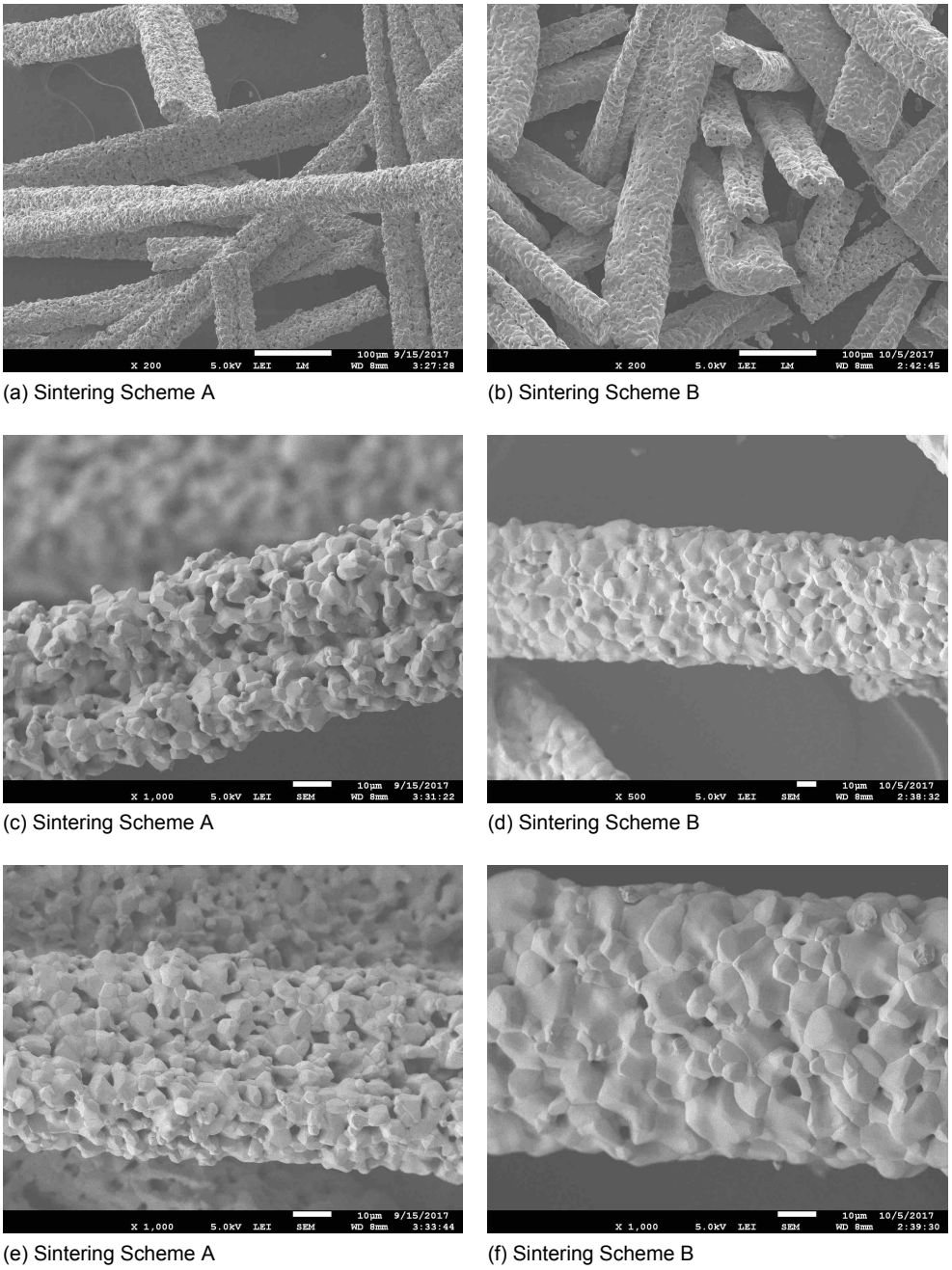

(a) Sintering Scheme A (b) Sintering Scheme B

(c) Sintering Scheme A (d) Sintering Scheme B

(e) Sintering Scheme A (f) Sintering Scheme B

Figure 4.4: SEM images of sintered fibres of $\mathrm{Mn_{2.4}\,Ni_{0.5}\,Cu_{0.1}\,O_4}$ comparing sintering scheme A to B at low and high magnification

As can be seen from the SEM images in figure 4.4, the fibres sintered with scheme A have high porosity and are not as dense as their pellet counterpart, despite undergoing similar sintering schemes. A comparison is given in figure 4.5. This is mainly due to two reasons. The first is due to the high amount of cellulose acetate used as binder that was necessary for fibre production, but leaves large significant space when burn-out that the NiMnCuO particles need to diffuse across to form a dense ceramic fibre. The second, is the fibres didn't experience much mechanical pressing (beyond the pressure involved in

extrusion) which is the most critical factor for obtaining high density ceramic pellets. Sintering Scheme B was designed to try to compensate for this and increased the sintering temperature to $1250°C$ and extended the sintering time to 6 hours to provide more time and energy for densification. It is evident from the figure 4.4 that it was successful in producing denser ceramic fibres. Also, sintering scheme B proves that a specific binder burn-out scheme is unnecessary and that a heating ramp of $180°C/hr$ is sufficiently slow to provide complete and thorough burn-out of the binder.

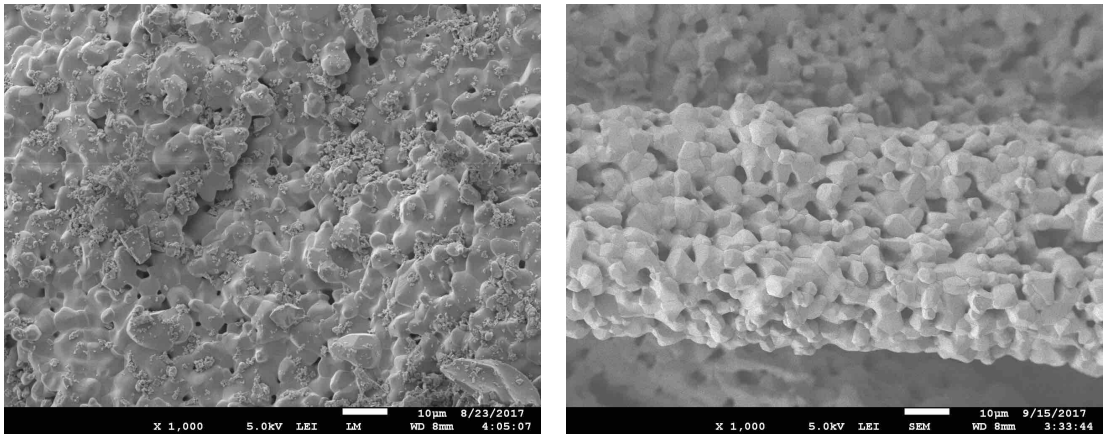

(a) Sintered Pellet (b) Sintered Fibre

Figure 4.5: SEM images of microstructure of pellet sintered at $1200°C$ for 2.5 hrs with ramp of $180°C/hr$ versus fibre sintered with Scheme A, both of composition $Mn_{2.4}\,Ni_{0.5}\,Cu_{0.1}\,O_4$, at the same magnification

XRD was performed on the ceramic fibre and compared to the calcined powder, sintered pellet, and reference pattern of $Mn_{2.17}\,Ni_{0.7}\,Cu_{0.13}\,O_4$, presented in figure 4.6. The pattern of the sintered fibre is very diffused because the XRD is designed for powder specimens and the crushed and compacted fibres were held in an amorphous putty. The pile of fibres had elevation differences which contributed to the pattern having low and diffused peaks. However, the distinguishable peaks still match at the right angles and seems to indicate that the fibre is a single phase.

4.3.2. Fibre Sintering Scheme B vs C

Sintering scheme B and C are both $1250°C$ for 6 hours, but Scheme B has a heating ramp of $180°C/hr$ while Scheme C has a heating ramp of $300°C/hr$. A faster heating ramp would be beneficial as it translates to a quicker process, but its effect on the densification of the fibre is unknown and interesting to investigate. As can be seen from figure 4.7, the faster heating ramp had very little effect on the overall density of the ceramic fibre. The porosity, crystal size and distribution are comparable on the ceramic fibres from both sintering schemes.

SEM images can only give a sense of the microstructure on the outside of the fibre, it has been observed with other systems that hollow fibres can be created due to the process of the binder burning out. However SEM images of the fibres show that completely solid fibres were produced, but they are oddly flat shaped, as can be seen in figure 4.8. This is probably due to the fibre forming a hollow core and then collapsing upon further densification.

4.3.3. Fibre Width

Image processing software (imageJ) was used on the SEM images of the fibres to measure the average width of the sintered fibres. Fibres sintered with Scheme A had an average width of 62 μm, while fibres sintered with Scheme B had an average width of 83 μm. Fibres sintered with Scheme C had an average width of 78 μm. It was observed that the average width of the fibres are more sensitive to the fibre spinning process, rather than the sintering scheme. Some problems with spinning occurred with the batches used for sintering scheme B and C, which led to a larger average fibre width and a greater spread of distribution in the fibre width observed. The stretching in the wet fibre spinning process is the most critical factor to control the final fibre width.

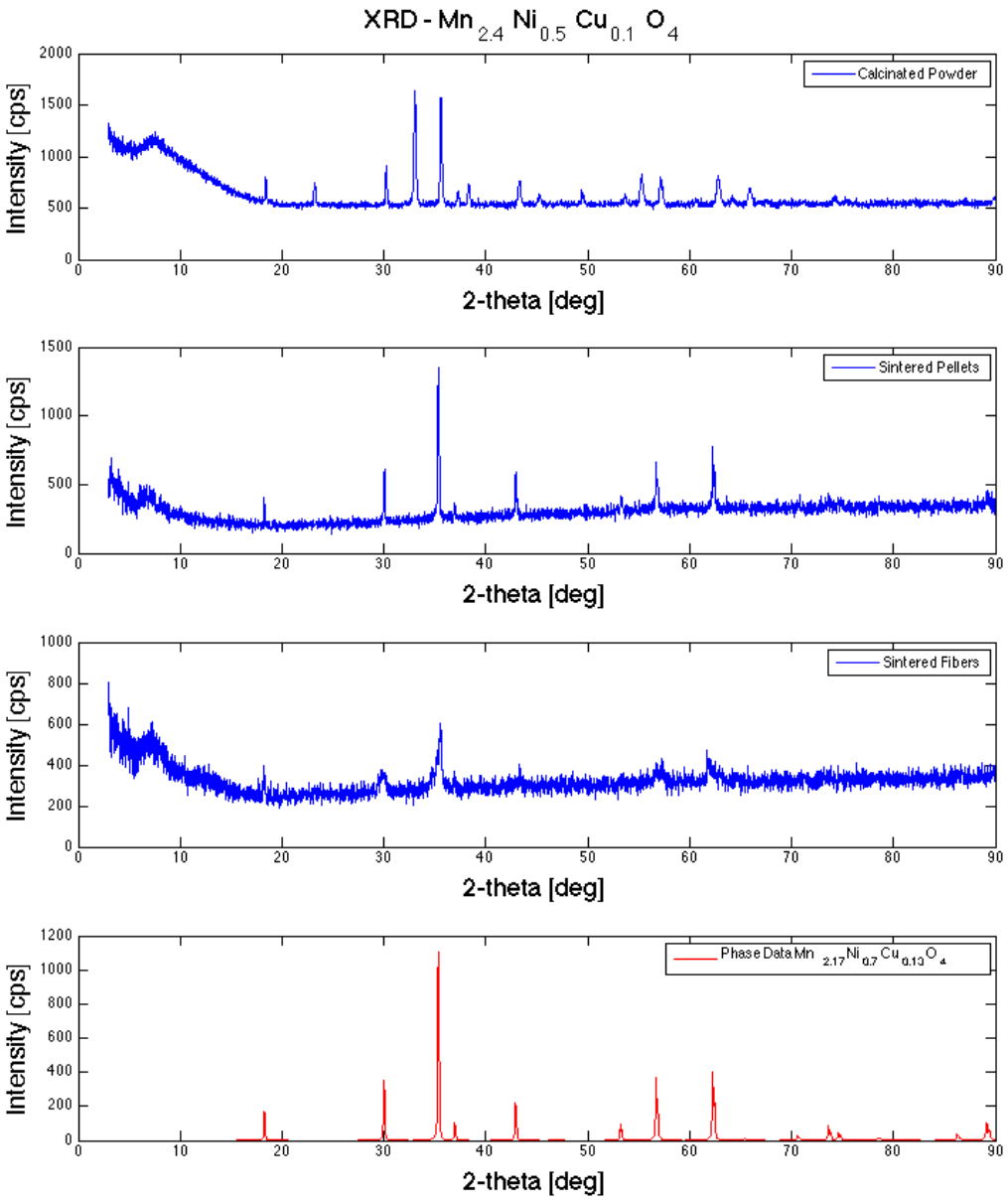

Figure 4.6: Comparison of XRD pattern of calcined powder, sintered pellets and sintered fibres of $Mn_{2.4}\,Ni_{0.5}\,Cu_{0.1}\,O_4$ compared to reference pattern of $Mn_{2.17}\,Ni_{0.7}\,Cu_{0.13}\,O_4$

4.4. Conclusion

Green ceramic fibres of $Mn_{2.4}\,Ni_{0.5}\,Cu_{0.1}\,O_4$ were produced via fibre spinning that was successfully adapted from the work of Stuber [54]. Three fibre sintering schemes were tested and their effect on the densification of the ceramic fibre was observed using scanning electron microscopy. There is a clear improvement in higher obtainable density with scheme B and C, over scheme A. However, due to the fragile nature of the brittle ceramic fibres, their thermistor performance could not be measured without embedding them into a composite. This is the focus of the following chapters.

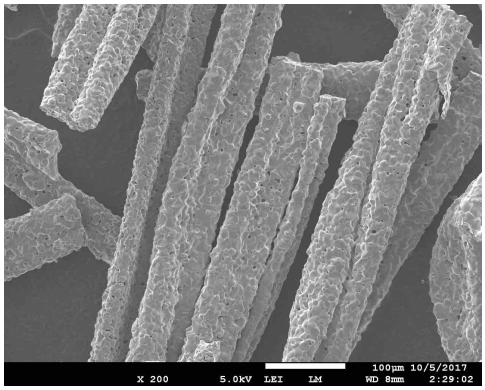

(a) Sintering Scheme B

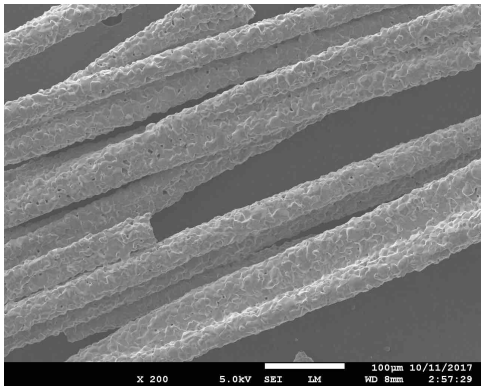

(b) Sintering Scheme C

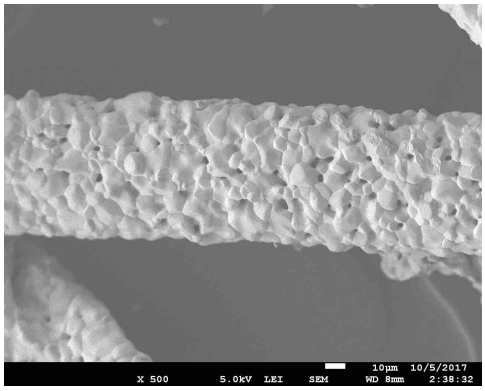

(c) Sintering Scheme B

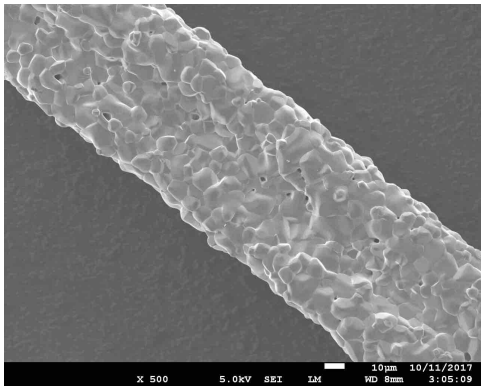

(d) Sintering Scheme C

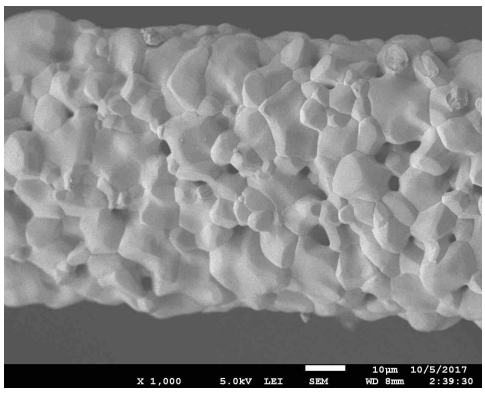

(e) Sintering Scheme B

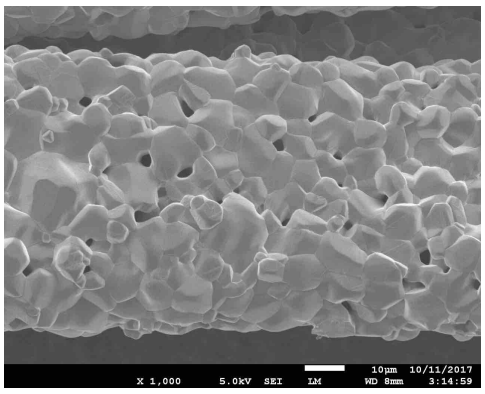

(f) Sintering Scheme C

Figure 4.7: SEM images of sintered fibres of $\mathrm{Mn}_{2.4}\,\mathrm{Ni}_{0.5}\,\mathrm{Cu}_{0.1}\,\mathrm{O}_4$ comparing sintering scheme B to C at low and high magnification

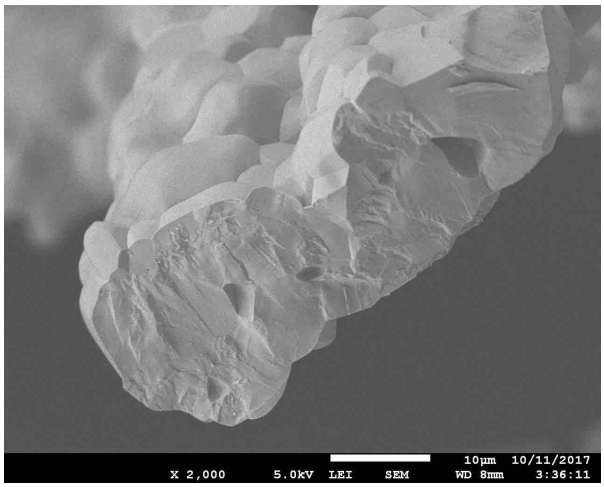

Figure 4.8: SEM image of fibre end

5

Phase 4: Ceramic Fibre - Polymer Matrix Composites

5.1. Introduction

Many composite thermistor systems that used polymer matrices or substrates were reviewed in Literature. A summary of the polymer matrices and substrates that were used is presented in tables C.1 and C.2 in Appendix C. According to [11], composite systems of conductive filler particles in polymer matrices can show NTC or PTC behaviour depending on the characteristics of the polymer and the filler. As already discussed, the filler particle's aspect ratio, shape, particle size and volume content all play a role. For the polymer, it's thermal expansion coefficient, melting point, stiffness, and glass transition temperature also influence the system. The list below gives a sense of the selection criteria involved in selecting an appropriate polymer matrix:

Selection Criteria: Preferred characteristics for polymer matrix

- Want low intrinsic resistivity without forming a conductive network of its own.
- Want low/bad wetting properties.
- Want high shrinkage of curing of polymer matrix.
- Want low heat capacity so that the sensor can obtain a quick and accurate response.
- Want high thermal conductivity to lower thermistor time delay.
- Want short working time so that heavy fibres do not sink and aggregate.
- Want low stiffness to have high flexibility and stretchability.
- Want low thermal expansion coefficient to avoid PTC effect.
- Want glass transition temperature to correlate with intended operating temperature

Conductive polymers (e.g. PEDOT:PSS) are avoided because they tend to be complex to process, sensitive to moisture, and expensive. Moreover, if they are too conductive, there is a danger that a short circuit is formed. The polymer-filler interaction can be very complex depending on the exact system. Evident from the literature study is that there is no single, optimal polymer. Instead trade-offs need to be made, and polymer selection is often trial based, so it is necessary to test the filler particles with a variety of polymer matrices.

5.2. Candidate Polymers for Composite Matrix

Three candidate polymers were chosen for the polymer matrix. Polydimethylsiloxane (PDMS) (Slygard 184, Dow Corning), Bisbenzocyclobutene (BCB) (Cyclotene 3022-35, Dow) and Electrodag (Loctite NCI 7002 E&C, Henkel Electronic Materials, Belgium).

Polydimethylsiloxane (PDMS) (Slygard 184, Dow Corning) is readily available and used for many applications due to its many advantages.

Advantages of using PDMS

- Simple and convenient processing (long shelf life and working time)
- Easy to obtain (readily available, relatively cheap)
- Compatible with metals and ceramics, and good biocompatibility.
- Good stiffness/flexibility
- Low curing temperature and short curing time
- Optically transparent
- Relatively low dielectric constant (2.72 at 100Hz)
- Relatively high thermal conductivity (0.27 Watts per meter K)

Bisbenzocyclobutene (BCB) (Cyclotene 3022-35, Dow) is used in microelectronic packaging and interconnect applications. Mainly used as coatings for microchips (e.g. silicon wafers) for dielectric isolation, moisture barrier, bonding (wafer-to-wafer adhesion), and planarization (i.e. surface leveling). It's advantages include:

Advantages of using BCB

- Has low dielectric constant (will insulate against electrical current loss and electrical field interference).
- Low moisture absorption
- Low cure temperature (1-2 hrs at $200°C$)
- High degree of planarization
- Low level of ionic contaminants
- High optical clarity
- Good thermal stability (up to $350°C$)
- High chemical resistance
- Good compatibility with various metallization systems [compatibility with copper, prevents copper electromigration]
- Rapid thermal curing
- Doesn't emit any volatiles in curing process.

Electrodag (Loctite NCI 7002 E&C, Henkel Electronic Materials, Belgium) is used in blends for force sensitive inks with tunable resistance and sensitivity profiles. Part of a 2 component force sensing ink (ECI 7004 E&C and ECI 7002 E&C). Designed for force sensitive resistors for medical, consumer electronic, industrial, musical and commercial applications. NCI 7002 E&C is the non-conductive element. It's advantages include:

Advantages of using Electrodag

- Good consistency (higher viscosity).
- Suitable for screen-print applications.
- Excellent screen residence time.
- Allows low temperature drying (1-2 hrs at $130°C$).
- Good adhesion to treated PET
- Success with NTC powder at Holst Centre

5.3. Composite Thermistor Architecture

Composite thermistors of ceramic fibre particles of NiMnCuO were made by mixing them in a polymer matrix. However, different from the ceramic pellets, the composite architecture needs a different electrode design so that we can measure its electrical resistance. Inkjet and stencil printed silver interdigitate electrodes on a polyethylene terephthalate (PET) substrate were obtained from the Holst Centre, Eindhoven. These electrodes are circular with a diameter of 6 mm and are presented in figures 5.2. The PET substrate is 125 μm in thickness and the silver electrodes are around 15 μm in thickness. Two different interdigitate electrodes are available with 0.13 mm or 0.20 mm gap sizes. Composites of fibre particles and polymer matrix will be drop coated and cured on the silver electrodes on the PET substrate. This thin-film architecture will enable the resistance of the composite to be measured using the silver electrode leads.

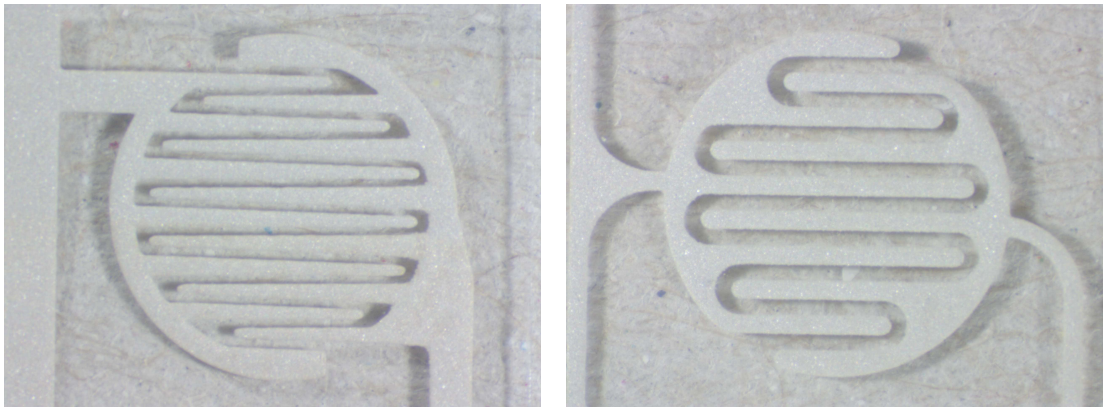

(a) Inkjet Printed - Electrode gap 0.13 mm (b) Stencil Printed - Electrode gap 0.20 mm

Figure 5.1: Optical images of silver interdigitate electrodes on PET substrate

For the connectivity of the composite, two options are available. The first is to make an isotropic mix of fibres and polymer matrix. According to the theory on functional granular composite, beyond a certain volume fraction (or weight fraction) of fibre filler particles a percolated network forms. This is illustrated in figure 5.2a. The advantages of an 0-3 composite is that it is easy to manufacture and delivers consistent and uniform performance since it is isotropic. The second option, is to try to exploit the use of long, fibre particles and try to control their placement so that the fibres are in contact with each other, the electrodes, and bridge the electrode gap as efficiently as possible. This can be done simply by aligning the fibres perpendicular to the interdigitate electrodes, stacking them together, and then encapsulating them with the polymer matrix. This is illustrated in figure 5.2b. This would hopefully ensure fibre to electrode contact, as well as fibre to fibre contact before encapsulation with the polymer so that tunnelling resistance doesn't dominate. This is effectively a quasi 3-3 composite. Furthermore, the composite would not be isotropic but with controlled fibre placement, a lower fibre content could potentially be used compared to its isotropic counterpart.

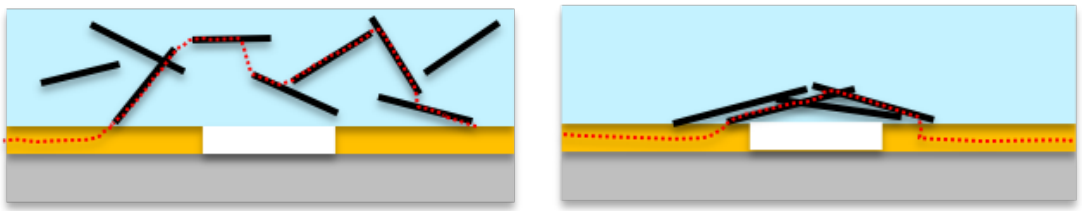

(a) Isotropic Mix - 0-3 Composite (b) Fibre Placement - quasi 3-3 Composite

Figure 5.2: Schematic of Composite Connectivity

The fibres used for the production of the composites are broken into smaller fibre particles. This is performed by hand in a crucible with a spatula. Using an optical microscope (Keyence, VHX 2000, Osaka, Japan) and image processing software (ImageJ) the fibres are on average 569 μm in length with a standard deviation of 288 μm. The spread is quite large with small fibres as small as 63 μm and long fibres as long as 1430 μm in length.

5.4. Characterisation of Electrical Performance - Experimental Setup

To measure the resistance of the composite thermistors at a certain temperature, the same experimental setup that was described in section 3.4.1 was used. DC resistance measurements were performed using a Keithley Model 2000 Multimeter using the 4-wire resistance setting. However the previous setup used a custom device, shown in figure 3.3a, to hold the pellets and to electrically connect them to the multimeter. To connect to the thermistor composites that are on thin film PET substrates, crocodile clips were used to clamp down onto the substrate and contact the electrode leads. The substrate needed to be placed on a rigid support to prevent the tension from the crocodile clips to bend the flexible thermistor, causing a change in the measured resistance. The rigid support was a simple piece of metal, wrapped with an electrically insulating tape so that it wouldn't short circuit the measurement setup. A picture of the setup is shown in figure 5.3. The same oil bath (Lauda K20) with sunflower oil was used to keep a steady state temperature for resistance measurements, however the composite thermistors and electrical leads were placed in a chemically resistant latex glove to avoid the direct contact of the specimen and electrical equipment with the oil.

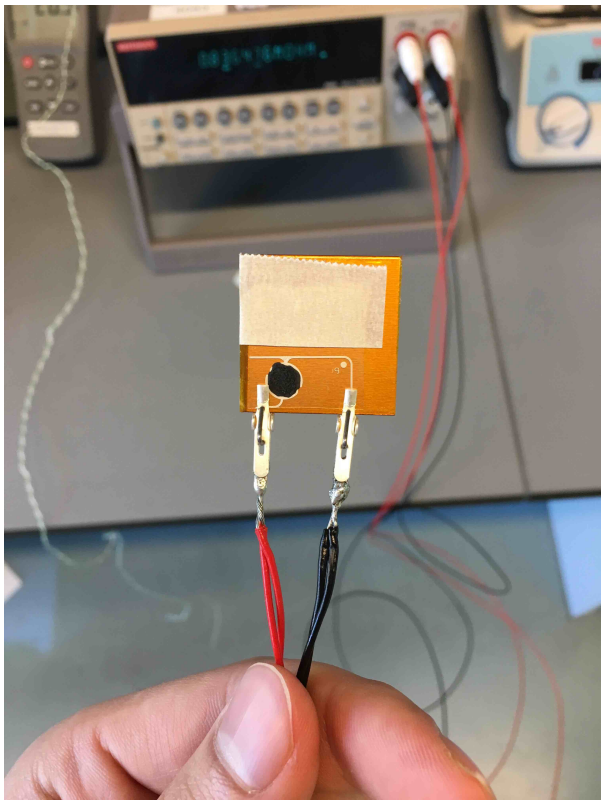

Figure 5.3: Experimental Setup to Composite Thermistor

5.5. Results of PDMS - NiMnCuO Composites

Isotropic composites of NiMnCuO fibres that were sintered using scheme B were made using the inkjet printed interdigitate electrodes (IDE) with an electrode gap of 0.13 mm. As previously mentioned, the fibres were broken into smaller fibre particles so that they can be used in the isotropic composite. Polydimethylsiloxane (PDMS) (Slygard 184, Dow Corning) was firstly prepared by a two part solution,

with part A being the base material and part B being the catalyser that needs to be mixed in a 10:1 ratio. An excess amount is prepared and mixed in a speed mixer at 2500 RPM for 5 minutes. Two batches of isotropic composites were made. Batch A had 16 $wt\%$ fibres, while batch B had an increased 28 $wt\%$ of fibres. Different amounts of batch A and batch B mixtures were deposited by drop coating on 8 electrodes. The PDMS-NiMnCuO composites were then cured at $100°C$ for 35 minutes on a hotplate. The resistance at $25°C$ and $85°C$ were subsequently measured, for which the results are shown in table 5.1.

Table 5.1: Resistance Values of Isotropic PDMS-NiMnCuO composites

Sample	Fiber wt%	Composite wt [g]	Electrode Gap [mm]	R_{25} [MΩ]	R_{85} [MΩ]
A1	16%	0.0316	0.20	Non-conductive	Non-conductive
A2	16%	0.0269	0.20	6.050	Overflow (>120MΩ)
A3	16%	0.0196	0.20	2.990	10.950
A4	16%	0.0275	0.20	Non-conductive	Non-conductive
B1	28%	0.0268	0.20	Non-conductive	Non-conductive
B2	28%	0.0422	0.20	1.810	Overflow (>120MΩ)
B3	28%	0.0183	0.20	2.930	Overflow (>120MΩ)
B4	28%	0.0182	0.20	4.120	Overflow (>120MΩ)

Surprisingly, the PDMS-NiMnCuO composites displayed a PTC effect when exposed to increasing temperature. The resistance at $85°C$ was unmeasurable for most samples since the resistance increased beyond the range that the Keithley 2000 multimeter can measure (R >120 $M\Omega$). For the isotropic composites with 16 $wt\%$ of fibres, 2 out of the 4 samples were non-conductive. One of the samples (A3) is given in figure 5.4a. For the isotropic composites with 28 $wt\%$ of fibres, only 1 was non-conductive, but samples B3 and B4 show that with the same amount of fibre, the resistance at $25°C$ can vary from 2.930 $M\Omega$ to 4.120 $M\Omega$.This is probably due to the tunnelling resistivity being the dominate factor in the overall resistivity of the composite. Sample (B3) is shown in figure 5.4b.

This is why fibre placement, schematically illustrated in figure 5.2b, can potentially produce better performance (by orders of magnitude) since the fibres should have direct contact with each other and the electrodes so that tunnelling resistance doesn't dominate. Hence, different amounts of fibres were placed onto the electrodes, but due to the short length of the fibres, controlling their direction proved to be too difficult. After placing the fibres, mixed PDMS is applied via syringe to encapsulate all the fibres, and then placed onto a hotplate at $100°C$ for 35 minutes to cure. The resistance at $25°C$ and $85°C$ were measured, for which the results are shown in table 5.2.

Table 5.2: Resistance Values of Fibre-Placed PDMS-NiMnCuO composites

Sample	Fiber wt [g]	Electrode Gap [mm]	R_{25} [MΩ]	R_{85} [MΩ]
C1	0.0135	0.20	4.110	Overflow (>120MΩ)
C2	0.0152	0.20	5.160	Overflow (>120MΩ)
C3	0.0265	0.20	Non-conductive	Non-conductive
C4	0.0165	0.20	4.370	Overflow (>120MΩ)

Fibre-placed composite sample C4 is shown in figure 5.4c. Evident from the resistance results in table 5.2 is that there is still a PTC effect and the resistance at $25°C$ is higher than the isotropic composites, that use lower amounts of fibres. Fibre placed composites should have quasi 3-3 composite connectivity, however the PDMS wettability has proven to be very high and are 0-3 composites where

tunnelling resistivity dominates. To be sure this isn't dependent on the fact that fibres from sintering scheme B were used, more fibre-placed composites were made using fibres from sintering scheme A and C. Much larger, amounts of fibre were used including the interdigitate electrodes with smaller electrode gap of 0.13 mm to see if the resistance can drop by orders of magnitude. Resistance was measured at room temperature to make measurements quicker and $85°C$ to see if the response to temperature still shows a PTC effect. The results are given in table 5.3.

Table 5.3: Fibre-Placed PDMS-NiMnCuO composites using differently sintered fibres

Fibres from Sintering Scheme	Sample	Fiber wt [g]	Electrode Gap [mm]	$R_{19.6}$ [MΩ]	Response
A	D1	0.0152	0.13	1.460	PTC
	D2	0.0115	0.13	1.760	PTC
	D3	0.0128	0.13	1.510	PTC
B	D4	0.0310	0.13	1.500	PTC
	D5	0.0448	0.13	1.340	PTC
C	D6	0.0396	0.13	2.820	PTC
	D7	0.0423	0.13	2.270	PTC

The results from table 5.3 confirm that the PDMS-NiMnCuO fibre placed composites have their overall resistance dominated by tunneling resistivity. This is why fibres from sintering scheme A (which are visibly much less dense, seen in the SEM images of figure 4.4) still have the same resistivity at room temperature as composites using fibres from sintering scheme B, despite using much lower amount of fibres.

(a) Isotropic Composite - 16 $wt\%$ of fibres

(b) Isotropic Composite - 28 $wt\%$ of fibres

(c) Fibre-Placed Composite

Figure 5.4: Optical images of PDMS-NiMnCuO composite thermistors on PET substrate

5.5.1. Conclusions

To conclude, PDMS-NiMnCuO composite thermistors show an overall PTC effect, due to the high thermal expansion coefficient of the PDMS (linear CTE $\approx 263 \cdot 10^{-6}\ °C^{-1}$ at $23°C$ [29]). A PTC thermistor has some advantages over a NTC thermistor, but the PTC effect was observed to be non-linear and therefore unusable for temperature sensing. It was observed that when low heat is applied, the resistance can go slightly down due to the NTC ceramic fibre behaviour even with the expansion of the PDMS, the conductive fibre network is still intact. With high heat, the PDMS expands to a point where the electrical network breaks and only returns upon cooling. This process was observed as reversible and repeatable, so the composite could possiblly be used as a switch. However, it is hard to know the exact cutoff temperature ($60 - 85°C$) and resistance at which the electrical connection breaks due to

the randomness of the fibre network, and the time delay of polymer heat conduction. The PDMS also proves to be too wet, able to coat fibres that are already touching (turning quasi 3-3 composites to 0-3 composites) and causing tunnelling resistivity to dominate. Hence, a higher quantity of fibre doesn't necessarily reduce the overall resistivity. Due to these reasons, PDMS is unfortunately not suitable as a polymer for composite thermistors.

5.6. Results of BCB - NiMnCuO Composites

BCB-NiMnCuO composites were made in the same manner as the PDMS-NiMnCuO composites. Fibres (sintered using scheme B) were broken into smaller particles and mixed with a speed mixer (2500 RPM for 5 minutes) with BCB to form an isotropic mix. BCB cures at $200°C$ for 1 hour, which is too close to the melting point of PET ($\approx 250°C$). Kapton substrates with stencil printed silver electrodes were obtained to be able to cure at the higher temperature needed. Unfortunately, the viscosity of the BCB is too low, and curing cannot occur quick enough to avoid the bleeding out of the polymer matrix. As can be seen from figure 5.5, it was practically too difficult to form a consistent isotropic mixture due to the low viscosity of the BCB. Hence, from a processing viewpoint, BCB is also not suitable as a polymer for composite thermistors.

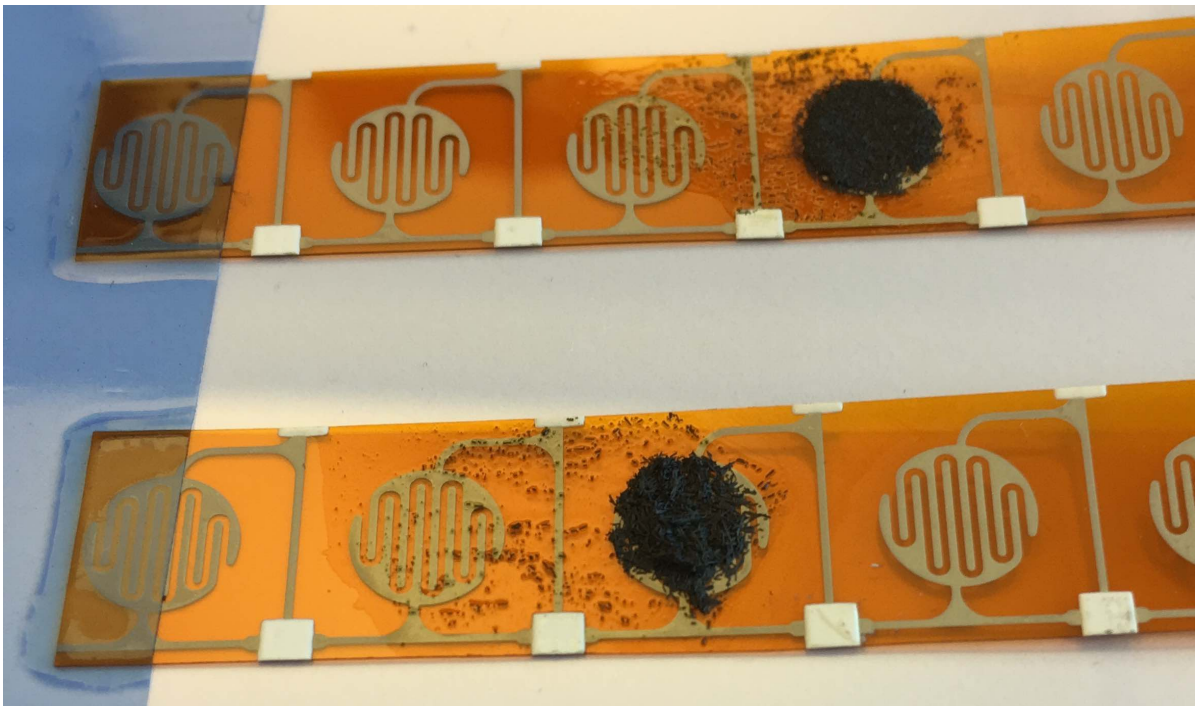

Figure 5.5: BCB-NiMnCuO Composites on Kapton substrates with stencil printed silver electrodes

5.7. Results of Electrodag - NiMnCuO Composites

Electrodag (Loctite NCI 7002 E&C, Henkel Electronic Materials, Belgium) is part of a 2 component force sensing ink (ECI 7004 E&C and ECI 7002 E&C) that is blended together to tune the resistance and sensitivity profiles. NCI 7002 E&C is the more resistive element that will be used for the polymer matrix of Electrodag-NiMnCuO composites. The viscosity of Electrodag is much higher, making it easier to handle and process. Samples were made by fibre placement, described schematically in figure 5.2b, in an attempt to produce quasi 3-3 composites and cured at $130°C$ for 1 hour. Fibres (sintered using scheme B) were placed onto the electrodes and then encapsulated with the Electrodag polymer. However, the Electrodag proves to be very viscous and does not diffuse evenly through the fibre pile to encapsulate all the fibres. Instead it remains as a separate phase, on top of the fibres. Upon curing, the entire composite curls and peels off the electrodes or cracks, as can be seen in figure 5.6. More success was obtained with an isotropic mix, creating (0-3) composites.

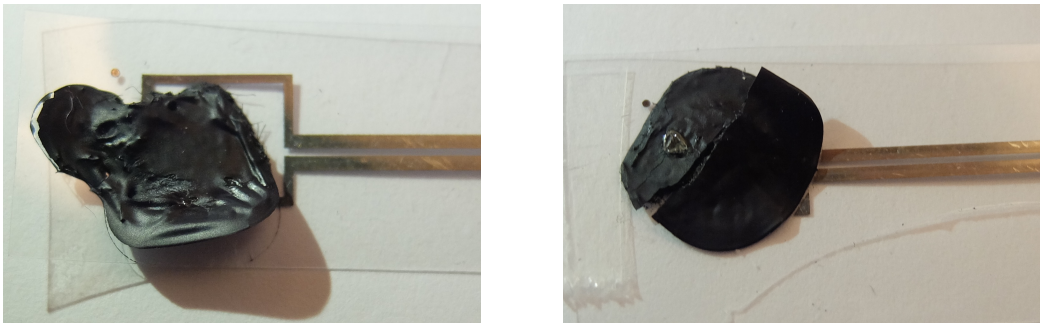

(a) (b)

Figure 5.6: Optical images of Fibre-Placed Electrodag-NiMnCuO composite thermistors on PET substrate

Isotropic (0-3) composites were made in the same manner as the isotropic PDMS-NiMnCuO and BCB-NiMnCuO composites. Fibres particles (sintered using scheme B) were mixed with a speed mixer (2500 RPM for 5 minutes) with Electrodag to form an isotropic mix, and drop coated onto the electrodes. They were then cured at $130^{\circ}C$ for 1 hour in an oven. A more consistent isotropic composite is formed as can be seen from figure 5.7a. Five test samples were made and their resistance at $25^{\circ}C$ and $85^{\circ}C$ was measured, and its corresponding B-value was calculated and presented in table 5.4.

Table 5.4: Resistance Values of Isotropic Electrodag-NiMnCuO composites

Sample	Fiber wt%	Composite wt [g]	Electrode Gap [mm]	R_{25} [MΩ]	R_{85} [MΩ]	$B_{25/85}$ [K]
E1	23.20	0.0197	0.13	1.930	0.310	3254
E2	23.20	0.0159	0.13	1.910	0.250	3619
E3	23.20	0.0054	0.20	10.240	3.510	1906
E4	23.20	0.0168	0.20	Overflow	Overflow	-
E5	23.20	0.0138	0.20	Overflow	Overflow	-

As can be seen from the results in table 5.4, 3 specimens showed a NTC effect albeit at high resistances in the $M\Omega$ range. 2 specimens were so high in resistance it exceeded the maximum 120 $M\Omega$ that the Keithley Model 2000 Multimeter could measure. From experimental observations and consultation with experts from TNO, Holst Centre, Electrodag is designed to be used as a thin film. It is very sensitive to the applied thickness and thicker layers can induce stress upon curing that is detrimental to its performance. Hence, the NTC performance with high B-values obtained are promising, but thinner deposition of the Electrodag is needed for better and more consistent performance across specimens. Diluting the Electrodag with 20 wt% Isopropyl alcohol (IPA) enabled thinner depositions of the electrodag, which then correlated to lower resistances that can be seen in table 5.5. However, this caused the Electrodag composition to become unstable and 24 hours after curing, the Electrodag cracks and delaminates. Figure 5.7b illustrates the instability of Electrodag diluted with IPA which cracks and delaminated 24 hours after it has been cured.

Evident from the resistance values from table 5.5 as compared to the resistance values obtain in table 5.4, is that thinner deposition of Electrodag leads to lower resistivity, despite using the same fibre content. E.g. comparing sample F1 to E1, both R_{25} and R_{85} are significantly lower. However, achieving a thinner deposition of electrodag is unsuitable by diluting with IPA because it causes the electrodag to become unstable. Instead, a better, more reproducible technique should be used like stencil printing, which is the subject of the next chapter.

Table 5.5: Resistance Values of Isotropic Electrodag-NiMnCuO composites diluted with isopropyl alcohol

Sample	Fiber wt%	Composite wt [g]	Electrode Gap [mm]	R_{25} [kΩ]	R_{85} [kΩ]	$B_{25/85}$ [K]
F1	23.20	0.0197	0.13	1000	170	3154
F2	23.20	0.0141	0.13	315	100	2042
F3	23.20	0.0244	0.20	Overflow	Overflow	-
F4	23.20	0.0880	0.20	900	300	1955
F5	23.20	0.0127	0.20	795	290	1795

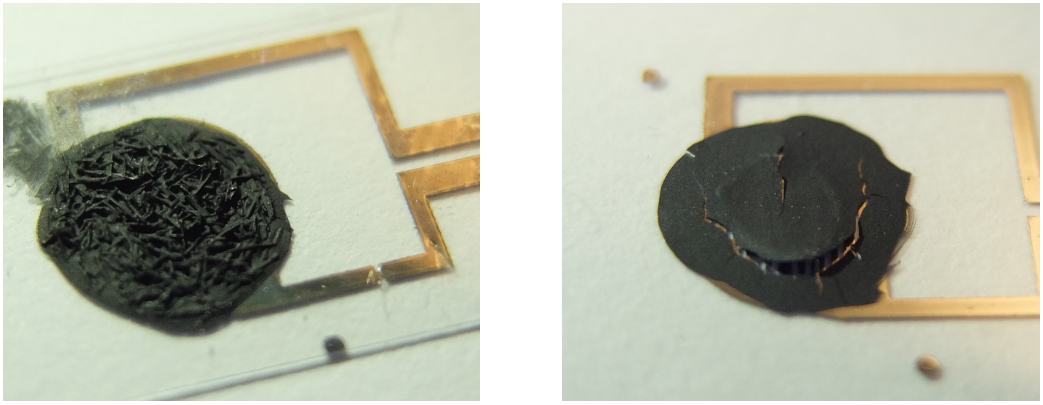

(a) Isotropic - 23.2 Wt% fibres (b) Diluted Electrodag

Figure 5.7: Optical Images of Electrodag-NiMnCuO composite thermistor on PET substrate

5.8. Conclusions

Using an isotropic mixture of Electrodag and NiMnCuO ceramic fibres ($\approx$ 23 wt% of fibres from fibre batch 2) on ink-jet printed silver interdigitate electrodes ($\approx$ 0.13 mm) on PET substrates, resistances can be around 1.9 $M\Omega$ at $25°C$ and 0.3 $M\Omega$ at $85°C$. The B-value $B_{25/85}$ can be as high as 3600 K. These results were obtained when the composites were deposited by simple drop coating. Lower resistances and lower corresponding B-values were obtained when the electrodag was diluted with Isopropyl alcohol, but this made the Electrodag composition unstable. The Electrodag-NiMnCuO composites are promising and can show NTC behaviour, but better control over the thickness of the deposited films need to be exercised to have better results, and more consistent results across the sample population. To do this, stencil printing will be investigated to try to make thinner, more homogenous thin films.

6

Phase 5: Stencil printed flexible thermistor composites

6.1. Stencil Printing

Composite thermistors of NiMnCuO fibre particles in an Electrodag matrix were prepared in the exact same manner as Chapter 5. Fibres (sintered with scheme B) were broken into fibre particles that have an average length of 569 μm in length (with a standard deviation of 288 μm) and an average width of approximately 83 μm. Fibres were mixed with a speed mixer (2500 RPM for 5 minutes) with Electrodag to form an isotropic mix. The inkjet printed silver interdigitate electrodes on polyethylene terephthalate substrate with electrode gap of 0.13 mm was used. A nickel stencil is then placed over the circular electrode design that is 50 μm thick. The design on the stencil is a simple circular cutout of 6 mm diameter that perfectly matches the silver electrode design and has alignment holes. An excess amount of the isotropic mix of Electrodag and NiMnCuO fibre particles is placed on the stencil above the cutout. Using a blade, held at a $45°$ angle, a single pass is made over the cutout, were the composite is deposited onto the electrode. A schematic illustration is shown in figure 6.1. After deposition, the stencil is removed and cleaned and the PET substrate is placed in an oven at $130°C$ for 1 hour to cure the Electrodag composite. Before curing, the deposited layer of Electrodag composite matches the height of the stencil that is 50 μm thick. After curing, the thickness of the Electrodag shrinks to a thickness of 20 μm.

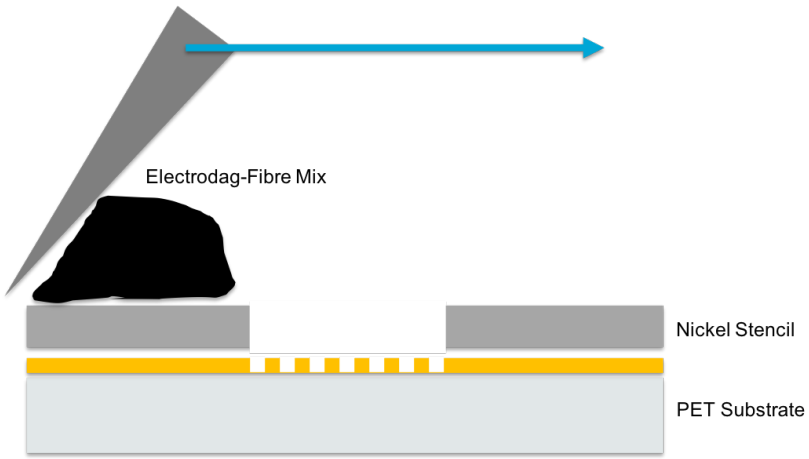

Figure 6.1: Schematic representation of stencil printing thermistor composites

6.2. Results of varying fibre volume content

The amount of fibre particle filler needed to form a percolated network is unknown, therefore a range of specimens were made with 0.0, 1.41, 2.86, 10, 25, 33.33, 50 $wt\%$ of fibre particles. 5 specimens were made for each fibre $wt\%$ and their resistance at $25°C$ and $85°C$ was measured using the experimental setup described in section 5.4. The averaged resistance reading and calculated B-value and temperature coefficient of resistance are presented in table 6.1. Optical microscope images of the stencil printed composites are presented in figure 6.2.

Table 6.1: Resistance Values of Stencil Printed Electrodag-NiMnCuO composites

Batch	Fiber wt%	Fiber vol%	Electrode Gap [mm]	R_{25} [kΩ]	R_{85} [kΩ]	$B_{25/85}$ [K]	α_{25} [% / K]
G	0.00	0.00	0.13	57,760 (SD 11,680)	9,590 (SD 2,500)	3210 (SD 110)	-3.6 (SD 0.1)
H	1.41	0.38	0.13	16,670 (SD 20,000)	2,680 (SD 3,300)	3490 (SD 360)	-3.9 (SD 0.4)
I	2.86	0.77	0.13	3,010 (SD 2,810)	620 (SD 670)	3170 (SD 790)	-3.6 (SD 0.9)
J	10.00	2.86	0.13	280 (SD 70)	45 (SD 15)	3290 (SD 270)	-3.7 (SD 0.3)
K	25.00	8.13	0.13	300 (SD 70)	75 (SD 30)	2540 (SD 260)	-2.9 (SD 0.3)
L	33.33	11.71	0.13	135 (SD 20)	25 (SD 10)	3100 (SD 600)	-3.5 (SD 0.7)
M	50.00	20.97	0.13	140 (SD 20)	20 (SD 5)	3280 (SD 150)	-3.7 (SD 0.2)

The composite resistance at $25°C$ and $85°C$ for composites of varying fibre content is plotted in figure 6.3 to see what the effect of increasing the fibre $wt\%$ has on the resistance of the composite. The corresponding B-value is also plotted against the varying fibre content in figure 6.4. The electrodes used have a gap width of 0.13 mm. As can be seen from the graph of figure 6.3, if the composite has a fibre content below 10 wt%, the average resistance at both $25°C$ and $85°C$ are very high in the $M\Omega$ range with a very high standard deviation. A percolated network is formed with as little as 10 wt% of fibres since the resistance drops to the $k\Omega$ range and only improves marginally with a further increase in fibre content. This is considerably good thermistor performance at a low fibre content, where $R_{25} = 280\ k\Omega$, $R_{85} = 45\ k\Omega$, and the sensitivity is high with a B-value = 3290 K and $\alpha_{25} = -3.7\ \%/K$.

To make the results more comparable to other composite thermistor systems, the fibre weight percentage can be converted to a volume percentage. Directly measuring the density of the fibres with the archimedes principle was difficult due to the sintered fibres' small size and brittleness. Instead, we must assume that the fibres are close to the same density as the pellets of the same composition at 4.79 g/mL which is $93.1\ \%$ relative density (compared to the max theoretical density of 5.14 g/mL). We can then re-plot the composite resistance at $25°C$ and $85°C$ for composites of varying fibre volume content, plotted in figure 6.5. Hence, a percolated network is formed with as low as $2.86\ vol\%$ (10 $wt\%$)

The length of the fibre particles in the Electrodag composites were investigated using an optical microscope (Keyence, VHX 2000, Osaka, Japan). Using image processing software (ImageJ) the average fibre length was calculated. The variation in length can be quite large, but the average fibre length is a bit smaller with composites that have higher fibre content. This seems logical as the brittle fibre particles are more likely to collide and break into smaller pieces in the uncured Electrodag with

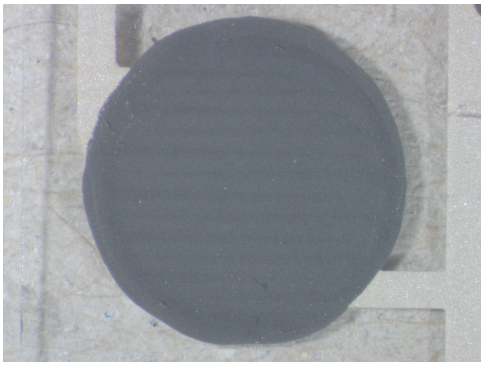

(a) Batch G - 0.0 fibre wt% - 0.0 fibre vol%

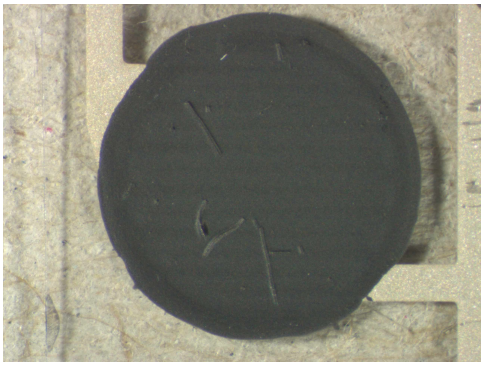

(b) Batch H - 1.41 fibre wt% - ≈ 0.38 fibre vol%

(c) Batch I - 2.86 fibre wt% - ≈ 0.77 fibre vol%

(d) Batch J - 10.00 fibre wt% - ≈ 2.86 fibre vol%

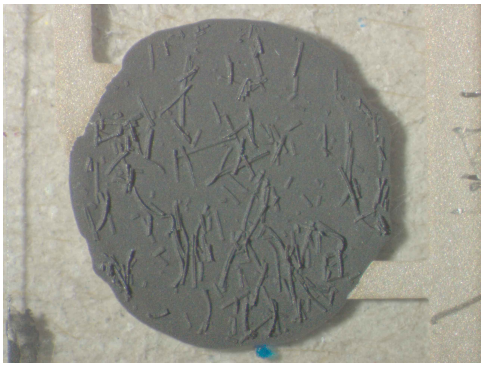

(e) Batch K - 25.00 fibre wt% - ≈ 8.13 fibre vol%

(f) Batch L - 33.33 fibre wt% - ≈ 11.71 fibre vol%

(g) Batch M - 50.00 fibre wt% - ≈ 20.97 fibre vol%

Figure 6.2: Optical Images of Stencil Printed Electrodag-NiMnCuO composite thermistor on PET substrate

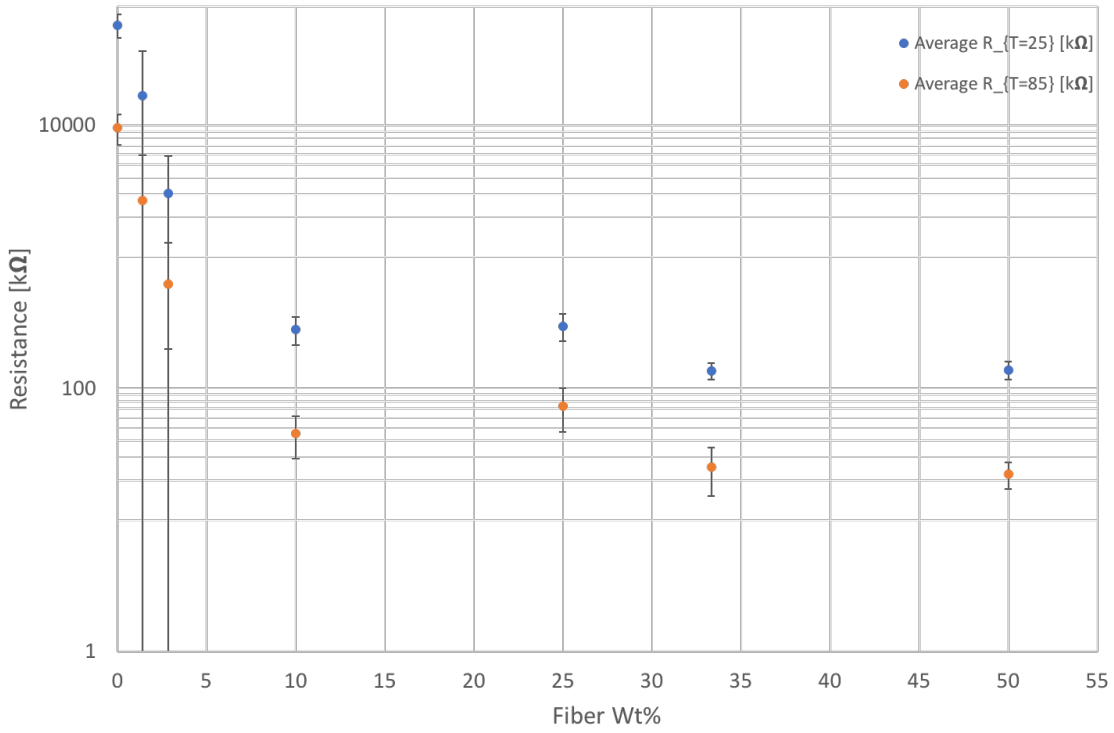

Figure 6.3: Composite resistance at $25^{\circ}C$ and $85^{\circ}C$ for varying fibre content by $wt\%$

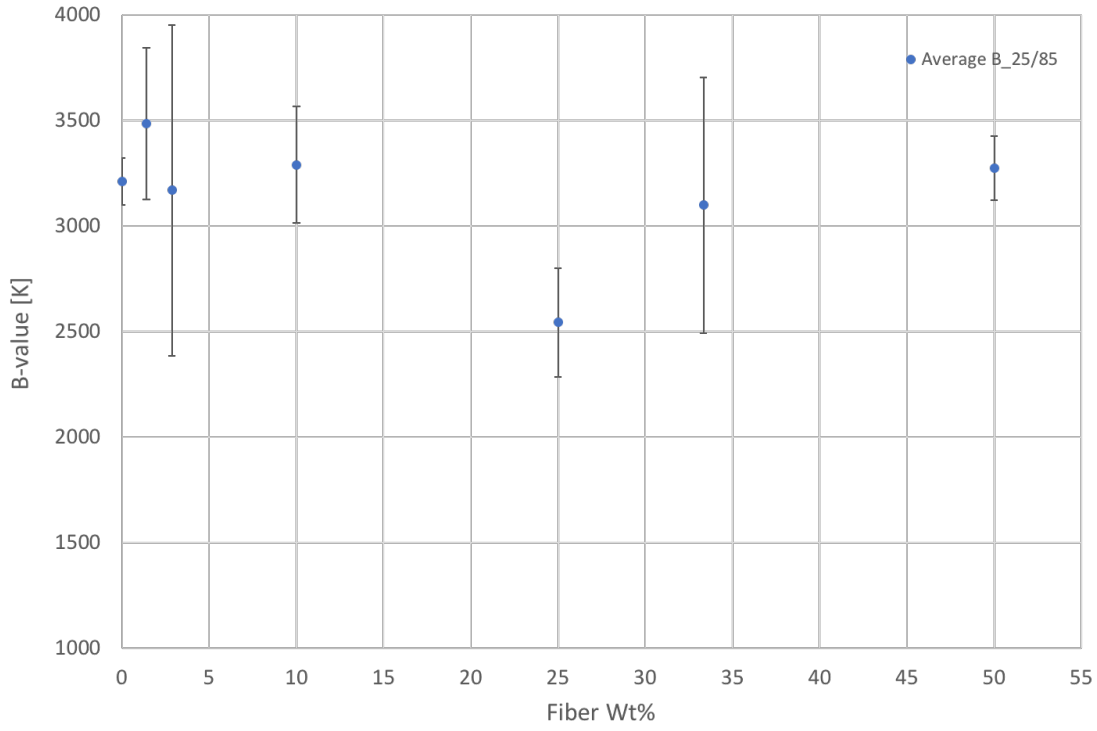

Figure 6.4: Composite B-value for varying fibre content by $wt\%$

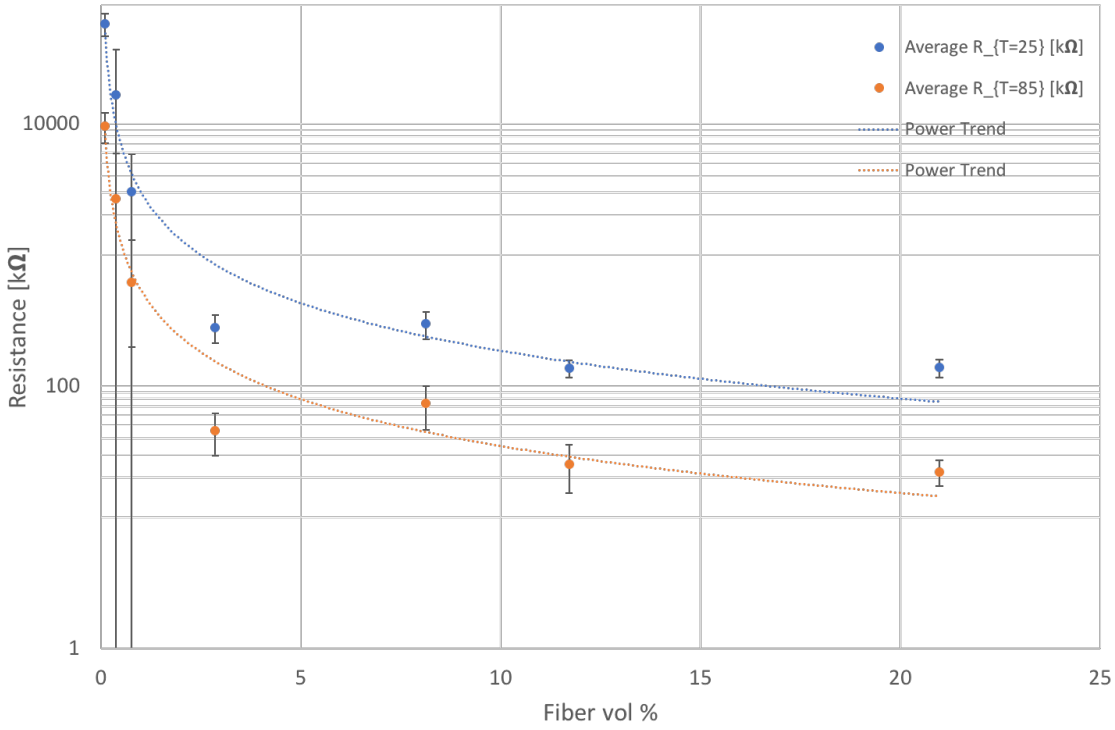

Figure 6.5: Composite resistance at $25°C$ and $85°C$ for varying fibre content by $vol\%$. Trend lines are for guidance only

higher fibre content. Especially when mixed in the speed mixer and when stencil printing where the isotropic mix flows along the stencil when being blade coated onto the electrodes. Composites with 10 wt% had an average fibre length of 477 μm with a standard deviation of 333 μm. Fibres can be as short as 66 μm and as long as 1645 μm in length. Composites with 50 wt% had an average fibre length of 301 μm with a standard deviation of 137 μm. Fibres can be as short as 51 μm and as long as 662 μm in length.

6.3. Results of increasing IDE gap width

If the electrode gap is increased from 0.13 mm to 0.20 mm, the sensitivity between $25°C$ and $85°C$ could be larger at the cost of higher resistances, despite using the same amount of fibre content. This can be achieved by having a proportionally higher increase of resistance at $25°C$ than $85°C$. It will be reflected in the measured B-value of $B_{25/85}$. Specimens were made with 0.0, 10, 25, 33.33, 50 $wt\%$ of fibre particles on interdigitate electrodes with a gap size of 0.20 mm. 5 specimens were made for each fibre $wt\%$ and their resistance at $25°C$ and $85°C$ was measured. The averaged resistance reading, B-value and temperature coefficient of resistance are presented in table 6.2. A comparison of the resistance obtained at $25°C$ and $85°C$ for varying fibre content by $wt\%$ and larger electrode size is presented in figure 6.6. A comparison of the B-value is given in figure 6.7.

Evident from figure 6.6 is that the resistance for a larger gap size, increased. This is logical. The B-value ($B_{25/85}$) also increased which means that for temperature sensing between $25°C$ and $85°C$, there is a larger decrease of resistance per change in degree of temperature. So the sensitivity of the composite thermistor is higher, at the cost of being a more resistive thermistor overall. With 10 $wt\%$ of fibre content, if an electrode gap size of 0.13 mm is used, the composite thermistor has a resistance $R_{25} = 280\ k\Omega$, a $R_{85} = 45\ k\Omega$, a B-value = 3290 K and an $\alpha_{25} = -3.7\ \%/K$. If an electrode gap size of 0.20 mm is used, the composite thermistor has a resistance $R_{25} = 830\ k\Omega$, a $R_{85} = 100\ k\Omega$, a B-value = 3810 K and an $\alpha_{25} = -4.3\ \%/K$. This shows that the overall composite resistance and sensitivity can be tailored and customised by changing the gap width of the interdigitate electrodes.

Table 6.2: Resistance Values of Stencil Printed Electrodag-NiMnCuO composites with larger electrode gap

Batch	Fiber wt%	Fiber vol%	Electrode Gap [mm]	R_{25} [kΩ]	R_{85} [kΩ]	$B_{25/85}$ [K]	α_{25} [% / K]
N	0.00	0.00	0.20	112,220 (SD 6,220)	19,120 (SD 3,290)	3170 (SD 220)	-3.6 (SD 0.3)
O	10.00	2.86	0.20	830 (SD 210)	100 (SD 30)	3810 (SD 460)	-4.3 (SD 0.5)
P	25.00	8.13	0.20	400 (SD 70)	48 (SD 7)	3800 (SD 50)	-4.3 (SD 0.06)
Q	33.33	11.71	0.20	360 (SD 100)	44 (SD 13)	3740 (SD 70)	-4.2 (SD 0.08)
R	50.00	20.97	0.20	350 (SD 140)	42 (SD 15)	3770 (SD 60)	-4.2 (SD 0.06)

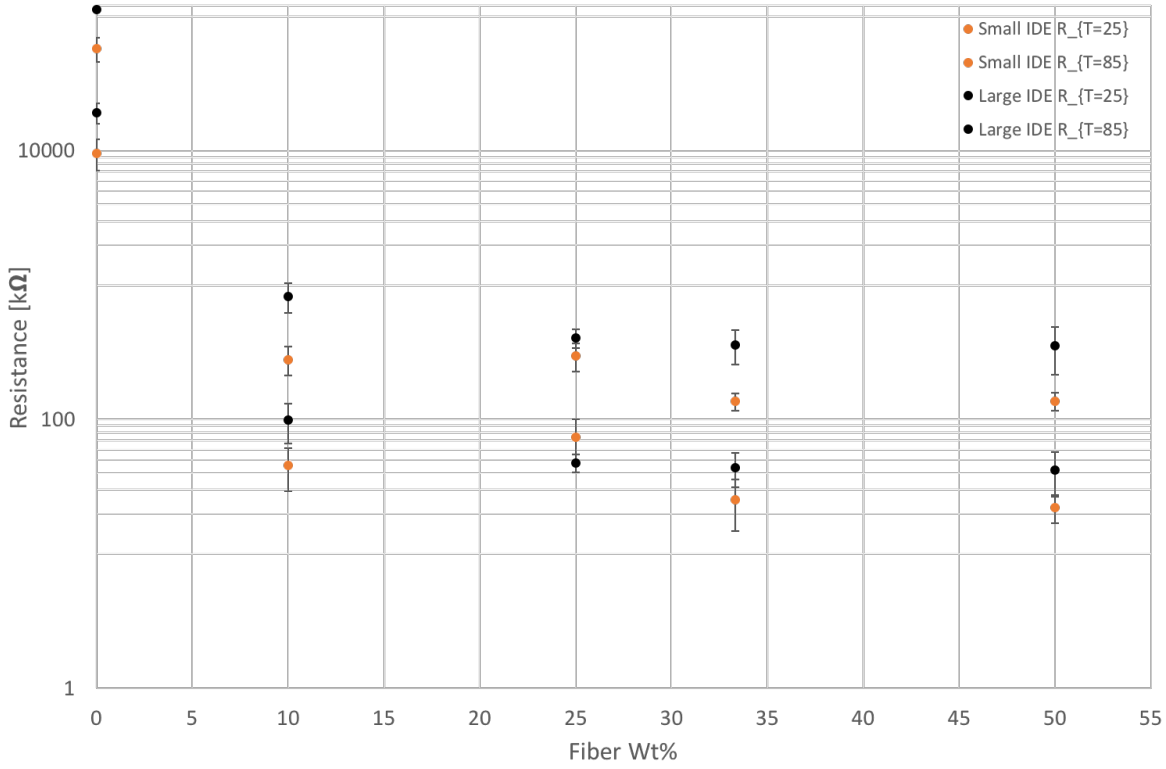

Figure 6.6: Comparison of effect of larger electrode gap on composite resistance at $25^{\circ}C$ and $85^{\circ}C$ for varying fibre content by $wt\%$

6.4. Bending tests

The design of the composite thermistors was intended to enable mechanical flexibility and so their flexibility was evaluated by bending tests. A flexible sensor needs to be able to mechanically survive bending (and not chip-off), and still be useful for temperature sensing. For this, the thermistor performance (i.e. the resistance at a particular temperature) needs to remain unchanged, or change in a predicable manner that can be corrected for. Therefore, cyclic bending tests were performed on the composite thermistors and their resistance at room temperature ($19.8^{\circ}C$) was compared, before and after bending.

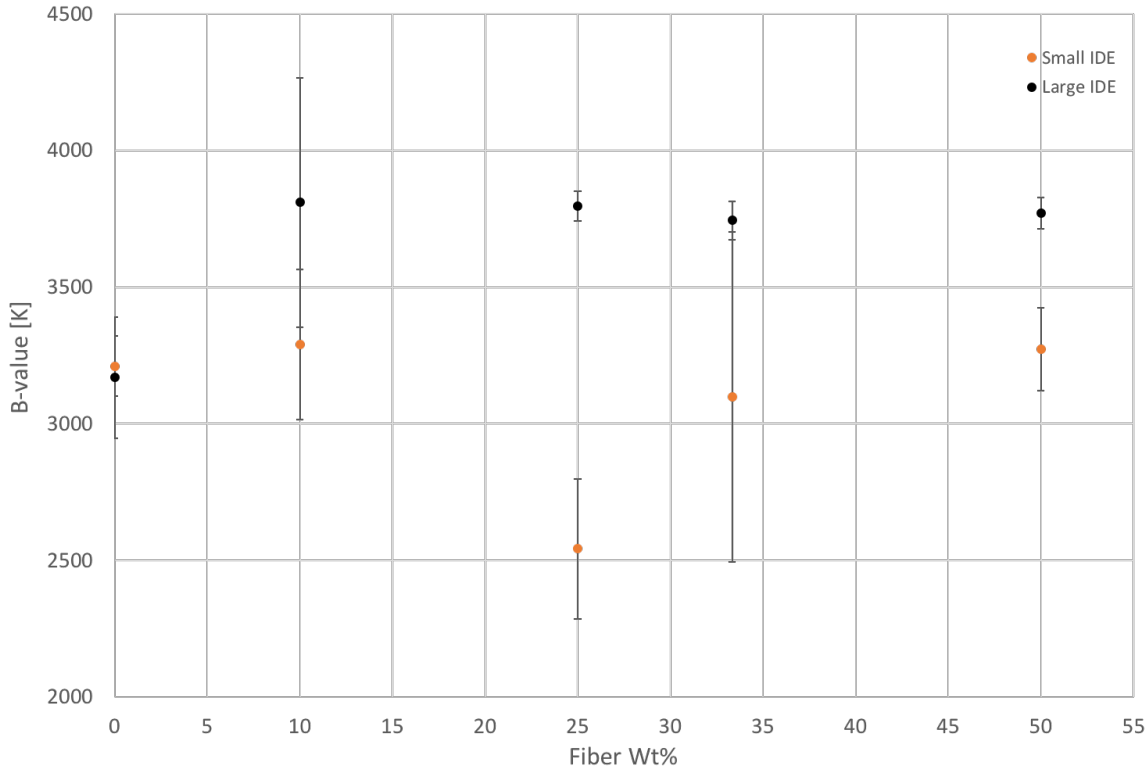

Figure 6.7: Comparison of effect of larger electrode gap on composite B-value for varying fibre content by $wt\%$

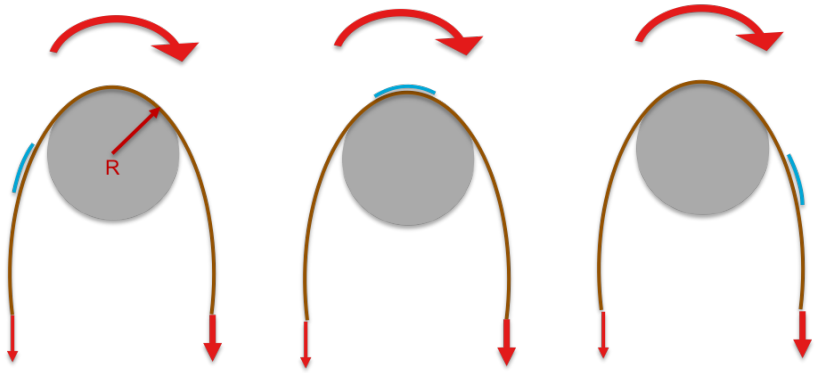

Figure 6.8: Schematic of cyclic tensile bending method

Composite thermistor samples of varying fibre content (0, 1.41, 10, 25, 50 $wt\%$) with the smaller electrode gap (0.13 mm) were bent to a 10 mm radius 100 times, followed by 5 mm radius 100 times, followed by a 2.5 mm radius 100 times. A bend radius of 10 mm correlates to a strain of approximately 0.621%, a 5 mm radius correlated to 1.23%, and a 2.5 mm radius correlates to a 2.44% strain. The resistance at room temperature ($19.8°C$) was measured after 0, 2, 5, 10, 20, 50, 100 bends. The method in which the samples were bent is shown schematically in figure 6.8. The bottom of the PET substrates were attached onto the sticky side of a piece of tape and slide over a metal rod of 10 mm radius. This is performed in a slow and controlled manner. Very little force is applied on both ends of the tape to avoid stretching, but to ensure that the composite thermistor on the PET substrate conforms to the circumference of the metal rod to have a bending radius equal to the radius of the metal rod. After 0,

2, 5, 10, 20, 50, and 100 bends with a 10 mm bending radius, the composite thermistor is removed from the tape and its resistance is measured. The results of 0, 1.41, 10, 25, and 50 $wt\%$ are all shown in appendix D, but 1.41, 10, 25, and 50 $wt\%$ all look very similar to the results of 50 $wt\%$ shown in figure 6.9. A control curve is include where the sample was measured 7 times at room temperature consecutively without bending, to show that the resistance is constant.

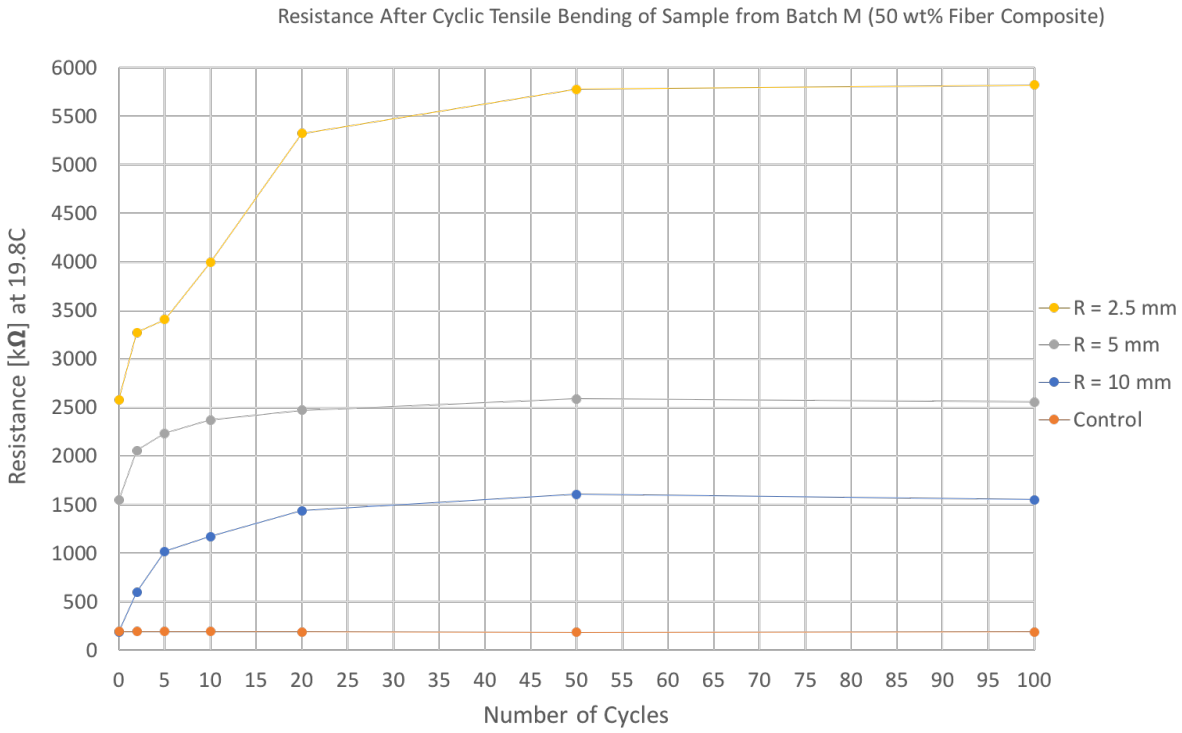

Figure 6.9: Resistance after cyclic tensile bending of thermistor composite with 50 $wt\%$ of fibres

When bent to a radius of 10 mm, the composite with 50 $wt\%$ would increase dramatically by a factor of 8 after 20 bends. However, between 20 and 100 bends, the resistance doesn't change very dramatically. This suggests that the fibres break and a new conductive path is formed in the first 20 bends. After 20 bends, the resistance change stabilises as the fibres no longer break and can survive being bent to 10 mm radius (at least for 100 bends). With a bending radius of 5 mm and 2.5 mm this behaviour is also evident, where the resistance change stabilises at a higher resistance.

The results of bending pure Electrodag were very different because it proved to be very sensitive to bending. Its bending results are shown in figure 6.10. Between 5-20 bends at 10 mm bending radius the resistance exceeds the 120 $M\Omega$ maximum resistance that the multimeter can measure.

A comparison of the relative resistance change (R/R0) over 100 bends at 10 mm radius is given in figure 6.11. With the exception of pure electrodag, it is logical that the results show that the relative change in resistance due to bending is lower for composites with lower fibre content.

In terms of survivability, after 300 bends (100 at 10 mm bending radius, 100 at 5 mm bending radius, 100 at 2.5 mm bending radius) the resulting thermistor composites are shown in figure 6.12. The composite thermistors with 0, 1.41, and 10 $wt\%$ of fibre content survived 300 bends without any observable, aesthetic damage. With higher fibre content (25 $wt\%$ and 50 $wt\%$) some chip-off occurred.

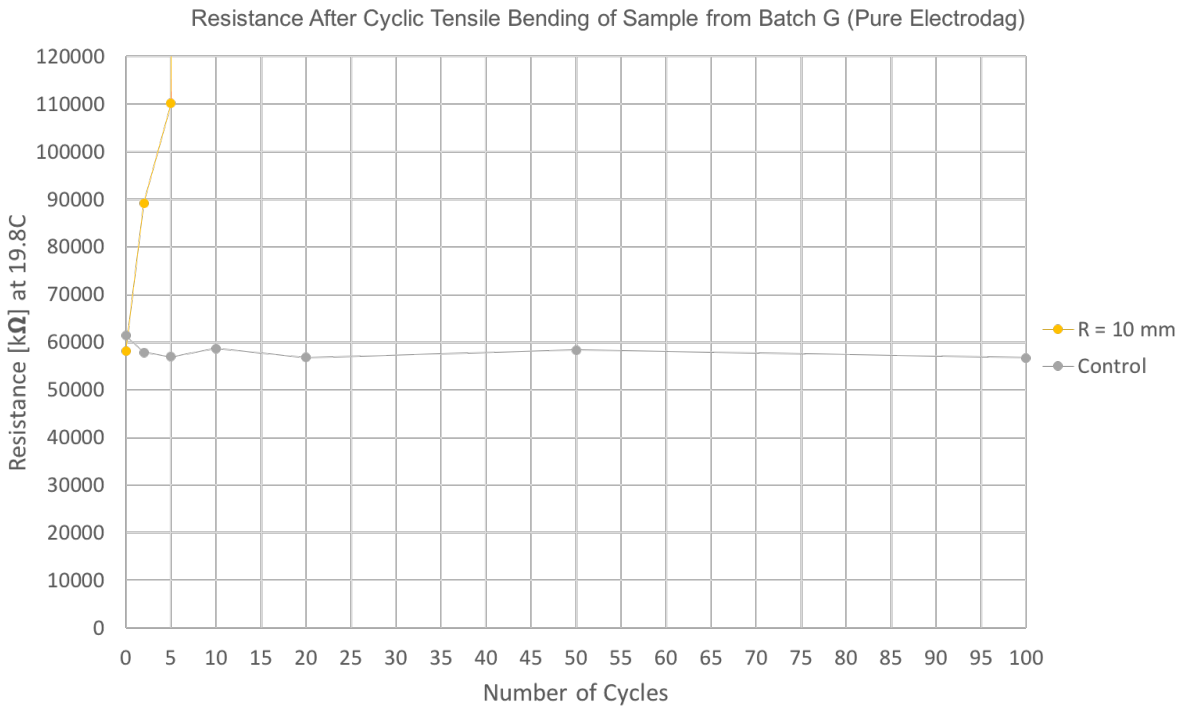

Figure 6.10: Resistance after cyclic tensile bending of pure electrodag

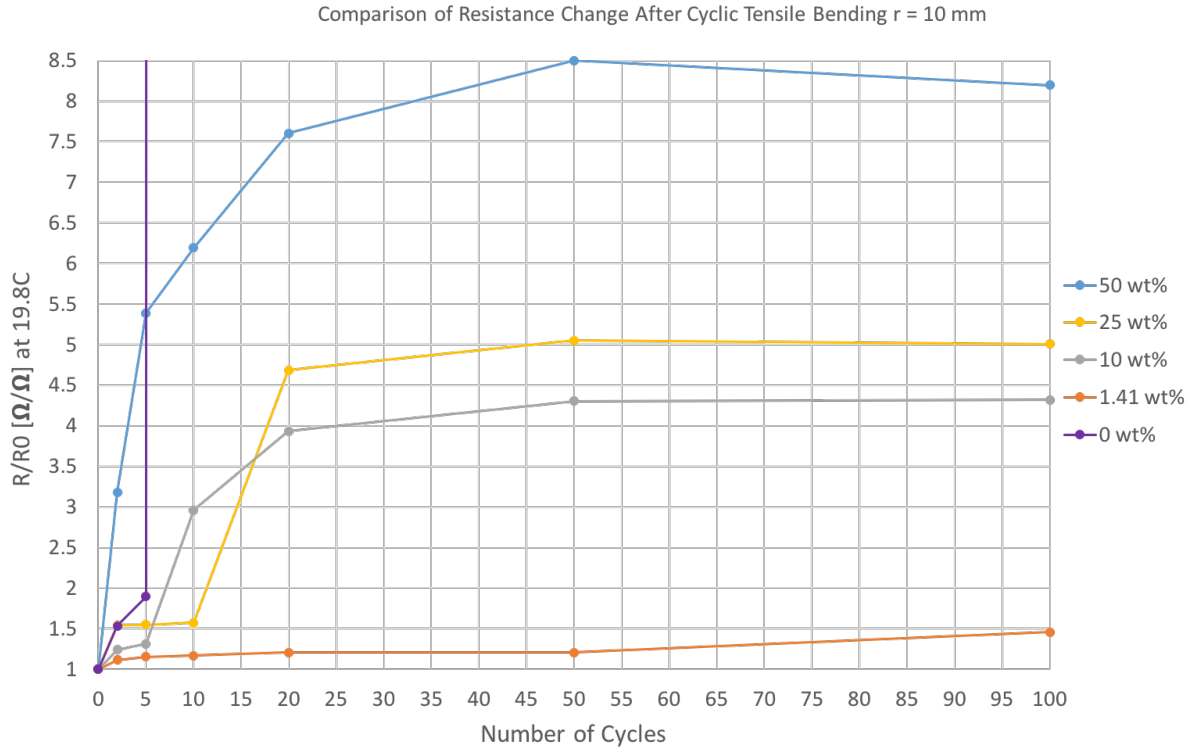

Figure 6.11: Comparison of relative resistance change over 100 bends at 10 mm radius

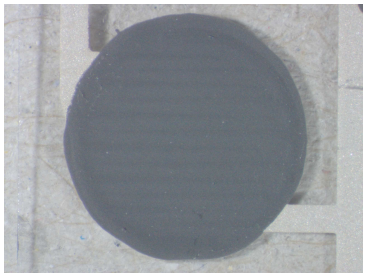

(a) Batch G - 0 fibre wt% - Before

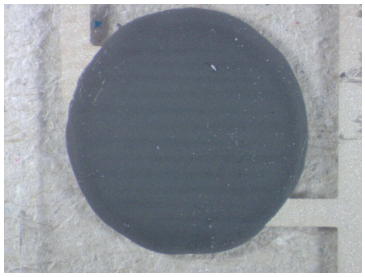

(b) Batch G - 0 fibre wt% - After

(c) Batch H - 1.41 fibre wt% - Before

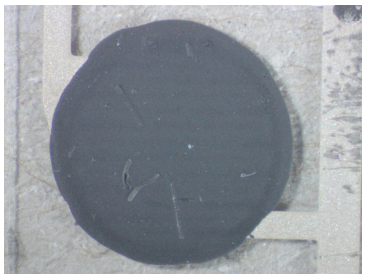

(d) Batch H - 1.41 fibre wt% - After

(e) Batch J - 10 fibre wt% - Before

(f) Batch J - 10 fibre wt% - After

(g) Batch K - 25 fibre wt% - Before

(h) Batch K - 25 fibre wt% - After

(i) Batch M - 50 fibre wt% - Before

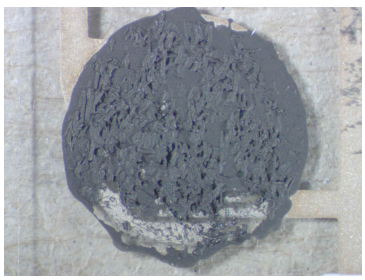

(j) Batch M - 50 fibre wt% - After

Figure 6.12: Optical Images of Stencil Printed Composite thermistor Before and After 300 Bend Cycles

7

Discussion

7.1. Introduction

From the results of chapter 6, flexible composite thermistors have been produced that can perform as thermistors. Their thermistor performance and mechanical flexibility depend on the fibre particle content of the NTC ceramic fibres.

The functional granular composites form a percolated network with as little as 10 $wt\%$ of filler particles. With interdigitate electrodes of a gap width of 0.13 mm, the resistance $R_{25} = 280\ k\Omega$, $R_{85} = 45\ k\Omega$, the B-value = 3290 K. If the fibre content is increased the composite can have lower resistance and higher sensitivity, but marginally so. At the extreme of 50 $wt\%$ of filler particles the resistance $R_{25} = 140\ k\Omega$, $R_{85} = 20\ k\Omega$, the B-value = 3280 K. Thus, a 5 fold increase in filler particles yields a 2 fold decrease in resistance. However, at such a high fibre content its ability to be bent is much lower. The relative resistance increases by a factor of 8.5 after 100 bend cycles at a bend radius of 10 mm ($\varepsilon \approx 0.621\%$). After 300 cycles (100 cycles with bending radius 10mm ($\varepsilon \approx 0.621\%$), 100 cycles with bending radius 5 mm ($\varepsilon \approx 1.23\%$), 100 cycles with bending radius 2.5 mm ($\varepsilon \approx 2.44\%$) the composite with 50 $wt\%$ of filler particles has some chip-off from the PET substrate. While at 10 $wt\%$ of filler particles, the composite thermistor can survive 300 bend without any chip-off. The relative resistance increases by a factor of 4.5 after 100 bend cycles at a bend radius of 10 mm ($\varepsilon \approx 0.621\%$). Hence, with increasing fibre content the resistance decreases, but so does its ability to mechanically bend. Overall, the composites with 10 $wt\%$ of filler particle is the best all around thermistor with good thermistor performance and good mechanical flexibility.

7.2. Comparison of Electrical Properties of NTC Composites

To compare the thermistor performance of the composite, the dimensionless value of resistivity is a better, more objective metric. However, with the design of the composite thermistor with its interdigitate electrode gaps, the design makes it difficult to identify the exact cross sectional area of the conductive path needed to convert the measured resistance to resistivity $\rho = \frac{R \cdot A}{L}[\Omega \cdot cm]$. We can give a rough estimate by measuring the equivalent length of the interdigitate electrode, as shown in figure 7.1. This gives an electrode length of 51.657 mm. The height of the conductive cross-sectional area is tricky, the cured Electrodag is 0.020 mm thick, while the fibres have a flat noodle shape, as seen in figure 4.8, with an average width of about 0.083 mm determined from SEM images in section 4.3.3. If we take the conservative approach and estimate that the height of the conductive area is the same as the fibre width, as seen in figure 7.2, we can calculate the cross-sectional area A needed to determine the resistivity. L is the gap width of the electrodes which were 0.13 mm. Therefore, the resistance values (at $25°C$) for the stencil printed thermistor composites given in table 6.1 can be converted into an approximate resistivity, given in table 7.1.

For pellets of $\mathrm{Mn_{2.4}\,Ni_{0.5}\,Cu_{0.1}\,O_4}$ produced with binder and sintered at $1250°C$ for 2.5 hours, the resistivity at $25°C$ obtained was $\rho_{25} = 720\ \Omega cm$ with a standard deviation of 180 Ωcm. The B-value obtained was $B_{25/85} = 3630$ K with a standard deviation of 30 K. When compared to the composites

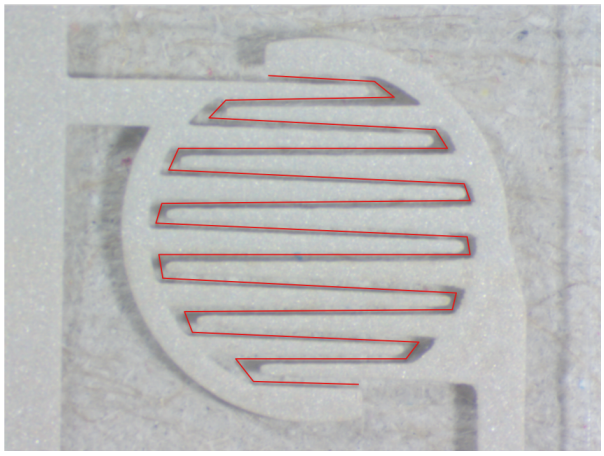

Figure 7.1: Estimated Length of Interdigitate Electrodes with 0.13 mm gap size

(a) Side View (b) Front View

Figure 7.2: Schematic of cross section of electrode gap

Table 7.1: Resistivity Values of Stencil Printed Electrodag-NiMnCuO composites

Batch	Fiber wt%	Fiber vol%	Electrode Gap [mm]	R_{25} [kΩ]	R_{85} [kΩ]	$B_{25/85}$ [K]	α_{25} [% / K]	ρ_{25} [kΩ·cm]
G	0.00	0.00	0.13	57,760 (SD 11,680)	9,590 (SD 2,500)	3210 (SD 110)	-3.6 (SD 0.1)	190,490 (SD 38,530)
H	1.41	0.38	0.13	16,670 (SD 20,000)	2,680 (SD 3,300)	3490 (SD 360)	-3.9 (SD 0.4)	54,970 (SD 65,960)
I	2.86	0.77	0.13	3,010 (SD 2,810)	620 (SD 670)	3170 (SD 790)	-3.6 (SD 0.9)	9,930 (SD 9,280)
J	10.00	2.86	0.13	280 (SD 70)	45 (SD 15)	3290 (SD 270)	-3.7 (SD 0.3)	920 (SD 220)
K	25.00	8.13	0.13	300 (SD 70)	75 (SD 30)	2540 (SD 260)	-2.9 (SD 0.3)	980 (SD 230)
L	33.33	11.71	0.13	135 (SD 20)	25 (SD 10)	3100 (SD 600)	-3.5 (SD 0.7)	450 (SD 70)
M	50.00	20.97	0.13	140 (SD 20)	20 (SD 5)	3280 (SD 150)	-3.7 (SD 0.2)	455 (SD 70)

of 10 $wt\%$ fibre particles, the B-value is not too much lower where $B_{25/85} = 3290$ K with a standard deviation of 270 K. However, the estimated resistivity is much higher where, $\rho_{25} = 920 \cdot 10^3\ \Omega cm$ with a standard deviation of $220 \cdot 10^3\ \Omega cm$. This is logically orders of magnitude higher because most of the composite (90 $wt\%$) is the very resistive Electrodag. A more useful comparison is to compare the resistivity to other flexible composite thermistors in Literature.

Looking at the summary of flexible temperature sensors found in recent Literature presented in tables A.1 and A.2 in appendix A. Researchers trying to develop flexible temperature sensors generally follow two trends:

1. Use conventional thermistor material → Develop new architecture to allow flexibility
2. Use new unconventional, intrinsically flexible thermistor material → Improve thermistor performance

Unfortunately, in recent Literature there are not many studies that follow the first trend and attempt to use functional granular composites to achieve flexible thermistors. Deutz [13] made functional granular composites of NiMnO particles in an epoxy matrix. However, for the best electrical performance it required using agglomerated particles of NiMnO at high filler volume of NTC particles (up to $\Phi_c = 50\%$) where the composite had a resistivity on the order of $10^5\ \Omega cm$ and a B-value of about 1500 K. The results are conveniently summarised in figures 1.10a and 1.10b, but are presented again in figure 7.3 for the convenience of the reader. The NiMnO-Epoxy system, needed a filler volume content above 35% to create a percolated network. This thesis work was able to achieve a percolated network with as little as 10 $wt\%$, equivalent to about 2.86 vol%. For composites of 10 $wt\%$ fibre particles, $\rho_{25} = 920 \cdot 10^3\ \Omega cm$ with a standard deviation of $220 \cdot 10^3\ \Omega cm$. This is a lower resistivity by almost 2 orders of magnitude. The B-value from the composite thermistor was 3290 K, a factor of 2 higher than the NiMnO-Epoxy system.

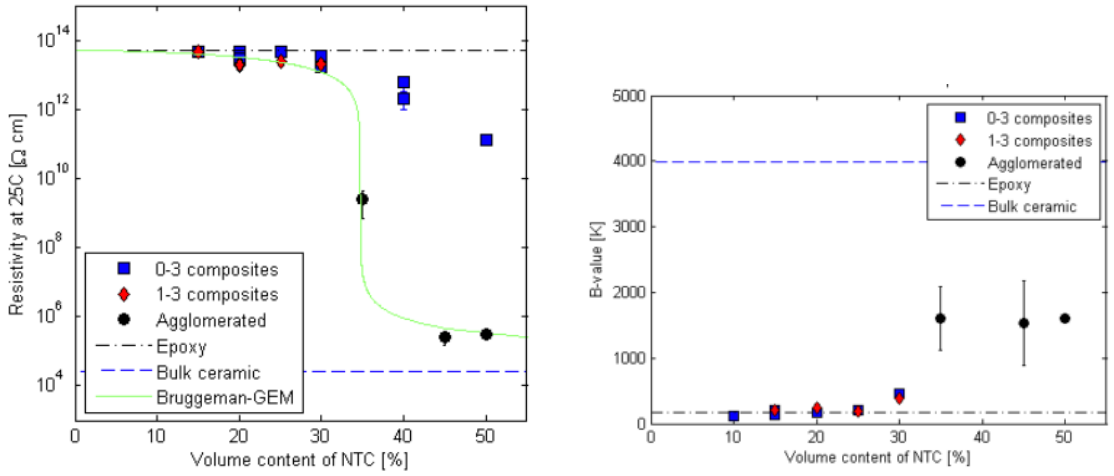

(a) Resistivity vs Filler Volume Content

(b) B-value vs Filler Volume Content

Figure 7.3: Resistivity and B-value vs filler volume content of NiMnO particles in NiMnO-Epoxy composites [13]

Another impressive system in Literature is from Khan et al. [23] who used NiO nanoparticles mixed with polystyrene-butadiene rubber (PSBR) binder that was stencil printed onto gold electrodes onto a kapton polyimide substrate. The B-value reported was 4330 K. The resistivity wasn't clearly reported but they use an electrode gap of $80\mu m$ and a composite thermistor that is 2mm in length and width, with a thickness of $40\mu m$. This translates to a $\rho_{30} = 35 \cdot 10^3\ \Omega cm$. Moreover, the bending performance is very impressive since the resistance at room temperature changed by 0% after 100 bends at a radius of 10 cm, followed by 0.5% after 100 bends at a radius of 5 cm, followed by 4% after 100 bends at a radius of 2.5 cm. The thermistor was encapsulated to protect it from moisture and other processing steps with poly(methyl methacrylate) and later with Cytop. The sensitivity range of the thermistor is from $32 - 37°C$. Now the B-value and ρ_{30} are more impressive, but the entire system is only applicable for a very narrow operating temperature range. By contrast the Electrodag-NiMnCuO composite thermistors can be used through the $25 - 85°C$ range while delivering a B-value $B_{25/85} = 3290$ K and a resistivity of $\rho_{25} \approx 920 \cdot 10^3\ \Omega cm$. Furthermore, while the change in resistance seems more drastic to bending tests, it is worth noting that the composites were bent to a much smaller bending radius of 2.5 mm without any protective encapsulating layer, while the NiO-PSBR composites were only bent to

a minimum bending radius of 2.5 cm and were encapsulated.

If the Electrodag-NiMnCuO functional granular composites are compared to a thin-film system like the one from Huang et al. [21]. The thermistor performance is still very decent while providing better mechanical flexibility. Huang et al. [21] ink-jet printed thin films of NiO onto polyimide films that had silver electrodes. The system has a good operating range (room temperature to $200°C$), with a very high sensitivity (B-value ≈ 4300K). The variation in resistance from bending is very small with a $\Delta R/R < 10\%$, but this study measures resistance in bending, as opposed to after bending. Furthermore, specimens were only subjected to a single bend and the bending radii were large (7 to 1 cm). At a lower bending radius of 0.5 cm, the NiO film chipped-off completely from the polyimide substrate. Therefore in comparison to this system, the Electrodag-NiMnCuO functional granular composites have demonstrated the ability to survive smaller bends and larger amount of bend cycles.

If the Electrodag-NiMnCuO composites are compared to systems that followed trend 2: using new unconventional, intrinsically flexible thermistor material. The Electrodag-NiMnCuO delivers superior thermistor performance, but lower mechanical flexibility. Yan et al. [59] used crumpled graphene in a serpentine shape, embedded in a PDMS matrix. The system was a huge advancement in being stretchable up to 50% strain, but its temperature sensing properties are fairly low. When not stretched, the B-value was 847 K. Stretching increased the B-value to a maximum of 1712 K at a strain of 50%. Hence in comparison to this system, the Electrodag-NiMnCuO composites cannot be subjected to the same amount of strain, but it delivers much better temperature sensing performance.

Overall, when comparing the Electrodag-NiMnCuO composites to the other flexible temperature sensors found in recent Literature presented in tables A.1 and A.2 in appendix A. For systems that use conventional thermistor material with new device architectures to provide flexibility, our design has more impressive bending while having good thermistor performance. For systems that use non-conventional, intrinsically flexible thermistor materials, our design has better temperature sensing performance while still having good bending performance.

8

General Conclusions

The objective of the thesis was to suggest a design for a mechanically flexible temperature sensor by designing a thermistor using functional granular composites that can have good thermistor performance (high sensitivity: B-value > 3000 K, and low resistivity: $\rho \approx 10^1 - 10^2\ \Omega cm$) while being mechanically flexible (surviving bending radii ≤ 1 cm over 100 cycles). To achieve this objective this thesis work was organised into 5 major phases with the intention to create the first fully flexible temperature sensor that can perform on par with conventional thermistors that can be immediately adopted into industry.

Due to its high commercial value, no reference NTC ceramic composition with its exact processing conditions are available in Literature that produce a thermistor with commercially desirable properties (i.e. high sensitivity over a large temperature range, with high thermal stability and low resistance drift). Phase 1 was therefore to select a NTC ceramic composition and Phase 2 was to investigate the necessary processing conditions to be able to produce bulk ceramics with adequate temperature sensing performance, before modifying the processing conditions to make NTC ceramic fibres in Phase 3. Phase 4 involved the selection of an appropriate polymer matrix and to attempt to create thermistor composites. Phase 5 involved creating more optimal composite thermistors using a more controlled and reproducible method and to test its thermistor and bending performance.

In phase one, the ceramic composition chosen stuck to a maximum of 3 elements to simplify the manufacturing process, to limit the risk of irregularities, and to ensure the reproducibility of the results. The criteria for composition selection prioritised low resistivity over higher sensitivity (B-value and α). A composition of $\mathrm{Cu_{0.3}Ni_{0.5}Mn_{2.2}O_4}$ was chosen where a resistivity on the order of $\rho_{25} \approx 12.6\ \Omega cm$ and a B-value on the order of $B_{25/50} \approx 2960$ K is expected.

In phase two, ceramic pellets were created to investigate the best processing conditions and to characterise the bulk ceramic's thermistor properties. The electrical performance of the pellets was very sensitive to how the un-sintered pellets were handled and pressed. Towards this, a binder is helpful and handling smaller amounts and geometries ensures better density and less cracks and defects. With higher copper content, higher density pellets are obtainable with lower resistivity, but also with low sensitivity (B-value and α). The resistivity is very low that resistance drift plays a larger role. A lower copper content was selected (Cu 0.1) because it delivers a higher B-value and α, close to those delivered by a copper content of 0.05, but with a lower trade-off in increased resistivity. With our in-house manufacturing route a more suitable composition of $\mathrm{Mn_{2.4}\,Ni_{0.5}\,Cu_{0.1}\,O_4}$ was selected with a sintering scheme of $1250°C$ for 2.5 hours with a ramp of $180°C/hr$ that should give a relative density of 91-93%, a $\rho_{25} \approx 720\ \Omega cm$, a $\rho_{85} \approx 90\ \Omega cm$, a $B_{25/85} \approx 3600$ K, and a $\alpha_{25} \approx -4.1\ \%/K$.

In phase three, ceramic NTC fibres of $\mathrm{Mn_{2.4}\,Ni_{0.5}\,Cu_{0.1}\,O_4}$ were produced via fibre spinning and were sintered at 3 different schemes. Using SEM images to observe the densification of the fibres, scheme B ($1250°C$ for 6 hours at $180°C/hr$) and scheme C ($1250°C$ for 6 hours at $300°C/hr$) produced equally dense fibres. Their exact density could not be measured with the archimedes principle, due to the small and brittle nature of the sintered fibres. XRD analysis confirms that the ceramic fibres are

monophase and SEM images confirm the fibres are not hollow, but solid flat noodle shaped fibres. The average fibre width was about 83 μm, but this is determined more by the fibre spinning process rather than sintering scheme (i.e. spinneret hole size and stretching ratio).

In phase 4, functional granular composites are drop coated as thin films onto PET substrates with silver electrodes. PDMS-NiMnCuO composites are made, but the polymer's coefficient of thermal expansion was too high so the overall composite displayed a non-linear PTC effect. The PDMS had high wettability so quasi 3-3 composites could not be made, instead producing 0-3 composites, where the high tunnelling resistivity dominates. BCB-NiMnCuO composites were also made, but the low viscosity polymer was not appropriate from a processing viewpoint. Electrodag-NiMnCuO composites were made and showed promising NTC behaviour, but better control over the thickness of the Electrodag deposition was required to obtain better performance.

In phase 5, stencil printed Electrodag-NiMnCuO composites were produced with varying amounts of fibre particle content. A percolated network is formed with as little as 10 wt% of fibres (≈ 2.86 vol%). The composite with 10 wt% of fibres has good thermistor performance at a low fibre content, where $R_{25} = 280\ k\Omega$, $R_{85} = 45\ k\Omega$, and the sensitivity is high with a B-value = 3290 K and $\alpha_{25} = -3.7\ \%/K$. If the interdigitate electrode gap size is increased from 0.13 mm to 0.20 mm, the composite with 10 wt% has a $R_{25} = 830\ k\Omega$, a $R_{85} = 100\ k\Omega$, a B-value = 3810 K and an $\alpha_{25} = -4.3\ \%/K$. Hence, the overall composite resistance and sensitivity can be tailored and customised by changing the gap width of the interdigitate electrodes. The composite with 10 wt% and a electrode gap of 0.13 mm can survive 300 bends cycles (100 cycles with bending radius 10 mm ($\varepsilon \approx 0.621\%$), 100 cycles with bending radius 5 mm ($\varepsilon \approx 1.23\%$), 100 cycles with bending radius 2.5 mm ($\varepsilon \approx 2.44\%$) without any observable, aesthetic damage. However, the relative resistance (R/R0) increases with bending, but after 20 bend cycles it appears to stabilise for every bending radius. The estimated resistivity of the composite with 10 wt% of fibres at $25°C$ is $\rho_{25} = 920 \cdot 10^3\ \Omega cm$ with a standard deviation of $220 \cdot 10^3\ \Omega cm$. This is logically orders of magnitude higher because most of the composite (90 $wt\%$) is the very resistive Electrodag. Compared to other flexible temperature sensors in recent Literature, its' thermistor performance is very impressive for the amount of mechanical flexibility it can display. For systems that use conventional thermistor material with new device architectures to provide flexibility, our design has superior bending performance while having good thermistor performance. For systems that use non-conventional, intrinsically flexible thermistor materials, our design has superior temperature sensing performance while still having good bending performance.

The thesis objective was therefore partially completed. A thermistor was designed using functional granular composites to create a mechanically flexible temperature sensor. However, the expectation was that a resistivity on the order of $\rho_{25} \approx 10^1 - 10^2\ \Omega cm$ was obtainable with a B-value > 3000 K. The composite thermistor design achieved a B-value above 3000 K, but its resistivity is in the order of $\rho_{25} \approx 10^3 - 10^4\ \Omega cm$. The desired mechanical flexibility was to survive bending radii ≤ 1 cm over 100 cycles. The composite with 10 wt% could survive 100 cycles with a bending radius as low as 2.5 mm ($\varepsilon \approx 2.44\%$) but its resistance increased significantly.

The results are very promising and future work should look into increasing the copper content back to a composition of $Cu_{0.3}Ni_{0.5}Mn_{2.2}O_4$ since the sintered pellets showed that a higher density and lower resistivity was obtainable with higher copper content. However, as a filler in an Electrodag matrix a high B-value might still be attainable. A logical next step to improve bending performance would be to encapsulate the Electrodag-NiMnCuO composite by laminating a sheet of PET on top of the composite. This would shift the neutral axis of bending higher and the composite would experience less stress for the same bending radius. Physically, encapsulation is also expected to help with holding the system together and making it more robust. Furthermore, it should be investigated whether the bending performance could be improved by spinning thinner fibres, by either using smaller spinneret holes or a higher stretching ratio, without experiencing a trade-off in lower thermistor performance.

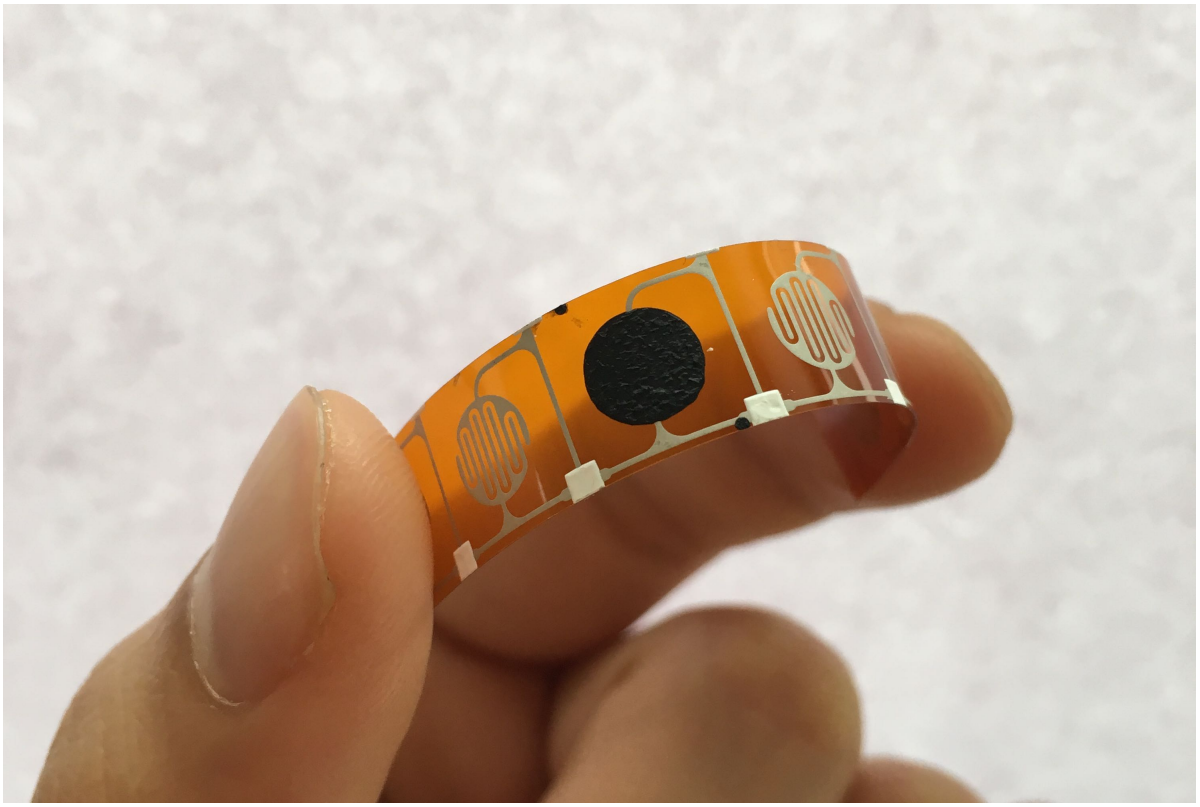

Figure 8.1: Flexible NTC Thermistor Design

References

[1] O. S. Aleksic, M. V. Nikolic, M. D. Lukovic, N. Nikolic, B. M. Radojcic, M. Radovanovic, Z. Djuric, M. Mitric, and P. M. Nikolic. *Preparation and characterization of Cu and Zn modified nickel manganite NTC powders and thick film thermistors*. *Materials Science and Engineering B: Solid-State Materials for Advanced Technology*, 178(3):202–210, 2013. ISSN 09215107. doi: 10.1016/j.mseb.2012.11.003.

[2] Ametherm. *4 Most Common Types of Tempearture Sensor*. URL https://www.ametherm.com/blog/thermistors/temperature-sensor-types. Online; accessed: 02-03-2017.

[3] askIITians. *Close Packing in Crystals*. URL http://www.askiitians.com/iit-jee-solid-state/close-packing-in-crystals/. Online; accessed: 02-03-2017.

[4] AtlasScientific. *PT-1000 Temperature Probe Datasheet*. Atlas Scientific LLC, 630 Flushing Avenue, Brooklyn, NY, v 1.0 edition, 05 2017.

[5] Raquel Barras, Inês Cunha, Diana Gaspar, Elvira Fortunato, Rodrigo Martins, and Luis Pereira. *Printable cellulose-based electroconductive composites for sensing elements in paper electronics*. *Flexible and Printed Electronics*, 2, 2017. ISSN 2058-8585. doi: 10.1088/2058-8585/aa5ef9.

[6] Ramaraju Bendi, Venkateswarlu Bhavanasi, Kaushik Parida, Viet Cuong Nguyen, Afriyanti Sumboja, Kazuhito Tsukagoshi, and Pooi See Lee. *Self-powered graphene thermistor*. *Nano Energy*, 26:586–594, 2016. ISSN 22112855. doi: 10.1016/j.nanoen.2016.06.014.

[7] Sylwia Bielska, Maciej Sibinski, and Andrzej Lukasik. *Polymer temperature sensor for textronic applications*. *Materials Science and Engineering B: Solid-State Materials for Advanced Technology*, 165(1-2):50–52, 2009. ISSN 09215107. doi: 10.1016/j.mseb.2009.07.014.

[8] Myles W. Billard, Hitesh A. Basantani, Mark W. Horn, and Bruce J. Gluckman. *A Flexible Vanadium Oxide Thermistor Array for Localized Temperature Field Measurements in Brain*. *IEEE SENSORS JOURNAL*, 16(8):2211–2212, 2016. doi: 10.1109/JSEN.2016.2517161.

[9] O Bodak, L Akselrud, P Demchenko, B Kotur, O Mrooz, I Hadzaman, O Shpotyuk, F Aldinger, H Seifert, S Volkov, and V Pekhnyo. *Microstructure, crystal structure and electrical properties of* $Cu_{0.1}Ni_{0.8}Co_{0.2}Mn_{1.9}O_4$ *ceramics obtained at different sintering conditions*. *Journal of Alloys and Compounds*, 347(1):14–23, 2002. ISSN 0925-8388. doi: https://doi.org/10.1016/S0925-8388(02)00675-8.

[10] Tim De Chant. *In Ten Years, You Won't Even Know You're Wearing Them*. URL http://www.pbs.org/wgbh/nova/next/tech/wearable-health-sensors/. Online; accessed: 05-03-2017.

[11] Kunmo Chu, Sung-Chul Lee, Sangeui Lee, Dongearn Kim, Changyoul Moon, and Sung-Hoon Park. *Smart conducting polymer composites having zero temperature coefficient of resistance*. *Nanoscale*, 7(2):471–478, 2015. ISSN 2040-3364. doi: 10.1039/C4NR04489D.

[12] Crystallography365. *The world's most underappreciated gemstone - Red Spinel*. URL https://crystallography365.wordpress.com. Online; accessed: 02-03-2017.

[13] D.B. Deutz. *Structure property relationships for NTC ceramics (I) and polymer composites (II)*. Master's thesis, Delft University of Technology, 2013.

[14] EDGEFX.in. *Know about Various Types of Temperature Sensors*. URL https://www.edgefx.in/6-different-types-of-temperature-sensors-with-their-specifications/. Online; accessed: 05-03-2017.

[15] E. Elbadraoui, J.L. Baudour, F. Bouree, B. Gillot, S. Fritsche, and A. Rousset. *Cation distribution and mechanism of electrical conduction in nickel-copper manganite spinels*. *Solid State Ionics*, 93(3-4):219–225, 1997. ISSN 01672738. doi: 10.1016/S0167-2738(96)00559-0.

[16] Ali Elham. *Structural Design: Weight Estimation*. John Wiley and Sons, Ltd, 2010. ISBN 9780470686652. doi: 10.1002/9780470686652.eae598.

[17] Antonio Feteira. *Negative temperature coefficient resistance (NTCR) ceramic thermistors: An industrial perspective*. *Journal of the American Ceramic Society*, 92(5):967–983, 2009. ISSN 00027820. doi: 10.1111/j.1551-2916.2009.02990.x.

[18] Jun Feng Gao, Dao Lai Fang, Zhong Bing Wang, Ping Hua Yang, and Chu Sheng Chen. *Preparation and electrical properties of copper-nickel manganite ceramic derived from mixed oxalate*. *Sensors and Actuators, A: Physical*, 135(2):472–475, 2007. ISSN 09244247. doi: 10.1016/j.sna.2006.09.005.

[19] W. A. Groen, C. Metzmacher, P. Huppertz, and S. Schuurman. *Aging of NTC Ceramics in the System Mn-Ni-Fe-O*. *Journal of Electroceramics*, 7(2):77–87, 2001. doi: 10.1023/B:JECR.0000027947.28060.33.

[20] Weili Hu, Xiaofan Niu, Ran Zhao, and Qibing Pei. *Elastomeric transparent capacitive sensors based on an interpenetrating composite of silver nanowires and polyurethane*. *Applied Physics Letters*, 102(8), 2013. ISSN 00036951. doi: 10.1063/1.4794143.

[21] Chun Chih Huang, Zhen Kai Kao, and Ying Chih Liao. *Flexible miniaturized nickel oxide thermistor arrays via inkjet printing technology*. *ACS Applied Materials and Interfaces*, 5(24):12954–12959, 2013. ISSN 19448244. doi: 10.1021/am404872j.

[22] AspenCore Inc. *Temperature Sensors*. URL http://www.electronics-tutorials.ws/io/io_3.html. Online; accessed: 05-03-2017.

[23] Yasser Khan, Mohit Garg, Qiong Gui, Mark Schadt, Abhinav Gaikwad, Donggeon Han, Natasha A D Yamamoto, Paul Hart, Robert Welte, William Wilson, Steve Czarnecki, Mark Poliks, Zhanpeng Jin, Kanad Ghose, Frank Egitto, James Turner, and Ana C. Arias. *Flexible Hybrid Electronics: Direct Interfacing of Soft and Hard Electronics for Wearable Health Monitoring*. *Advanced Functional Materials*, pages 8764–8775, 2016. ISSN 16163028. doi: 10.1002/adfm.201603763.

[24] De Kong, Linh T. Le, Yue Li, James L. Zunino, and Woo Lee. *Temperature-dependent electrical properties of graphene inkjet-printed on flexible materials*. *Langmuir*, 28(37):13467–13472, 2012. ISSN 07437463. doi: 10.1021/la301775d.

[25] Wenwen Kong, Wei Wei, Bo Gao, and Aimin Chang. $Mn_{1.56}Co_{0.96}Ni_{0.48}O_4$ *flexible thin films fabricated by pulsed laser deposition for NTC applications*. *Materials Science & Engineering*, 206: 39–44, 2016. ISSN 0921-5107. doi: 10.1016/j.mseb.2015.10.012.

[26] Arvind Kumar, Madan Lal Singla, Amod Kumar, and Jaspreet Kaur Rajput. *HCl/CSA doped* $POT-Mn_3O_4$ *nanocomposites based conformable thin film temperature sensor for prosthetic hand gloves*. *Journal of Materials Science: Materials in Electronics*, 26(3):1838–1852, 2015. ISSN 1573482X. doi: 10.1007/s10854-014-2619-2.

[27] T.R. Kuphaldt. *Lessons in Electric Circuits Vol. 1 Direct Current*. Koros Press Limited, 2011. ISBN 9781907653087.

[28] Someya Group Organic Transistors Lab. *Electronic Artificial Skin*. URL http://www.ntech.t.u-tokyo.ac.jp/en/research_results/index.html. Online; accessed: 15-01-2018.

[29] Sandia National Laboratories. *Slygard 184: Linear CTE vs Temp*. URL http://www.sandia.gov/polymer-properties/E1-CTE_vs_temp.html. Online; accessed: 07-02-2018.

[30] Daniel Langley, Gael Giusti, Celine Mayousse, Caroline Celle, Daniel Bellet, and Jean-Pierre Simonato. *Flexible transparent conductive materials based on silver nanowire networks: a review*. *Nanotechnology*, 24(45):452001, 2013. doi: 10.1088/0957-4484/24/45/452001.

[31] E G Larson, R J Arnott, and D G Wickham. *Preparation, Semiconduction and Low-Temperature Magnetization of the system* $Ni_{1-x}Mn_{2+x}O_4$. *Journal of Physics and Chemistry Solids*, 23:1771–1781, 1962. ISSN 00223697.

[32] Duc Thang Le, Chang Jun Jeon, Young Hun Jeong, Ji Sun Yun, Dae Ho Yoon, and Jeong Ho Cho. *High performance of temperature sensitive thin film fabricated onto flexible substrates*. *Journal of Alloys and Compounds*, 686:982–988, 2016. ISSN 09258388. doi: 10.1016/j.jallcom.2016.06.237.

[33] Victor Lebedev, Elena Laukhina, Vladimir Laukhin, Andrey Somov, Alexander M. Baranov, Concepcio Rovira, and Jaume Veciana. *Investigation of sensing capabilities of organic bi-layer thermistor in wearable e-textile and wireless sensing devices*. *Organic Electronics*, 42:146–152, 2017. ISSN 15661199. doi: 10.1016/j.orgel.2016.12.034.

[34] LibreTexts. *Closest Packed Structures*. URL `https://chem.libretexts.org/Core/Physical_and_Theoretical_Chemistry/Physical_Properties_of_Matter/States_of_Matter/Properties_of_Solids/Crystal_Lattice/Closest_Pack_Structures`. Online; accessed: 02-03-2017.

[35] E.D. Macklen. *Thermistors*. Electrochemical Publications Limited, 1979.

[36] David S. MacLachlan, Michael Blaszkiewicz, and Robert E. Newnham. *Electrical Resistivity of Composites*. *Journal of the American Ceramic Society*, 73(8):2187–2203, 1990. doi: 10.1111/j.1151-2916.1990.tb07576.x.

[37] Suresha K. Mahadeva, Sungryul Yun, and Jaehwan Kim. *Flexible humidity and temperature sensor based on cellulose-polypyrrole nanocomposite*. *Sensors and Actuators, A: Physical*, 165(2):194–199, 2011. ISSN 09244247. doi: 10.1016/j.sna.2010.10.018.

[38] Kowsar Majid, Sajeela Awasthi, and M. L. Singla. *Low temperature sensing capability of polyaniline and* Mn_3O_4 *composite as NTC material*. *Sensors and Actuators, A: Physical*, 135(1):113–118, 2007. ISSN 09244247. doi: 10.1016/j.sna.2006.06.055.

[39] Renaud Metz. *Electrical properties of N.T.C. thermistors made of manganite ceramics of general spinel structure:* $Mn_{3-x-x'}M_xN_{x'}O_4$ *(0 ≤ x + x' ≤ 1; M and N being Ni, Co or Cu). Aging phenomenon study*. *Journal of Materials Science*, 35:4705–4711, 2000. doi: 10.1023/A.

[40] Hemant Moore and Divyendra Patil. *Chemistry - Packing of Solids*. URL `http://hemantmore.org/chemistry-1/solid-state-packing-in-solids/1837/`. Online; accessed: 02-03-2017.

[41] A. J. Moulson and J. M. Herbert. *Electroceramics*. Wiley, second edition, 2003. ISBN 0471497479.

[42] M. N. Muralidharan, P. R. Rohini, E. K. Sunny, K. R. Dayas, and A. Seema. *Effect of Cu and Fe addition on electrical properties of Ni-Mn-Co-O NTC thermistor compositions*. *Ceramics International*, 38(8):6481–6486, 2012. ISSN 02728842. doi: 10.1016/j.ceramint.2012.05.025.

[43] P Murugaraj, D Mainwaring, and N Mora-Huertas. *Thermistor behaviour in a semiconducting polymer–nanoparticle composite film*. *Journal of Physics D: Applied Physics*, 39:2072–2078, 2006. ISSN 0022-3727. doi: 10.1088/0022-3727/39/10/015.

[44] Tomohiko Nakajima and Tetsuo Tsuchiya. *Flexible thermistors: pulsed laser-induced liquid-phase sintering of spinel Mn–Co–Ni oxide films on polyethylene terephthalate sheets*. *Journal of Materials Chemistry C*, 3:3809–3816, 2015. ISSN 2050-7526. doi: 10.1039/C5TC00327J.

[45] R E Newnham. *Composite Electroceramics*. *Ferroelectrics*, 68(1):1–32, 1986. ISSN 0015-0193. doi: 10.1080/00150198608238734.

[46] R. E. Newnham, D.P. Skinner, and L.E. Cross. *Connectivity and Piezoelectric-Pyroelectric Composites*. *Materials Research Bulletin*, 13(5):525–536, 1978.

[47] Alexandros Pantelopoulos and Nikolaos G. Bourbakis. *A survey on wearable sensor-based systems for health monitoring and prognosis*. *IEEE Transactions on Systems, Man and Cybernetics Part C: Applications and Reviews*, 40(1):1–12, 2010. ISSN 10946977. doi: 10.1109/TSMCC.2009.2032660.

[48] K. Park and J. K. Lee. *Mn-Ni-Co-Cu-Zn-O NTC thermistors with high thermal stability for low resistance applications*. *Scripta Materialia*, 57(4):329–332, 2007. ISSN 13596462. doi: 10.1016/j.scriptamat.2007.04.026.

[49] A. Rousset, R. Legros, and A. Lagrange. *Recent progress in the fabrication of ceramic negative temperature coefficient thermistors*. *Journal of the European Ceramic Society*, 13(3):185–195, 1994. ISSN 09552219. doi: 10.1016/0955-2219(94)90027-2.

[50] G. R. Ruschau, S. Yoshikawa, and R. E. Newnham. *Resistivities of conductive composites*. *Journal of Applied Physics*, 72(3):953–959, 1992. ISSN 00218979. doi: 10.1063/1.352350.

[51] G.R. Ruschau, S. Yoshikawa, and R.E. Newnham. *Percolation constraints in the use of conductor-filled polymers for interconnects*. *Proceedings 42nd Electronic Components & Technology Conference*, pages 481–486, 1992. ISSN 05695503. doi: 10.1109/ECTC.1992.204249.

[52] A. Safari. *Developement of Piezoelectric Composites for Transducers*. *Journal de Physique III*, 4:1129–1149, 1994.

[53] Takao Someya, Tsuyoshi Sekitani, Shingo Iba, Yusaku Kato, Hiroshi Kawaguchi, and Takayasu Sakurai. *A large-area, flexible pressure sensor matrix with organic field-effect transistors for artificial skin applications*. *Proceedings of the National Academy of Sciences of the United States of America*, 101(27):9966–9970, 2004. doi: 10.1073/pnas.0401918101.

[54] Vincent L. Stuber. *Lead-free Piezoelectric Composites for Energy Harvesting Applications*. Master's thesis, Delft University of Technology, 2017.

[55] E J W Verwey and E L Heilmann. *Physical Properties and Cation Arrangement of Oxides with Spinel Structures*. *The Journal of Chemical Physics*, 15(4):174–180, 1947. ISSN 00219606. doi: 10.1063/1.1746466.

[56] Tiina Vuorinen, Juha Niittynen, Timo Kankkunen, Thomas M. Kraft, and Matti Mäntysalo. *Inkjet-Printed Graphene/PEDOT:PSS Temperature Sensors on a Skin-Conformable Polyurethane Substrate*. *Scientific Reports*, 6(35289), 2016. ISSN 2045-2322. doi: 10.1038/srep35289.

[57] Zhizhen Wu, Chunyan Li, Jed Hartings, Sthitodhi Ghosh, Raj Narayan, and Chong Ahn. *Polysilicon-based flexible temperature sensor for brain monitoring with high spatial resolution*. *Journal of Micromechanics and Microengineering*, 27(2):025001, 2017. ISSN 0960-1317. doi: 10.1088/1361-6439/aa4e99.

[58] Suyan Xiao, Lufeng F. Che, Xinxin Li, and Yuelin Wang. *A cost-effective flexible MEMS technique for temperature sensing*. *Microelectronics Journal*, 38(3):360–364, 2007. ISSN 00262692. doi: 10.1016/j.mejo.2007.01.022.

[59] Chaoyi Yan, Jiangxin Wang, and Pooi See Lee. *Stretchable graphene thermistor with tunable thermal index*. *ACS Nano*, 9(2):2130–2137, 2015. ISSN 1936086X. doi: 10.1021/nn507441c.

[60] Y Yang, M Cheng, W Chang, L Tsao, and S Yang. *An integrated flexible temperature and tactile sensing array using PI-copper films*. *Sensors And Actuators*, 143(May):143–153, 2008. ISSN 09244247. doi: 10.1016/j.sna.2007.10.077.

[61] Cunjiang Yu, Ziyu Wang, Hongyu Yu, and Hanqing Jiang. *A stretchable temperature sensor based on elastically buckled thin film devices on elastomeric substrates*. *Applied Physics Letters*, 95(14), 2009. ISSN 00036951. doi: 10.1063/1.3243692.

[62] Chunhua Zhao, Biyun Wang, Pinghua Yang, Louis Winnubst, and Chusheng Chen. *Effects of Cu and Zn co-doping on the electrical properties of* $Ni_{0.5}Mn_{2.5}O_4$ *NTC ceramics*. *Journal of the European Ceramic Society*, 28(1):35–40, 2008. ISSN 09552219. doi: 10.1016/j.jeurceramsoc.2007.06.007.

A

Summary of Relevant Flexible Temperature Sensors in Literature

N	Flexible Thermistor Systems	Form	Shape	Flexible	Thermistor	Particle size	$\Phi_c[\%]$	Interparticle d	$\alpha[\%K^{-1}]$
1	NiMnO - Epoxy (Epotek 302-3M)	Composite	Composite moulded into disk	Yes	NTC	$10-100\mu m$	$45vol\%$	$0.6\mu m$	-
2	Mn3O4 - Polyaniline	Composite	Composite pressed into pellet	Yes	NTC	$45\mu m$	-	-	
3	NiO-(polystyrene-butadiene rubber)	Composite	Composite stencil printed on polyimide thin-film	Yes	NTC	$0.5-1.5\mu m$	6:2 Wt Ratio NiO:PSBR	-	$\alpha=-5.84$
4	NiO on polyimide substrate	Thin Film	Inkjet printed on Polyimide thin-film	Yes	NTC	50 nm	100%	-	-
5	Graphene (with nanocellulose binder) in Polydimethylsiloxane (PDMS)	Composite	Serpintine channel embedded into PDMS matrix	Yes	NTC	graphene crumpled sheets (chips/platelets)	100%	-	$\alpha_{27}=-1.05$
6	Graphene on polyethylene terephthalate (PET)	Thin Film	Thin-film on PET substrate	Yes	NTC	graphene multilayers	100%	-	$\alpha_{25}=-1.48$
7	Graphene on P(VDF-TrFE) thin film	Thin Film	Thin-Film on PET substrate	Yes	NTC	graphene monolayer/multilayer	100%	-	-
8	Graphene on P(VDF-TrFE) thin film	Thin Film	Thin-Film on PET substrate	Yes	NTC	graphene monolayer/multilayer	100%	-	-
9	Buckled Cr/Au on silicon ribbon on PDMS thin film	Thin-Film	Wavy thin-film on PDMS substrate	Yes	PTC	Cr (5nm) Au (200nm) Si ($400\mu m$)	-	-	-
10	Carbon Nanoparticles in Polyimide Composite	Composite	Composite slipcasted into a thin-film	Yes	NTC	30nm	$1-8vol\%$	-	$\alpha=(-)0.14-(-)0.05$
11	Graphene and (PEDOT:PSS) Composite ink	Composite	Inkjet Printed composite onto polyurethane substrate	Yes	NTC	-	$(1-5)wt\%$ graphene, $(1-5)wt\%$ PEDOT:PSS	-	$\alpha=-0.034$
12	Carbon fibre and carboxymethyl cellulose composite Ink	Composite	Screen printed composite onto paper	Yes	NTC	10 printed layers	CF ($10wt\%$) and CMC ($3wt\%$) and Water	-	$\alpha_{25}=-0.079$
13	Mn-Co-Ni-O on Polyimide	Thin-Film	Liquid Flow Deposition on polyimide substrate	Yes	NTC	-	100%	-	$\alpha_{27}=-2.76$
14	Polycarbonate/$\alpha'-(BEDT-TTF)_2I_xBr_{3-x}$ bi-layer film	Thin-Film	Thin-Film glued to polyester textile	Yes	NTC	-	-	-	$\alpha=-1.2$
15	Vanadium oxide on Polyimide	Thin-Film	Through-film thermistor	Yes	NTC	-	100%	-	$\alpha=-4.060$
16	Mn-Co-Ni-O on Polyimide	Thin-Film	Pulsed lazer deposition of MCN on polyimide substrate	Yes	NTC	-	100%	-	$\alpha=-5.47$
17	Poly-o-toluidine-Mn_3O_4 nanocomposites thin film	Composite	Composite thin-film prepared onto glass cloth substrate	Yes	NTC	-	-	-	-
18	Mn-Co-Ni-O with methylcellulose resin on PET	Thin-Film	Pulsed laser-induced sintering onto PET substrate	Yes	NTC	286.3 nm	100%	-	-
19	Polysilicon thermistor array on flexible polyimide substrate	Thin-Film	Polysilicon by AIC process on polyimide substrate	Yes	NTC	-	-	-	$\alpha=-0.31$

Table A.1: Summary of Relevant Flexible NTC Thermistor Systems in Literature - Part I

N	Flexible Thermistor Systems	B-value [K]	Temp Range [$^\circ C$]	$\rho[\Omega cm]$	$\tau[s]$	Bending Tested	Source	Year	Comments
1	NiMnO - Epoxy (Epotek 302-3M)	$B_{25/85}=1500$ (f=1kHz, V=1V)	-	$\rho_{25}=10^5$	-	-	[13]	2013	Agglomerated Particles
2	Mn3O4 - Polyaniline	$B_{10/100}=3614$	15-170	$\rho_{25}=10^4$	-	-	[38]	2007	Above $200^\circ C$ polymer decomposes
3	NiO-(polystyrene-butadiene rubber)	$B_{20/40}=4330$	20-40	$\rho_{30}=3.5\cdot10^4$	$\tau_{31/22}=10$	$r=2.5cm, R/R0=4\%$	[23]	2016	Stencil printed onto Kapton PI substrate
4	NiO on polyimide substrate	$B_{25/200}=4300$	15-200	$\rho_{50}=7.7\cdot10^4$	$\tau_{30/22}\approx11$	$r=1cm, R/R0=5\%$	[21]	2013	Inkjet printed thin film onto polyimide film
5	Graphene (with nanocellulose binder) in Polydimethylsiloxane (PDMS)	$B_{30/100}=847$ (increases with strain)	30-100	-	-	$\epsilon=50\%, R/R0=1125\%$	[59]	2015	Strechable Graphene Thermistor ($0<\epsilon<50\%$)
6	Graphene on polyethylene terephthalate (PET)	$B_{25/85}=1860$	25-85	-	-	bending $2\theta=27.4^\circ, R/R0=-5.6\%$	[24]	2012	Inket printed graphene thin film on PET
7	Graphene on P(VDF-TrFE) thin film	$B_{22/110}=250$	22-110	-	-	-	[6]	2016	Flexible Thermistor - Unpoled
8	Graphene on P(VDF-TrFE) thin film	$B_{22/40}=18000$	22-40	-	-	-	[6]	2016	Self-Powered, Flexible Thermistor - Poled
9	Buckled Cr/Au on silicon ribbon on PDMS thin film	-	25-110	-	-	$\epsilon=30\%, R/R0=0\%$	[61]	2009	Stretchable to $\epsilon=30\%$ with no performance change
10	Carbon Nanoparticles in Polyimide Composite	$B_{25/100}=192-76$	25-100	$\rho=10^6-10^1$	-	-	[43]	2006	Carbon particles may have aggregated
11	Graphene and (PEDOT:PSS) Composite ink	-	35-45	-	-	-	[56]	2016	Practically unstable due to high moisture sensitivity
12	Carbon fibre and carboxymethyl cellulose composite Ink	-	25-75	-	-	$r=5mm$ 1000 cycles, $R/R0=50\%$	[5]	2017	Also very moisture sensitive
13	Mn-Co-Ni-O on Polyimide	-	20-110	$\rho_{27}=250$	-	-	[32]	2016	High α, Low ρ, No proof of flexibility
14	Polycarbonate/$\alpha'-(BEDT-TTF)_2I_xBr_{3-x}$ bi-layer film	-	30-60	-	-	-	[33]	2017	Temperature sensing fabric, Attaching process caused cracks
15	Vanadium oxide on Polyimide	-	20-57	-	-	-	[8]	2016	Degree of flexibility is unknown
16	Mn-Co-Ni-O on Polyimide	$B_{50/100}=4920$	27-120	$\rho_{27}=920$	-	-	[25]	2016	Degree of flexibility is unknown
17	Poly-o-toluidine-Mn_3O_4 nanocomposites thin film	$B_{100/170}=6210-8824$	30-185	-	-	-	[26]	2015	Require doping with HCL or CSA, No mechanical flexibility testing
18	Mn-Co-Ni-O with methylcellulose resin on PET	$B=4429$	-	$\rho=518\cdot10^3$	$\tau_{30/22}=1.8s$	r = 3.0 cm, 40 cycles, $R/R0=2.3\%$	[44]	2015	High B-value, but very high resistivity
19	Polysilicon thermistor array on flexible polyimide substrate	-	30-45	-	$\tau_{25/40}=0.8s$	-	[57]	2017	Degree of flexibility is unknown

Table A.2: Summary of Relevant Flexible NTC Thermistor Systems in Literature - Part II

B

Summary of Relevant NTC Ceramic Compositions Found in Literature

N	Ceramic NTC	Form	resistivity $\rho[\Omega cm]$	B-value [K]	Temperature Coefficient of Resistance $[\%/K]$	Activation Energy, q [eV]	$\Delta R/R[\%]$	Source	Year
1	$NiMnO$	Pellets	$\rho_{25} = 1.1 \cdot 10^3$	$B_{25/85} = 4000$	-	-	-	[13]	2013
2	Mn_3O_4	-	10^6	-	-	-	-	[38]	2007
3	NiO	Thin-film	-	4300	-	-	-	[21]	2013
4	$Mn_{3-x}Ni_xO_4$	-	2500-1000 for x=0.5-1.0	-	-	-	$\approx 3\%$ (Aged $125°C$ for 1000h)	[49]	1994
5	$Mn_{2.25-x}Ni_{0.75}Co_xO_4$	-	2000-300 for x=0.0-1.0	-	-	-	-	[49]	1994
6	$Mn_{2.3-x}Ni_{0.70}Cu_xO_4$	-	2000-3 for x=0.0-0.6	-	-	-	$\approx 12\%$ (Aged $125°C$ for 1000h)	[49]	1994
7	$Mn_{2.04}Ni_{0.66}Cu_{0.3}O_4$	Disk	$\rho_{25} = 63.3$	$B_{25/50} = 2740$	-	-	5.4% (@T=25, Aged $150°C$ for 500h)	[18]	2007
8	$Mn_{1.5-x}Ni_{0.5}Cu_xZn_{1.0}O_4$	Disk	$\rho_{25} = 3216 - 750$ for x=0.0-0.4	$B_{25/50} = 3891 - 3590$ for x=0.0-0.4	-	-	2.6% (@T=25, Aged $150°C$ for 1000h) for x =0.0-0.4	[62]	2008
9	$Mn_{2.5-x}Ni_{0.5}Cu_xO_4$	Disk	$\rho_{25} = 2907 - 12.6$ for x=0.0-0.4	$B_{25/50} = 3970 - 2760$ for x=0.0-0.4	-	-	$2.6 - 15\%$ (@T=25, Aged $150°C$ for 1000h) for x =0.0-0.4	[62]	2008
10	$Mn_{2.3}Ni_{0.7}O_4$	Disk	$\rho_{25} = 2087$	$B_{25/85} = 3847$	$\alpha_{25} = -4.332012$	0.331611	0.52% (@T=25, Aged $120°C$ for 168h)	[42]	2012
11	$Mn_{2.2}Ni_{0.7}Co_{0.1}O_4$	Disk	$\rho_{25} = 1584$	$B_{25/85} = 3804$	$\alpha_{25} = -4.283591$	0.327905	0.39% (@T=25, Aged $120°C$ for 168h)	[42]	2012
12	$Mn_{2.0}Ni_{0.7}Co_{0.3}O_4$	Disk	$\rho_{25} = 996$	$B_{25/85} = 3642$	$\alpha_{25} = -4.101167$	0.31394	0.31% (@T=25, Aged $120°C$ for 168h)	[42]	2012
13	$Mn_{1.8}Ni_{0.7}Co_{0.5}O_4$	Disk	$\rho_{25} = 725$	$B_{25/85} = 3563$	$\alpha_{25} = -4.012207$	0.307131	0.34% (@T=25, Aged $120°C$ for 168h)	[42]	2012
14	$Mn_{1.6}Ni_{0.7}Co_{0.7}O_4$	Disk	$\rho_{25} = 538$	$B_{25/85} = 3478$	$\alpha_{25} = -3.916490$	0.299804	0.39% (@T=25, Aged $120°C$ for 168h)	[42]	2012
15	$Mn_{1.79}Ni_{0.7}Co_{0.5}Cu_{0.01}O_4$	Disk	$\rho_{25} = 585$	$B_{25/85} = 3508$	$\alpha_{25} = -3.950273$	0.30239	0.30% (@T=25, Aged $120°C$ for 168h)	[42]	2012
16	$Mn_{1.78}Ni_{0.7}Co_{0.5}Cu_{0.02}O_4$	Disk	$\rho_{25} = 513$	$B_{25/85} = 3462$	$\alpha_{25} = -3.898473$	0.298424	0.18% (@T=25, Aged $120°C$ for 168h)	[42]	2012
17	$Mn_{1.77}Ni_{0.7}Co_{0.5}Cu_{0.03}O_4$	Disk	$\rho_{25} = 444$	$B_{25/85} = 3425$	$\alpha_{25} = -3.856808$	0.295235	0.44% (@T=25, Aged $120°C$ for 168h)	[42]	2012
18	$Mn_{1.76}Ni_{0.7}Co_{0.5}Cu_{0.04}O_4$	Disk	$\rho_{25} = 402$	$B_{25/85} = 3332$	$\alpha_{25} = -3.752083$	0.287218	0.45% (@T=25, Aged $120°C$ for 168h)	[42]	2012
19	$Mn_{1.75}Ni_{0.7}Co_{0.5}Cu_{0.05}O_4$	Disk	$\rho_{25} = 354$	$B_{25/85} = 3373$	$\alpha_{25} = -3.798252$	0.290753	0.64% (@T=25, Aged $120°C$ for 168h)	[42]	2012
20	$Mn_{1.7}Ni_{0.7}Co_{0.5}Fe_{0.1}O_4$	Disk	$\rho_{25} = 947$	$B_{25/85} = 3589$	$\alpha_{25} = -4.041485$	0.309372	0.36% (@T=25, Aged $120°C$ for 168h)	[42]	2012
21	$Mn_{1.5}Ni_{0.7}Co_{0.5}Fe_{0.3}O_4$	Disk	$\rho_{25} = 1213$	$B_{25/85} = 3441$	$\alpha_{25} = -3.874825$	0.296614	0.29% (@T=25, Aged $120°C$ for 168h)	[42]	2012
22	$Mn_{1.3}Ni_{0.7}Co_{0.5}Fe_{0.5}O_4$	Disk	$\rho_{25} = 1207$	$B_{25/85} = 3233$	$\alpha_{25} = -3.640602$	0.278685	0.24% (@T=25, Aged $1120°C$ for 168h)	[42]	2012
23	$Mn_{1.1}Ni_{0.7}Co_{0.5}Fe_{0.7}O_4$	Disk	$\rho_{25} = 1506$	$B_{25/85} = 3257$	$\alpha_{25} = -3.667628$	0.280753	0.21% (@T=25, Aged $120°C$ for 168h)	[42]	2012
24	$Mn_{1.95}Ni_{0.45}Co_{0.15}Cu_{0.45}O_4$	-	$\rho_{25} = 30.7$	$B_{25/85} = 2875$	-	0.25	-	[48]	2007
25	$Mn_{1.89}Ni_{0.45}Co_{0.15}Cu_{0.45}Zn_{0.064}O_4$	-	$\rho_{25} = 41.3$	$B_{25/85} = 3021$	-	0.26	-	[48]	2007
26	$Mn_{1.83}Ni_{0.45}Co_{0.15}Cu_{0.45}Zn_{0.12}O_4$	-	$\rho_{25} = 54.1$	$B_{25/85} = 3169$	-	0.27	-	[48]	2007
27	$Mn_{1.77}Ni_{0.45}Co_{0.15}Cu_{0.45}Zn_{0.18}O_4$	-	$\rho 25 = 26.1$	$B_{25/85} = 2887$	-	0.25	-	[48]	2007
28	$Mn_{1.71}Ni_{0.45}Co_{0.15}Cu_{0.45}Zn_{0.24}O_4$	-	$\rho_{25} = 14.0$	$B_{25/85} = 2427$	-	0.21	-	[48]	2007
29	$Mn_{1.65}Ni_{0.45}Co_{0.15}Cu_{0.45}Zn_{0.3}O_4$	-	$\rho_{25} = 22.9$	$B_{25/85} = 2791$	-	0.24	-	[48]	2007
30	$Mn_{1.9}Ni_{0.8}Co_{0.2}Cu_{0.1}O_4$	Disk	$\rho_{25} = 312.5$	$B_{25/85} = 3160$	-	-	-	[9]	2002
31	$Mn_{1.56}Ni_{0.48}Co_{0.96}O_4$	Thin-film	$\rho_{25} = 920$	$B_{50/100} = 4920$	$\alpha_{25} = -5.47$	0.41	-	[25]	2016
32	$Mn_{1.89}Ni_{0.66}Cu_{0.45}O_4$	Disk	$\rho_{25} = 10.6$	-	-	-	39% (@T=25, Aged $125°C$ for 1000h)	[39]	2000
33	$Mn_{1.3}Ni_{0.5}Cu_{0.2}Zn_{1.0}O_4$	Disk	$\rho_{20} = 2555$	B(Ea/k) = 3424	-	0.299	0.23% (@T=25, Aged $150°C$ for 800h)	[1]	2013
34	$Mn_{1.25}Ni_{0.5}Cu_{0.25}Zn_{1.0}O_4$	Disk	$\rho_{20} = 2222$	B(Ea/k) = 3406	-	0.298	0.51% (@T=25, Aged $150°C$ for 800h)	[1]	2013
35	$Mn_{2.1}Ni_{0.5}Cu_{0.4}O_4$	Disk	$\rho_{20} = 45.97$	B(Ea/k) = 2632	-	0.231	19.2% (@T=25, Aged $150°C$ for 800h)	[1]	2013

Table B.1: Summary of Relevant NTC Ceramics for Thermistors Found in Literature

C

Summary of polymers used as matrix or substrates in flexible thermistor systems in Literature

N	Polymer Matrix	Use	Tg [°C]	$\rho[\Omega cm]$	B-value [K]	Curing Temp	CTE (below Tg)	CTE (above Tg)	Degradation T[°C]	Dielectric Constant	Wetting	Thermal Conductivity	Working Time	Stiffness
1	Epoxy (Epotek 302-3M)	Matrix	55	$\rho = 10^{14}$	$B_{25/85} = 100$ (f=1kHz, V=1V)	$20 - 200°C$	$56 \cdot 10^{-6} in/in/°C$	$193 \cdot 10^{-6} in/in/°C$	350	3.4 (1 KHz)	High	-	-	-
2	Polyaniline (PANI)	Binder	-	$\rho = 10^{6}$	-	-	-	-	200	-	Low	-	-	-
3	Polystyrene-butadiene rubber (PSBR) (Targray Technology)	Matrix	-	-	-	140 °C (2hrs)	-	-	-	-	-	-	-	-
4	Polydimethylsiloxane (PDMS)	Matrix	-	-	-	60°C (2hrs)	-	-	-	-	-	0.15 [W/m/K at 25°C]	-	-
5	Polyurethane (PU)	Matrix	-	-	-	-	-	-	-	4.5	-	-	9 mins	595 MPa
6	Polydimethylsiloxane (PDMS)	Matrix	-	-	-	-	-	-	-	2.7	-	-	long	6 MPa
7	Polyimide	Matrix	-	-	-	-	-	-	-	-	-	-	-	-
8	PEDOT:PSS	Matrix	-	-	-	130°C (10 mins)	-	-	-	-	-	-	-	-
9	Carboxymethyl cellulose	Matrix	-	-	-	-	-	-	-	-	-	-	-	-
N	**Polymer Substrate**	**Use**	**Tg [°C]**	$\rho[\Omega cm]$	**B-value [K]**	**Curing Temp**	**CTE (below Tg)**	**CTE (above Tg)**	**Degradation T[°C]**	**Dielectric Constant**	**Wetting**	**Thermal Conductivity**	**Working Time**	**Stiffness**
10	Kapton Polyimide	Thin-Film Substrate	-	-	-	-	-	-	-	-	-	-	-	-
11	Polyimide	Thin-Film Substrate	-	-	-	-	-	-	-	-	-	-	-	-
12	Polyethylene Terephthalate (PET)	Thin-Film Substrate	-	-	-	-	-	-	-	-	-	-	-	-
13	Poly[(vinylide-nefluoride-co-trifluoroethylene)] (PVDF-TrFE)	Thin-Film Substrate	-	-	-	-	-	-	-	-	-	-	-	-
14	Polyethylene (PET)	Thin-Film Substrate	-	-	-	25°C, 90 min	-	-	-	-	-	-	-	-
15	Polydimethylsiloxane (PDMS)	Thin-Film Substrate	-	-	-	25°C, 90 min and 100°C, 90 min	-	-	-	-	-	-	-	-
16	Polyurethane Substrate	Thin-Film Substrate	-	-	-	-	-	-	-	-	-	-	-	-
17	Polyimide	Thin-Film Substrate	-	-	-	-	-	-	-	-	-	-	-	-
18	Polyimide	Thin-Film Substrate	-	-	-	-	-	-	-	-	-	$< 0.002 W/cmK$	-	-
19	Glass Cloth Substrate	Thin-Film Substrate	-	-	-	-	-	-	-	-	-	-	-	-

Table C.1: Summary of relevant polymers used as matrix or substrates in flexible thermistor systems in Literature - Part 1

N	Polymer Matrix	Use	Source	Year	Main Reason Chosen	Comments
1	Epoxy (Epotek 302-3M)	Matrix	[13]	2013	Excellent water, chemical, solvent resistance	High intrinsic resistivity
2	Polyaniline (PANI)	Binder	[38]	2007	Conductive Polymer, Inexpensive monomer, straightforward polymerization reaction, high yield, excellent stability	Decomposes at 170-200°C
3	Polystyrene-butadiene rubber (PSBR) (Targray Technology)	Matrix	[23]	2016	PSBR holds the nanoparticles	-
4	Polydimethylsiloxane (PDMS)	Matrix	[59]	2015	High Stretchability	Low thermal conductivity, but can be made thinner
5	Polyurethane (PU)	Matrix	[54]	2017	Short working time to avoid fibre sinking	-
6	Polydimethylsiloxane (PDMS)	Matrix	[54]	2017	Low Dielectric Constant	-
7	Polyimide	Matrix	[43]	2006	High endurance to high temperature	-
8	PEDOT:PSS	Matrix	[56]	2016	Stretchable with high conductivity and optical transparency	Performance is very moisture sensitive, needs protection
9	Carboxymethyl cellulose	Matrix	[5]	2017	Water soluble cellulose, cheap, renewable, film forming	Moisture sensitive
N	**Polymer Substrate**	**Use**	**Source**	**Year**	**Main Reason Chosen**	**Comments**
10	Kapton Polyimide	Thin-Film Substrate	[23]	2016	-	
11	Polyimide	Thin-Film Substrate	[21]	2013	-	
12	Polyethylene Terephthalate (PET)	Thin-Film Substrate	[24]	2012	Chosen for temperature sensitivity and mechanical flexibility	
13	Poly[(vinylide-nefluoride-co-trifluoroethylene)] (PVDF-TrFE)	Thin-Film Substrate	[6]	2016	Ferroelectric (high remnant polarization charge), chemical inert, flexible, used to enable poling	
14	Polyethylene (PET)	Thin-Film Substrate	[6]	2016	-	
15	Polydimethylsiloxane (PDMS)	Thin-Film Substrate	[61]	2009	-	
16	Polyurethane Substrate	Thin-Film Substrate	[56]	2016	Stretchable substrate for epidermal electronic systems	
17	Polyimide	Thin-Film Substrate	[32]	2016	High Chemical Resistance, High Temperature Stability	
18	Polyimide	Thin-Film Substrate	[25]	2016	Flexible and resistant to high temperature	
19	Glass Cloth Substrate	Thin-Film Substrate	[26]	2015	Flexible, Flame Retardant, Chemically Resistant	

Table C.2: Summary of relevant polymers used as matrix or substrates in flexible thermistor systems in Literature - Part 2

D

Resistance Change After Cyclic Tensile Bending of Sample from Batch G,H,J,K,M

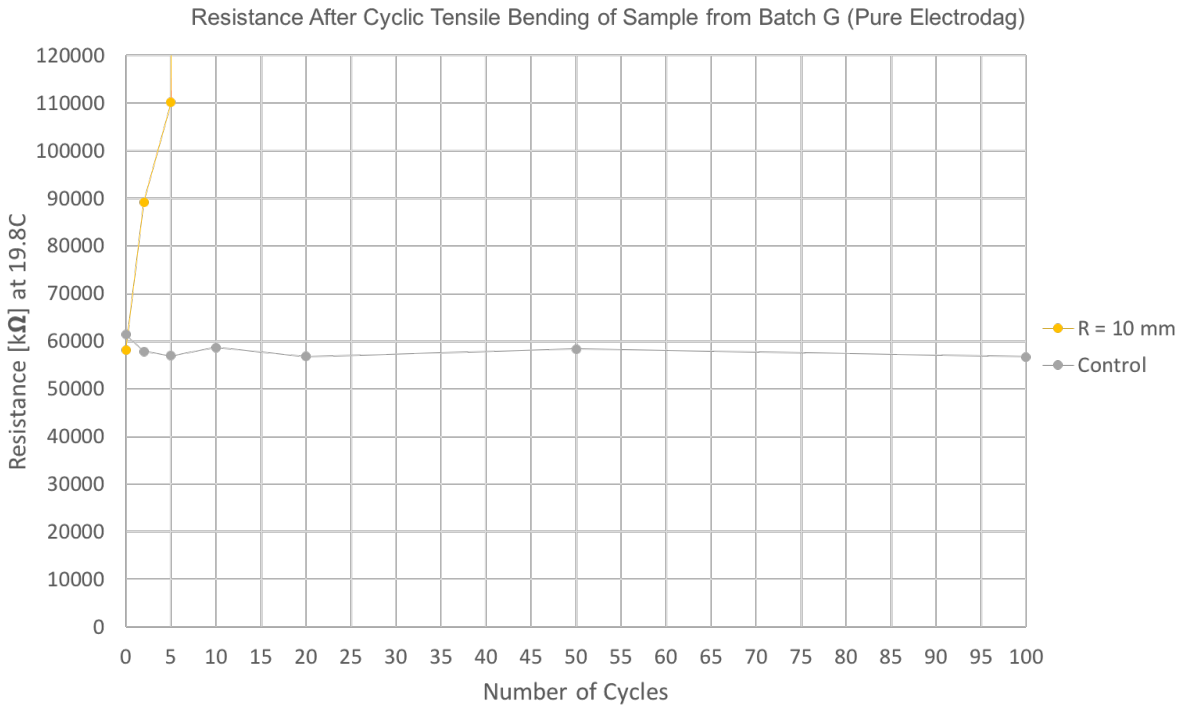

Figure D.1: Resistance after cyclic tensile bending of thermistor composite with pure Electrodag

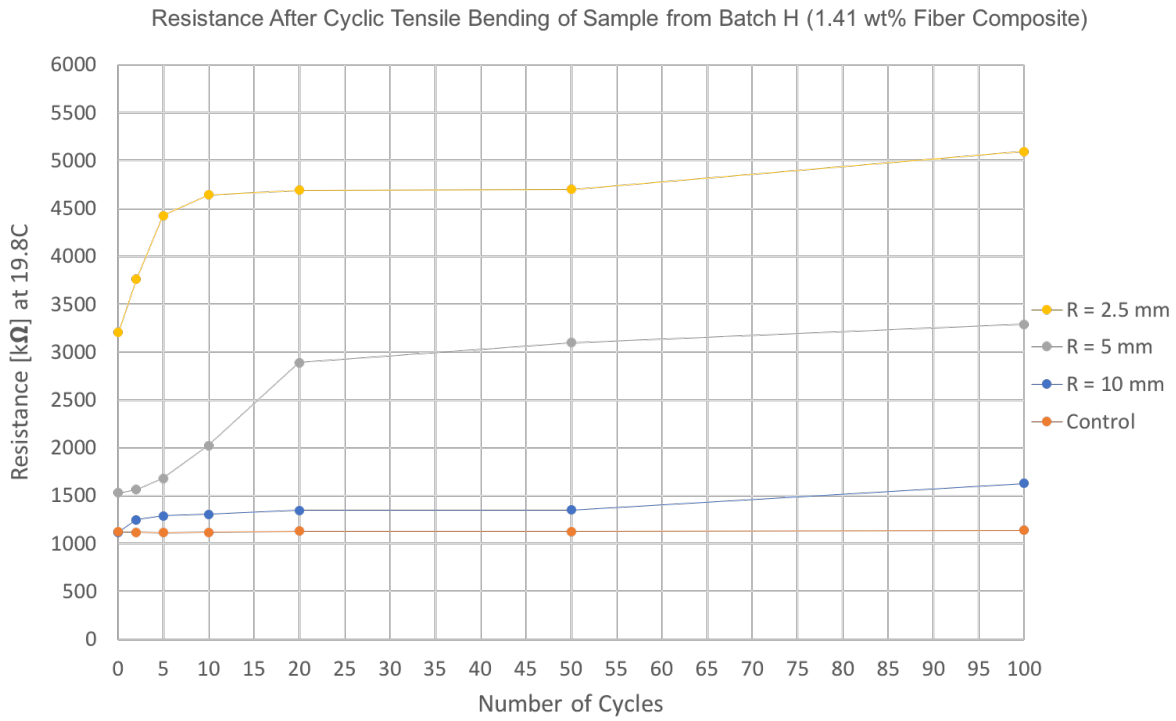

Figure D.2: Resistance after cyclic tensile bending of thermistor composite with 1.41 $wt\%$ of fibres

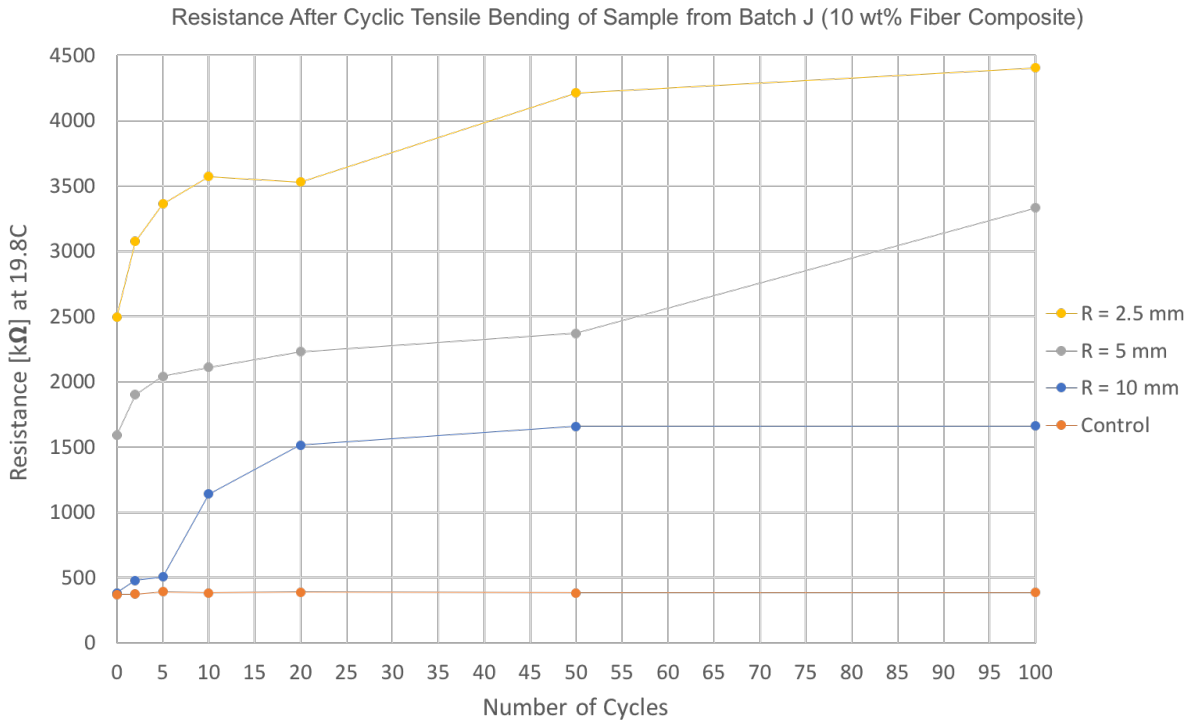

Figure D.3: Resistance after cyclic tensile bending of thermistor composite with 10 $wt\%$ of fibres

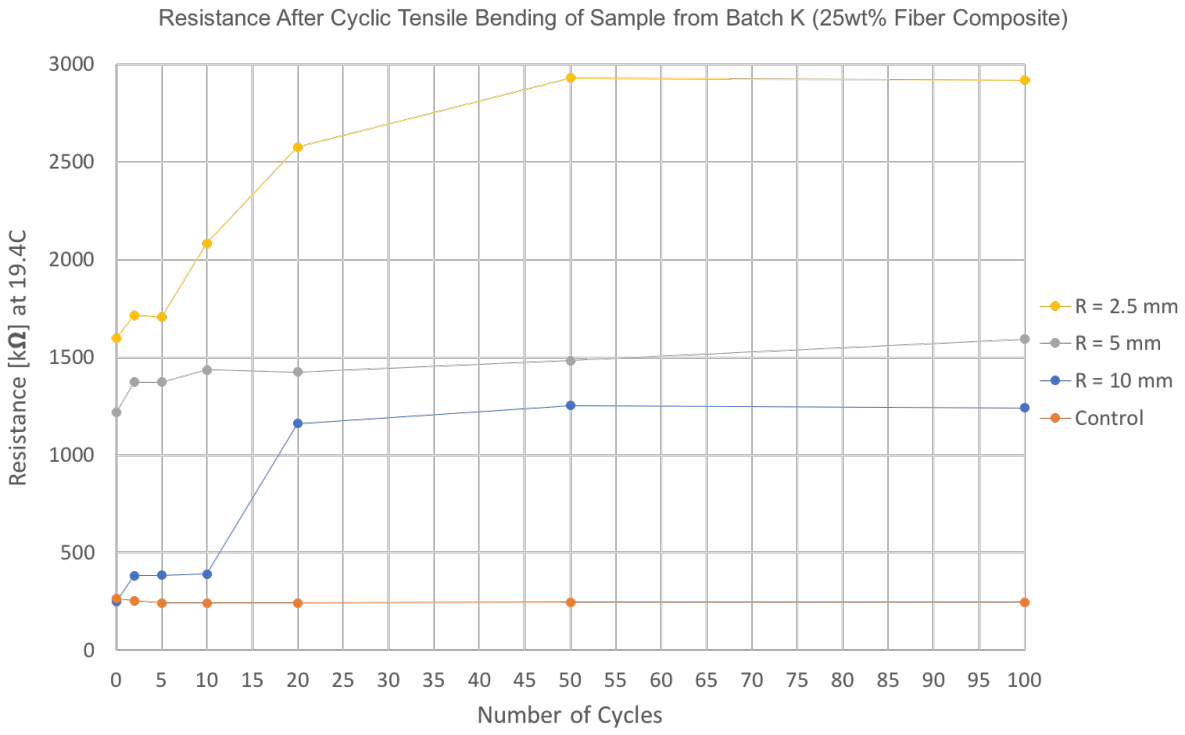

Figure D.4: Resistance after cyclic tensile bending of thermistor composite with 25 $wt\%$ of fibres

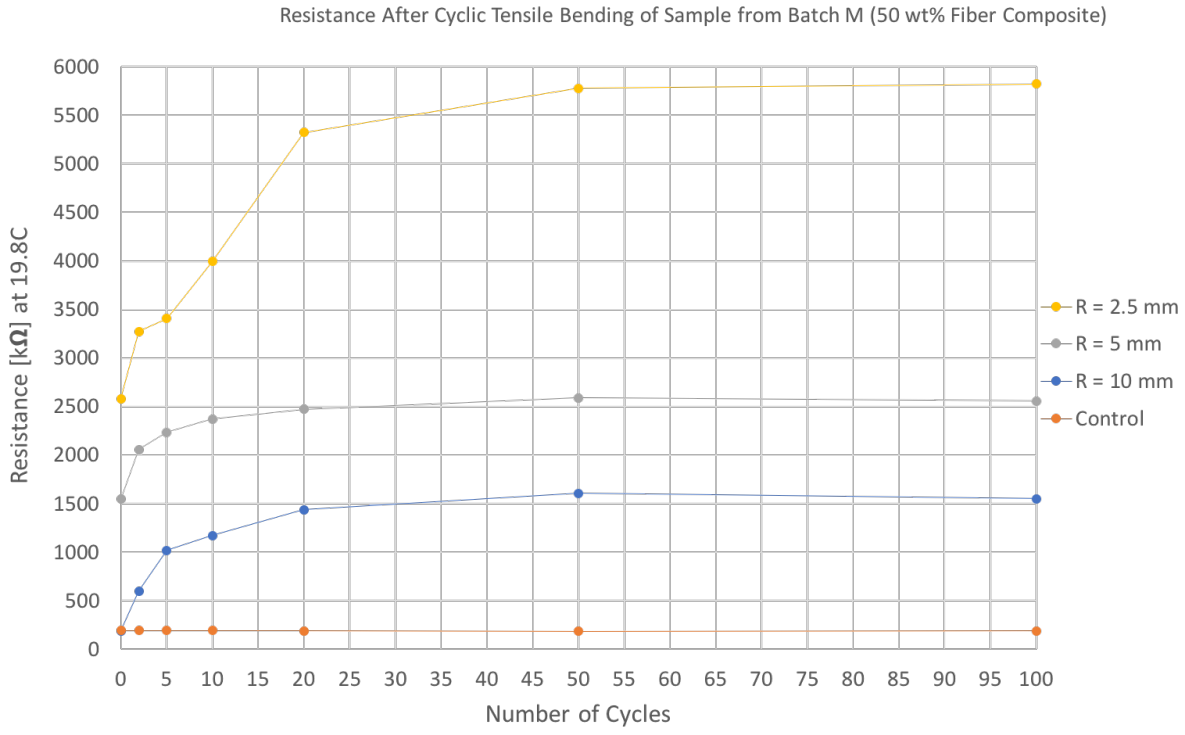

Figure D.5: Resistance after cyclic tensile bending of thermistor composite with 50 $wt\%$ of fibres